Optimal Estimation of the Surface Fluxes of Chloromethanes Using a 3-D Global Atmospheric Chemical Transport Model

by

Xue Xiao

B.S. Atmospheric Science, 1998
M.S. Atmospheric Environment, 2001
Peking University, China

Submitted to the Department of Earth, Atmospheric, and Planetary Sciences
in Partial Fulfillment of the Requirements for the Degree of

DOCTOR OF PHILOSOPHY IN ATMOSPHERIC SCIENCE
AT THE
MASSACHUSETTS INSTITUTE OF TECHNOLOGY

SEPTEMBER 2008

Signature of Author: …….....
Department of Earth, Atmospheric, and Planetary Sciences
August 8, 2008

Certified by: …….....
Ronald G. Prinn
TEPCO Professor of Atmospheric Chemistry
Thesis Supervisor

Accepted by: …….....
Maria T. Zuber
E.A. Griswold Professor of Geophysics
Head, Department of Earth, Atmospheric, and Planetary Sciences

Optimal Estimation of the Surface Fluxes of Chloromethanes Using a 3-D Global Atmospheric Chemical Transport Model

by

Xue Xiao

Submitted to the Department of Earth, Atmospheric, and Planetary Sciences
on August 8, 2008 in Partial Fulfillment of the Requirements for the Degree of

Doctor of Philosophy in Atmospheric Science

ABSTRACT

The four chloromethanes - methyl chloride (CH_3Cl), dichloromethane (CH_2Cl_2), chloroform ($CHCl_3$), and carbon tetrachloride (CCl_4), are chlorine-containing gases contributing significantly to stratospheric ozone depletion and having adverse health effects. Large uncertainties in estimates of their source and sink magnitudes and temporal and spatial variations currently exist. GEIA inventories and other bottom-up emission estimates are used to construct a priori maps of surface fluxes of these species. The Model of Atmospheric Transport and CHemistry (MATCH), driven by NCEP interannually varying meteorological fields, is then used to simulate the trace gas mole fractions using the a priori emissions and to quantify the time series of sensitivities of tracer concentrations to different aseasonal, seasonal, and regional sources and sinks.

We implement the Kalman filter (with the unit pulse response method) to estimate both constant (if applicable) and time-varying surface fluxes on regional/global scales at a monthly resolution for the three short-lived species between 2000-2004, and the continental industrial emissions and global oceanic sink for CCl_4 at a 3-month resolution between 1996-2004. The high frequency observations from AGAGE, SOGE, NIES and NOAA/GMD HATS and other low frequency flask observations are used to constrain the source and sink magnitudes estimated as multiplying factors for the a priori fluxes and contained in the state vector in the Kalman filter. The CH_3Cl inversion results indicate large CH_3Cl emissions of 2240 ± 370 Gg yr^{-1} from tropical plants. The inversion implies

greater seasonal oscillations of the natural sources and sink of CH_3Cl compared to the a priori. Seasonal cycles have been derived for both the oceanic (for $CHCl_3$ and CH_2Cl_2) and terrestrial (for $CHCl_3$) sources, with summer maxima and winter minima emissions. Our inversion results show significant industrial sources of CH_2Cl_2 and CCl_4 from the Southeast Asian region. Our inversions also exhibit the strong effects of the 2002/2003 globally wide-spread heat and drought conditions on the emissions of CH_3Cl from tropical plants and global salt marshes, on the soil fluxes of CH_3Cl and $CHCl_3$, on the biomass burning sources of CH_3Cl and CH_2Cl_2, and on the derived oceanic flux of $CHCl_3$.

Thesis Supervisor: Ronald G. Prinn
Title: TEPCO Professor of Atmospheric Chemistry

Acknowledgements

Above all, I must first thank my advisor Ron Prinn for his support and advice over these many years. Ron provided the necessary direction to start my research project, and then gave me the freedom to follow my own specific interests. He also encouraged and helped me to maintain a critical perspective on the overall scientific picture, and to pursue the underlying physical concepts beneath the modeling and mathematical results.

Many other people who played a role in the production of this thesis deserve my gratitude. Among them include my additional thesis committee members – Alan Plumb, Chien Wang, and Derek Cunnold – who found time in their busy schedules to review my thesis work. Alan Plumb and Chien Wang also reminded me to focus on the scientific concepts, and Derek Cunnold, because of the close collaboration, provided detailed thoughts in the modeling, calculation, and analysis of the thesis results. I should also thank Amram Golombek for his help with the model input, thank David Kicklighter, Julia Lee-Taylor, and Shari Yvon-Lewis for sharing their research results as the a priori inputs into the thesis work. I am also grateful to the many members of AGAGE, SOGE, NOAA-HATS, and NIES, on whose data this work relies.

This thesis is also infinitely better due to my discussions with Jin Huang, Yu-Han Chen, and Qian Tan, for their help with the model and the inversion ideas. My further thanks go to my fellow students and Prinn Group members for their encouragement, and to the Prinn group support staff for their never-ending help. I would also like to thank Carol Sprague in the Education Office for her help.

My final thanks go to my family, my husband Chang for his constant love and support over the years, my son Andrew Haoming who was born during my study at MIT, for bringing us responsibility, happiness, love, and hope. Finally, I dedicate this thesis to Mom and Dad.

This thesis work was supported financially by a variety of sources, including NASA grants NNX07AE89G, NAG5-12669 and NAG5-12099, NSF grant ATM-0120468, and a Martin Family Fellowship at MIT.

Contents

List of Figures

List of Tables

Chapter 1

Introduction

Stratospheric chlorine accounts for 75% of the halogens (chlorine, bromine) involved in stratospheric ozone depletion [*Madronich et al*., 1999]. Methyl chloride (CH_3Cl), chloroform ($CHCl_3$) and dichloromethane (CH_2Cl_2) are relatively short-lived chloromethanes (with lifetimes of 1.3, 0.5 and 0.4-0.5 years, respectively) that contribute about 15% of stratospheric chlorine [*Schauffler et al*., 1993; *Kurylo et al*., 1999]. Carbon tetrachloride (CCl_4) is even longer lived (26-year lifetime) and contributes about 12% to total chlorine in the stratosphere [*Schauffler et al*., 1993].

As a result of the Montreal Protocol and its amendments and adjustments, tropospheric mixing ratios of some major ozone-depleting substances (ODSs) such as CFC-11 (CCl_3F), CFC-113 (CCl_2FCClF_2), and methyl chloroform (CH_3CCl_3) have been decreasing since 1992 [*Prinn et al*., 2000], and CFC-12 (CCl_2F_2) reached steady concentrations and then began to decrease during recent years. As these ODSs of mainly anthropogenic origin are dropping off gradually, those ODSs with substantial natural emissions will play relatively

more and more important roles in stratospheric ozone depletion. Among these gases, the importance of methyl chloride is highlighted as the most abundant halocarbon, estimated to be about 43% of the total reactive chlorine in the troposphere [*Khalil and Rasmussen*, 1999b], and 15-25% of the total recent organic chlorine in the stratosphere [*Schauffler et al*., 1993; *Montzka et al*., 1996]. Chloroform and dichloromethane are defined as very short-lived substances (with lifetimes of a few months or less) by *WMO 2002* [*Montzka and Fraser et al*., 2003], and as such their contributions to stratospheric chlorine are not as important as methyl chloride. Nonetheless, they are two of a number of compounds that individually may contribute only a small amount to the stratospheric chlorine but together may be worth considering more seriously, especially as the long-lived anthropogenic halocarbons are gradually phased out in the atmosphere by the Montreal Protocol. Chloroform is much more important for human health reasons in enclosed environments and in drinking water where people could be exposed to it over long periods of their lives. It is a carcinogen in this capacity and is regarded as a cause for concern when high concentrations are discovered, and so it is regulated by the Environmental Protection Agency (U.S. EPA). Dichloromethane also has health risks, and is classified by EPA as a Group B2 chemical (probable human carcinogen). Dichloromethane is largely of industrial origin, and is recommended as one of the potential indicators for OH concentrations and trends in the troposphere, so estimates of its regional emissions need to be carefully studied. Carbon tetrachloride is the only one regulated by the amended and adjusted Montreal Protocol, but global limits on CCl_4

production apply only after 2005. Inferred emissions in 1999, however, are about 7 times greater than the limits to global production set for 2005 [*WMO 2002*].

Thus careful study of the global and regional budgets, and the emission and sink patterns of these four chloromethanes is warranted. Although most emission processes have been identified, significant uncertainties exist in their magnitudes and variability, especially for those with natural sources which are affected in complicated ways by seasonal and climate changes. A more detailed knowledge of the sources and sinks of these chloromethanes is required in order to improve the understanding of their contributions to stratospheric ozone depletion and to environmental pollution issues.

1.1. Flux estimation and the motivation and goals of the thesis

With the aim of identifying and quantifying the natural emissions of these chloromethanes (especially for methyl chloride recently), considerable effort has been devoted to directly measuring gaseous fluxes from selected surface sources and then extrapolating the local measurements to regional and global scales using highly uncertain aggregation techniques [*Yokouchi et al*., 2000b; *Yokouchi et al*., 2002; *Rhew et al*., 2000]. A typical example is the determination of the global methyl chloride emission from coastal salt marshes [*Rhew et al*., 2000]. Field studies were conducted in two Southern California coastal salt marshes, and then global extrapolations were applied by multiplying the unit area flux with an estimated global salt marsh area under the assumptions that the study sites are representative of salt marshes globally. Some other investigations also used emission process models [*Khalil et al*., 1999; *Lobert et al*., 1999;

Varner et al., 1999] which seek to represent the complicated physical and biological processes associated with the emissions using simple equations and input parameters such as temperature, wind speed, etc., for which global distributions are available. These are "bottom-up" studies. The uncertainties resulting from such approaches are so large that we cannot say that we understand the budgets of methyl chloride and other chloromethanes well enough to assess their future roles in the environment.

An alternative method, applicable to determination of either surface or internal sources or sinks indirectly, is to optimally adjust estimates of these sources or sinks in a chemical transport model to provide a statistically good fit to imperfect observed concentrations of the chemicals of interest [e.g., *Prinn*, 2000], which we call a "top-down" or inverse modeling approach. This method involves solution of an inverse problem in which the observables are integrals and the unknowns (the rates of the processes of production, destruction, emission or uptake) are contained in integrands. The inversion procedure thus obviously requires realistic physical, dynamical and chemical equations or models that relate the rates of the processes to the observations, giving the so-called partial derivative or sensitivity matrix $\mathbf{H}$. In this respect, the MATCH (Model of Atmospheric Transport and CHemistry) model is especially useful because previous studies have shown its remarkable capability to simulate reasonably well the actual timing and magnitude of peaks in observed concentrations of both short [e.g., ^{222}Rn, *Mahowald et al.*, 1997b] and long-lived [e.g., CCl_3F, *Mahowald et al.*, 1997a; CH_4, *Chen and Prinn*, 2005, 2006] species.

The performance of the inverse method also relies on the availability and accuracy of worldwide observations of trace gas levels. Mole fractions (or mixing ratios) of these chloromethanes have been measured in situ at high frequency and in flasks at low frequency, in the globally distributed stations of the Advanced Global Atmospheric Gases Experiment (AGAGE) [*Prinn et al*., 2000], the NOAA Global Monitoring Division (GMD), and other laboratories.

In the light of the highly uncertain flux estimates obtained by source aggregation techniques, and the availability of these high precision observations for flux top-down estimations, the goal of this thesis is to conduct inverse modeling to produce optimized magnitudes and distributions of the surface fluxes of all of the four chloromethanes by sequentially adjusting the fluxes in the MATCH model to fit the concentration observations. An inverse modeling framework for the study of surface fluxes is presented in Figure 1.1. First, an initial guess for the flux magnitudes and distributions (a priori "reference" emission fields) is made. This may be obtained, for example, from the aggregation of the results of the emission measuring campaigns. Second, this initial guess is used to drive the model, producing model-predicted concentrations, which can be corrupted by model systematic and random errors. Third, the model predictions are compared to the corresponding noise-corrupted observations in an optimal estimator, which produces the updated emission fields. The newly updated fluxes can be entered into another circle of estimation using additional observations. The high frequency observations potentially offer strong constraints on emissions, especially for estimating

both seasonal and interannual flux changes. There are several interesting questions that are proposed to be addressed in this thesis:

(1) What are the distributions in space and time of the surface fluxes of chloromethanes and what are the driving processes?

(2) Are tropical plants a large source for methyl chloride as recently proposed from in situ studies?

(3) Are seasonal changes dominant in driving the variations of the surface fluxes for the largely natural chloromethanes (CH_3Cl and $CHCl_3$)? What are the magnitudes and variability of their natural sources and what are the causes for their variability?

(4) Are the optimized magnitudes and distributions of surface fluxes of carbon tetrachloride consistent with their industrial production rates and end-uses?

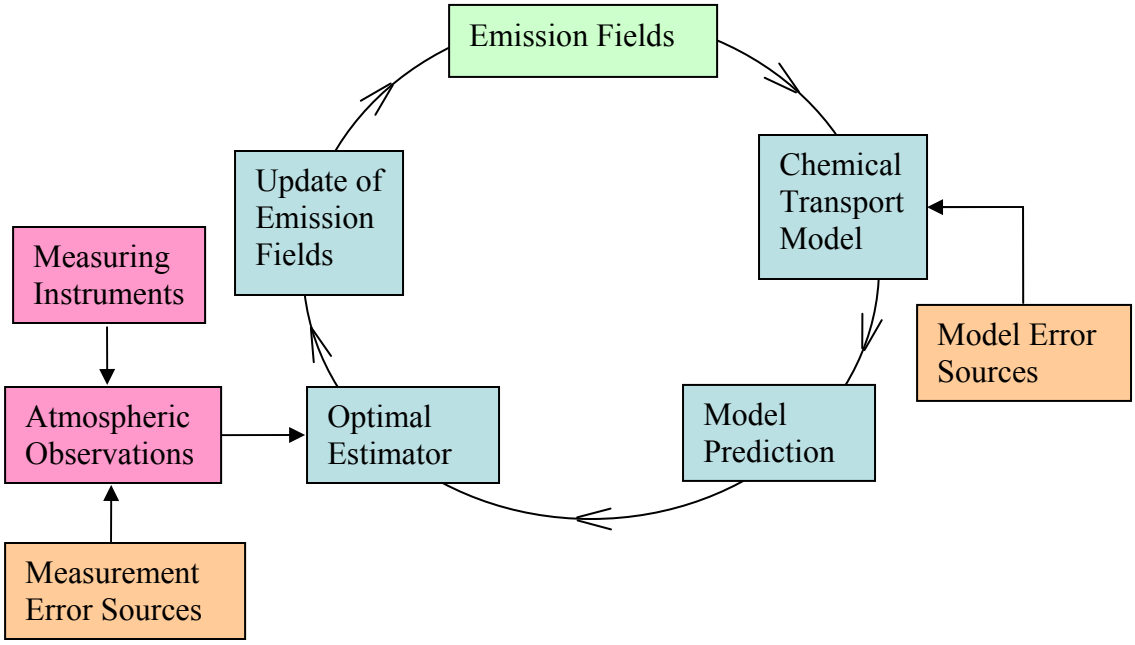

Figure 1.1. General schematic describing the forward and inversion technique for the study of chloromethane surface fluxes.

1.2. Chapter descriptions

The following describes the organization of the thesis, beginning with the available data, model and technique, followed by the inversion results and conclusions.

Chapter 2 introduces the high and low frequency surface observations used to constrain the surface fluxes in the inversion processes. Observational errors are defined to encompass the instrumental, low frequency sampling, and model grid volume – observational location mismatch errors.

Chapter 3 describes the chemical transport model (MATCH) used throughout this thesis, in which the concentrations of OH which is the primary atmospheric sink of CH_3Cl, CH_2Cl_2, and $CHCl_3$, and the rates of stratospheric photodissociation which is the primary sink for CCl_4 have been calculated and scaled to reproduce the appropriate reported lifetimes of each gas and of OH indicator gases like CH_3CCl_3.

Chapter 4 develops the inversion methodology used to optimally estimate the chloromethane surface fluxes. The Kalman filter is adapted to estimate either constant or time-varying fluxes, and the unit pulse method [*Chen and Prinn*, 2006] is used in MATCH to compute the sensitivity matrix needed in the filter. An example of inverting for the natural surface fluxes of CH_3Cl is presented and the inversion behavior is examined.

Chapter 5 presents the inversion results for the seasonal, annual, and interannual surface fluxes of CH_3Cl, and examines the influences of the seasonal and interannual climate

changes on the variations of the flux magnitudes. We further test the sensitivity of the inversion to using different sets of observations. We test the inversion results by running the optimized fluxes forward in MATCH, followed by a comparison to the observations.

Chapter 6 Similarly presents, tests, and discusses the inversion results for the seasonal, annual, and interannual surface fluxes of the natural sources of $CHCl_3$. **Chapter 7** similarly presents the inversion results for the constant industrial sources and seasonal, annual, and interannual natural sources of CH_2Cl_2. **Chapter 8** presents the inversion results for the industrial sources and oceanic sink of CCl_4.

Chapter 9 summarizes the main findings and contributions of this thesis.

Chapter 2

Observations

The performance of the inverse modeling is highly dependent on the availability and accuracy of the measurements. This thesis work uses both high frequency in situ and low frequency flask observations of the concentrations (expressed as mole fractions) of the chloromethanes, with greater weight on the high frequency data due to its capability to capture the major variations in time. These two sampling strategies broadly represent the two complementary approaches to global sampling: high sampling frequency versus high spatial coverage. The Advanced Global Atmospheric Gases Experiment (AGAGE) operates the greatest number of high frequency stations [*Prinn et al*., 2000], while the Global Monitoring Division (GMD) of NOAA operates the greatest number of flask sites. Additional high frequency or flask observations are available from the system for observation of halogenated greenhouse gases in Europe (SOGE) and the National Institute for Environmental Studies (NIES) in Japan.

2.1. High and low frequency observations

Table 2.1 lists the stations for the high and low frequency observations that we use in the inversions. The ALE/GAGE/AGAGE in situ real-time global measurement network is intended to measure the concentrations of anthropogenic or anthropogenic/biogenic ozone-depleting and climate-forcing gases in air [*Prinn et al*., 2000; *Sturrock et al*., 2001; *O'Doherty et al*., 2004]. The Atmospheric Lifetime Experiment (ALE) began in July 1978 using Gas Chromatographs (GC) with Electron Capture Detectors (ECD) to measure 5 species including carbon tetrachloride at a frequency of four times per day [*Prinn et al*., 2000]. This GC experiment was succeeded in the 1981-1985 time frame by the Global Atmospheric Gases Experiment (GAGE), using new GC instrumentation with ECD and Flame Ionization Detectors (FID) to measure 3 additional gases including chloroform at an increased frequency of 12 times per day [*Prinn et al*., 1990, 1992; *Cunnold et al*., 1994]. The Advanced Global Atmospheric Gases Experiment (AGAGE), began over the 1993-1996 period increasing the measuring frequency to 36 times per day and using GCs with three detectors (ECD, FID, and MRD (Mercuric oxide Reduction Detectors)) to measure five biogenic/anthropogenic gases and five anthropogenic gases [*Prinn et al*., 2000]. Methyl chloride and dichloromethane have been measured since 1998 using a new gas chromatographic-mass spectrometric system (GC-MS) [*Prinn et al*., 2000], currently present at all five of the AGAGE primary stations.

The high measurement frequency also enables excellent resolution of short-term variability such as pollution events which are typically of 1 to 3 days duration, while

monitoring methods using flask collections cannot practically resolve such events. The high frequencies thus enable the data during pollution periods to be used to assess source strengths for regions proximal to the stations. For example, *Cox et al*. [2003] used back trajectory analysis techniques to identify the air mass origin of high pollution events of CH_3Cl, $CHCl_3$ and CH_2Cl_2 at Cape Grim, Tasmania.

While in situ measurement networks provide high frequency, highly consistent observations, the global stations are located sparsely, limiting the resolution of the estimated flux distributions. Given fixed resources, flask sampling allows greater spatial coverage than high frequency sampling because samples need only be collected, rather than actually measured, at a site. The samples are then delivered to a central laboratory for analysis. CCl_4 and CH_3Cl samples have been collected and analyzed by the HATS (Halocarbons & other Atmospheric Trace Species Group) Flask Sampling Program of NOAA/GMD [*Montzka et al*., 1999, 2000]. The NOAA/GMD HATS Flask Network has stations shown in Table 2.1 and Figure 2.1. The GMD flask measurement results are from typically weekly sampling and analysis of 2 stainless steel or glass flasks that were filled simultaneously.

Different measuring networks are using different calibration standards, and therefore their data need to be converted to the same calibration scale when combined together and used in the inversions. Inter-comparison of AGAGE data with other laboratories provides the information of the ratios of other standards to AGAGE standard [*Krummel et al*., personal communication]. Throughout this thesis we convert the other network scales to

the AGAGE scales, and the calibration factors for CH_3Cl, CH_2Cl_2, $CHCl_3$, and CCl_4 (from left to right) are shown in Table 2.1. Measurements from laboratories other than AGAGE or the AGAGE-affiliated SOGE are divided by the corresponding factors to be converted to the AGAGE standard in this work.

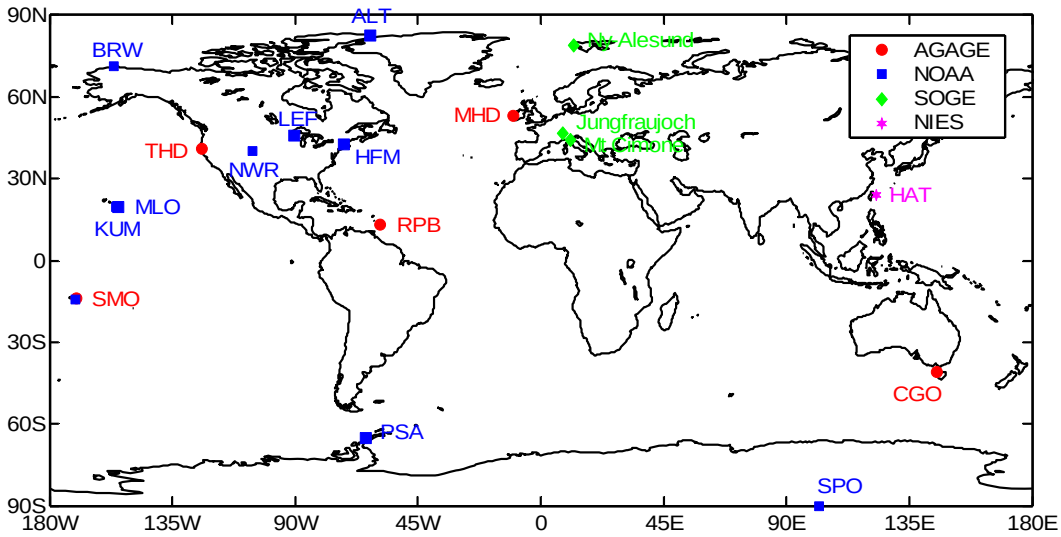

Figure 2.1. Location of chloromethane observing sites from different laboratories.

Table 2.1. Location of the chloromethane measuring stations and their calibration factors relative to AGAGE.

Number	ID	Station Location	Latitude	Longitude	Altitude	Laboratory	Calibration ($CH_3Cl/CH_2Cl_2/CHCl_3/CCl_4$)
High Frequency Observations							
1	MHD	Mace Head, Ireland	53.3ºN	9.9ºW	25	AGAGE	1/1/1/1
2	THD	Trinidad Head, California	41.0ºN	124.0ºW	140	AGAGE	1/1/1/1
3	RPB	Ragged Point, Barbados	13.0ºN	59.0ºW	42	AGAGE	1/1/1/1
4	SMO	Cape Matatula, American Samoa	14.3ºS	170.6ºW	42	AGAGE	1/1/1/1
5	CGO	Cape Grim, Tasmania	41.0ºS	145.0ºE	94	AGAGE	1/1/1/1
6	JUN	Jungfraujoch, Switzerland	46.5ºN	8.0ºE	3580	SOGE	1/1/1/1
7	MTE	Monte Cimone, Italy	44.2ºN	10.7ºE	2165	SOGE	1/1/1/1
8	ZEP	Zeppelin St., Norway	78.9ºN	11.9ºE	474	SOGE	1/1/1/1
9	HAT	Hateruma, Japan	24.1ºN	123.8ºE	47	NIES	1.0313/-/1.1716/-
10	BRW	Pt. Barrow, Alaska	71.3ºN	156.6ºW	8	GMD	1.0029/-/-/1.0362
11	MLO	Mauna Loa, Hawaii	19.5ºN	155.6ºW	3397	GMD	1.0029/-/-/1.0362
12	NWR	Niwot Ridge, Colorado	40.0ºN	105.5ºW	3018	GMD	1.0029/-/-/1.0362
13	SMO	Cape Matatula, American Samoa	14.3ºS	170.6ºW	77	GMD	1.0029/-/-/1.0362
14	SPO	South Pole, Antarctica	89.9ºS	24.8ºW	2810	GMD	1.0029/-/-/1.0362

Low Frequency Observations							
15	ALT	Alert, Northwest Territories, Canada	82.5ºN	62.5ºW	210	GMD	1.0103/1.0890/1.1107/1.0410
16	BRW	Pt. Barrow, Alaska	71.3ºN	156.6ºW	11	GMD	-/1.0890/1.1107/-
17	LEF	WLEF tower, Wisconsin	46.0ºN	90.3ºW	470	GMD	1.0103/1.0890/1.1107/-
18	HFM	Harvard Forest, MA	42.5ºN	72.2ºW	340	GMD	1.0103/1.0890/1.1107/-
19	NWR	Niwot Ridge, Colorado	40.1ºN	105.6ºW	3472	GMD	-/1.0890/1.1107/-
20	MLO	Mauna Loa, Hawaii	19.5ºN	155.6ºW	3397	GMD	-/1.0890/1.1107/-
21	KUM	Cape Kumukahi, Hawaii	19.5ºN	154.8ºW	3	GMD	1.0103/1.0890/1.1107/1.0410
22	SMO	American Samoa	14.2ºS	170.6ºW	77	GMD	-/1.0890/1.1107/-
23	PSA	Palmer Station, Antarctica	64.9ºS	64.0ºW	10	GMD	1.0103/1.0890/1.1107/-
24	SPO	South Pole, Antarctica	89.98ºS	102.0ºE	2841	GMD	-/1.0890/1.1107/-

- Hyphen: is used where there is no measurement or no comparison for the species for that station.

2.2. Observational errors

Our interpretation using inverse methods requires both a continuous or nearly continuous record of monthly means (χ) and estimates of their uncertainties (which can be represented by standard deviations (denoted σ) under the assumption of a normal distribution). The monthly mean mole fractions at the in situ sites can be directly computed from the available data made in each month at each station. For the low frequency flask measurements, only a few (weekly or bi-weekly) measurements are taken in each month. Although monthly mean values can also be calculated as the average values of the available data, large uncertainties should be assigned to these means as described below. The square of the standard deviations, i.e., the variances (σ^2) of the uncertainties of the monthly means can be estimated as the sum of the errors associated with: (1) the measurement error, (2) the frequency of sampling used to define the monthly mean, and (3) the "mismatch" error between the local point observations and the model grid volume [*Chen and Prinn*, 2006]. This assumes reasonably that these errors are uncorrelated.

The measurement error includes those associated with instrumental, sampling, and inter-calibration imperfections. The instrumental precision varies slightly between different laboratories.

The sampling frequency error accounts for how well the observational monthly mean is defined given a finite number of measurements. Assuming temporally uncorrelated

atmospheric mole fractions, the standard deviation represents the error on a mean quantity due to a limited sampling frequency [*Wunsch*, 1996] which can be expressed as:

$$\sigma_{sampling\ \ frequency} = \sqrt{\frac{\sigma_{mon}^2}{m}} \tag{2.1}$$

where σ_{mon}^2 at each site is the variance of the mole fractions during each month, and can be estimated from the high frequency in situ measurements themselves, or from the MATCH high frequency output as an approximation, because we do not have high frequency measurements everywhere. We compared the high frequency model outputs and in situ measurements, and the variability of the model is nearly equal to the variability of the actual observations. We use MATCH-derived σ_{mon}^2 for both in situ sites and flask sites. The term m is the number of measurements during the month made by the measuring network. This indicates greater usefulness of high frequency in situ measurements than low frequency flask measurements, because the in situ measurements usually have hundreds or thousands of numbers (m ~ 1000), while the flask measurements are typically taken at weekly (bi-weekly) frequency (m ~ 4). *Chen and Prinn* [2006] discussed the high frequency versus low frequency model means. Throughout the thesis we use outputs at all model time steps within a month to compute the model monthly means (i.e., the high frequency model means).

In the Kalman filter we compare point station observations with grid cell averaged concentrations predicted by the model, which causes the so-called "mismatch" or "representation" error. This error may either be considered the model error to measure the

failure of the model to represent a point measurement, or the observational error to measure the failure of a point measurement to represent the volume average. We choose to put this error into the observational error, thus effectively assuming a perfect transport model for this purpose in the inversion. The standard deviations of the high frequency measurements at in situ sites provide reasonable estimates of the mismatch errors, because the station during each month samples a substantial fraction of the air mass from the large volume of air in the grid cell box containing that station [*Prinn*, 2000]. For the flask measurements, since only weekly or bi-weekly air masses are sampled, we have chosen to estimate the mismatch error at each flask site using the standard deviation of the modeled mole fractions (y) at the nine surrounding grid cells [*Chen and Prinn*, 2006]:

$$\sigma_{mismatch} = \sqrt{\sigma^2_{surrounding\ \ 9\ grid\ \ cells}}$$

$$= \sqrt{\frac{1}{9}\sum_{i=1}^{9}\left(y_{ik} - \bar{y}_k\right)^2} \qquad (2.2)$$

where i indicates the index of the surrounding grid cells, and k is the index of the month. We are thus assuming that the spatial variability within a single grid cell is related to the variability between that grid cell and the neighboring grid cells. Note that the mismatch error at any particular site varies month by month. The square root of the sum of the variances of the above three types of errors gives the total observational error:

$$\sigma_k = \sqrt{\sigma^2_{measurement} + \sigma^2_{sampling\ \ frequency} + \sigma^2_{mismatch}} \qquad (2.3)$$

The derived monthly mean mole fractions and their standard deviations are used as key parameters in the Kalman filter algorithm designed for surface flux estimation.

Chapter 3

The MATCH Model

The Model of Atmospheric Transport and CHemistry (MATCH) is used in this thesis. It is an off-line transport model developed primarily by Philip Rasch, Brian Eaton, Natalie Mahowald, and Mark Lawrence, with smaller contributions by many others. MATCH contains the basic meteorological component [e.g., *Rasch et al*., 1997; *Mahowald*, 1996; *Mahowald et al*., 1997a, b]. Its extension including detailed global tropospheric photochemistry, called the Max-Planck-Institute for Chemistry version of MATCH (MATCH-MPIC) was developed by *Lawrence et al*. [e.g., 1999b].

MATCH has been widely used and well-tested for a variety of tracers in many applications. *Rasch et al*. [1997] compared MATCH to the on-line NCAR Community Climate Model (CCM), and showed that the errors associated with using sampling timescales in an off-line model that are longer than the typical 20-30 minute dynamical integration time scale, can be made small when the sampling interval is of order 6 hours or less. They also showed that one can accurately reproduce the subgrid-scale processes

within the off-line model. *Mahowald* [1996] and *Mahowald et al*. [1997a, b] compared MATCH radon simulations with observations and performed an inverse modeling study of CCl_3F. *Lawrence* [1996] introduced MATCH-MPIC and employed it to study the photochemistry of the tropical Pacific troposphere. *Lawrence et al*. [1999b] extended this work to investigate the photochemistry of the entire global troposphere. MATCH has also been used in studies of the sulfur cycle [*Lucas and Prinn*, 2005], aerosols, photochemistry, and in studies of plume tracers for the Indian Ocean Experiment intense field phase [e.g., *Rasch et al*., 2001; *Collins et al*., 2001, 2002; *Lawrence et al*., 2003]. Also, *von Kuhlmann et al*. [2003] have modeled tropospheric ozone and hydrocarbons using an updated version. *Chen and Prinn* [2005, 2006] and *Chen* [2004] performed optimal estimation of methane and carbon dioxide surface fluxes using MATCH. Success in these simulations by MATCH demonstrated its capability in representing transport, hydrologic processes, and photochemistry for both long-lived and short-lived species.

3.1. Meteorology in MATCH

One important advantage of off-line models is that they are less expensive to run than "on-line" models, such as general circulation models (GCMs) and numerical weather prediction (NWP) global models, in which the meteorological data are also predicted at every time step. MATCH, an off-line transport model, can be driven by archived gridded time-dependent meteorological data derived from forecast center analyses. Throughout this work, MATCH is driven by NOAA National Center for Environmental Prediction (NCEP) reanalysis meteorology. The model-predicted species values can be compared

directly with the values from field measurements, rather than comparing values representative of model and measured climatological means.

The basic meteorology fields input into the model are for temperature, surface pressure, meridional and zonal wind speeds, surface wind stresses, and surface latent and sensible heat fluxes. These inputs occur at regular (usually 6-hour) intervals. All other meteorological parameters (e.g., vertical velocities, cloud fractions, and convective mass fluxes) are computed on-line based on these basic meteorological fields. The model time step is 40 minutes for the T42 spectral resolution used in this thesis. The archived data are linearly interpolated between the neighboring time intervals to obtain the values for each time step. Using 6-hourly meteorological data in an off-line simulation was found to be sufficient to reproduce the effects that quickly changing fields such as convection have on tracers [*Rasch et al*., 1997].

The horizontal spectral resolution of the input analysis data and the integrations is chosen to be T42, which corresponds to approximately 2.8º × 2.8º (64 × 128 grid points). Due to the large number of simulations required for the reference runs and the unit pulse runs used in the inverse modeling, T42 is a reasonably good choice. As computational power increases, we could use T62 [*Chen and Prinn*, 2005, 2006]. In the vertical, MATCH uses a hybrid coordinate, which consists of a terrain-following sigma coordinate combined with (optional) constant pressure level values (usually employed in the stratosphere). The NCEP data are on 28 sigma levels, with 18 levels in the troposphere, and 10 levels in the stratosphere.

The three basic types of transport simulated in MATCH are advection, dry turbulent mixing, and moist convection [*Lawrence et al*., 1999b]. Our version implements the mass-conserving SPITFIRE (SPlit Implementation of Transport using Flux Integral REpresentation) flux-form advection scheme [*Rasch and Lawrence*, 1998]. Dry turbulent mixing is simulated in MATCH based on the non-local boundary layer scheme [*Holtslag and Boville*, 1993]. Finally, a parameterization for moist convection provides the model with cumulus transport, convective cloud top and bottom levels, and convective precipitation and evaporation rates. Our version uses the Zhang/McFarlane/Hack (ZMH) convection scheme [*Zhang and McFarlane*, 1995; Hack, 1994]. First, the penetrative deep convection scheme of *Zhang and McFarlane* [1995] is used to reduce the convective available potential energy (CAPE). Next, the local mixing scheme of *Hack* [1994] is applied to remove any remaining local instabilities by exchanging moisture, energy and tracers between neighboring layers. This version of MATCH is also capable of simulating nearly the full tropospheric hydrological cycle, with the exception of using the surface latent heat fluxes from the archived data as the initial condition.

3.2. Photochemistry in MATCH

3.2.1. OH fields

Although MATCH can be extended to simulate the complicated photochemistry in the atmosphere [e.g., *Lawrence et al*., 1999b; *von Kuhlmann et al*., 2003; *Lucas and Prinn*, 2005], only simple chemistry needs to be incorporated into the basic MATCH model for the simulation of chloromethanes because they are not major sinks for OH or sources of

HO_x. The predominant removal process in the troposphere for CH_3Cl, CH_2Cl_2 and $CHCl_3$ is oxidation by the hydroxyl (OH) radical, which is the primary oxidizing chemical in the atmosphere. The reactions are as following [*Sander et al*., 2003]:

$$CH_3Cl + OH \rightarrow CH_2Cl + H_2O \quad (3.1)$$

$$CH_2Cl_2 + OH \rightarrow CHCl_2 + H_2O \quad (3.2)$$

$$CHCl_3 + OH \rightarrow CCl_3 + H_2O \quad (3.3)$$

$$CCl_4 + OH \rightarrow \text{products} \quad (3.4)$$

The temperature-dependent rate constant for reaction with the OH radical is given in the Arrhenius form:

$$k(T) = A\exp[(-E/R)(1/T)] \quad (3.5)$$

where A is the pre-exponential factor (cm^3 $molecule^{-1}$ s^{-1}), E (J mol^{-1}) is the activation energy, R is the universal gas constant, and T (K) is the temperature. Table 3.1 lists the values of these parameters that we have used [*Sander et al*., 2003], and the illustrative values of the rate constants at a selected tropospheric average temperature of 272 K [*Spivakovsky et al*., 2000] for the four chloromethanes. The reaction rate constants are also used to generate the OH-removal lifetimes by reference to CH_3CCl_3, whose OH-removal lifetime is 5.0 years [*WMO 2002*; *Prinn et al*., 2005]. In the model simulation, these reaction rate constants are updated each time step based on the ambient conditions (temperature, pressure, etc.) in the grid cells.

Table 3.1. Rate constants (cm^3 $molecule^{-1}$ s^{-1}) of the reactions for each chloromethane and the associated lifetimes for their removal (except for CCl_4, see foot note).

	A	*E / R*	k_{OH} *(at 272 K)*	Lifetime (years)
CH_3CCl_3 + OH	1.6×10^{-12}	1520	6.0×10^{-15}	5.0
CH_3Cl + OH	2.4×10^{-12}	1250	2.4×10^{-14}	1.2
CH_2Cl_2 + OH	1.9×10^{-12}	870	7.8×10^{-14}	0.39
$CHCl_3$ + OH	2.2×10^{-12}	920	7.5×10^{-14}	0.40
CCl_4 + OH	$\sim 1.0 \times 10^{-12}$	> 2300	$< 2.1 \times 10^{-16}$	26[1]

The reaction rate obviously depends on the assumed concentration of OH. The OH fields chosen are from the output generated using the version of MATCH-MPIC described in *Lawrence et al*. [1999b], *Jöckel* [2000], and *von Kuhlmann et al*. [2003]. This MATCH version incorporates a full photochemical component, representing the major known sources (e.g., industry, biomass burning), transformations (chemical reactions and photolysis), and sinks (e.g., wet and dry deposition) for studies of ozone and hydrocarbons in the troposphere. *Chen and Prinn* [2005, 2006] used the monthly mean MATCH-MPIC 3-D OH fields at T63 resolution adjusted to fit global AGAGE CH_3CCl_3 observations (we reduced these to T42 for this thesis). Finally, a diurnal cycle scaled to the solar zenith angle is further applied to the daily average OH concentrations interpolated by MATCH from the monthly mean OH concentrations. This ensures zero

[1] This 26-year global lifetime comes from the principle sinks for CCl_4 which are stratospheric photo-dissociation with a 35-year lifetime [*WMO 1998*], and the oceans with a 94-year lifetime [*Yvon-Lewis and Butler*, 2002].

nighttime values while maintaining the daily average OH concentrations [*Chen and Prinn*, 2005, 2006]. Since the annual and global average OH did not change much (within 3%) over the period of 2000-2004 [Figure 2, *Prinn et al*., 2005], we used annually repeating OH fields. This allows us to assess the effect of the interannually varying transport (captured in the NCEP data) on the concentrations of the gases.

3.2.2. Stratospheric sink

In the stratosphere, the chloromethanes are photodissociated and/or oxidized by the hydroxyl radical. However, the stratospheric sink plays different roles in the total atmospheric sink of each chloromethane. The stratospheric sink is small for CH_3Cl (7.6% of the total atmospheric loss), and is very small for the shorter-lived species CH_2Cl_2 (1.7% of the total) and $CHCl_3$ (< 2% of the total) [*Keene et al*., 1999; *Cox et al*., 2003]. Most of the stratospheric loss of CH_3Cl arises from OH attack [*Seinfeld and Pandis*, 1998], which is accounted for by the 3-D OH fields in MATCH. Reactions with OH in the stratosphere for CH_2Cl_2 and $CHCl_3$ have also been included in MATCH. For CCl_4, stratospheric photodissociation is the most important sink, and is much larger than its destruction by $O^1(D)$ [*Golombek and Prinn*, 1986, 1989, 1993]. In this thesis we only consider stratospheric photodissociation for CCl_4, because of lack of information about and the negligible role of the stratospheric sink for the other three short-lived species. The chemical destruction rates (J values in s^{-1}) for stratospheric photodissociation of CCl_4 have been calculated from a more detailed 3-D model for the stratosphere [*Golombek and Prinn*, 1986, 1989, 1993]. Here we interpolated the monthly mean photodissociation rate

fields that vary with latitude and altitude to the MATCH grids. We do not explicitly model stratospheric destruction of CCl_4 by $O^1(D)$ since it is minor as mentioned above. Figure 3.1 shows the latitude-altitude 2-D distributions of the stratospheric photodissociation rates of CCl_4 in January (a) and July (b). In general the J values are highest in the top layers of the model where the available light is the strongest, and the J values decrease downward. For each vertical layer, the highest J values occur near the latitude of 20ºS in January and 20ºN in July following the seasonal variation of insolation on the earth.

These values are then modified by a constant global factor to reflect the appropriate best estimate of the stratospheric lifetime for CCl_4. Due to the very rapid vertical and horizontal variations of the J values, the interpolation from the *Golombek and Prinn* model to the MATCH model produces typically factor-of-two errors. Without any adjustment factor, the data would give a lifetime of ~ 13.8 years (the target lifetime is ~ 35 years). We have conducted modeling trials by multiplying the data by factors less than 1 and checking the implied lifetimes to obtain the factor yielding 35 years.

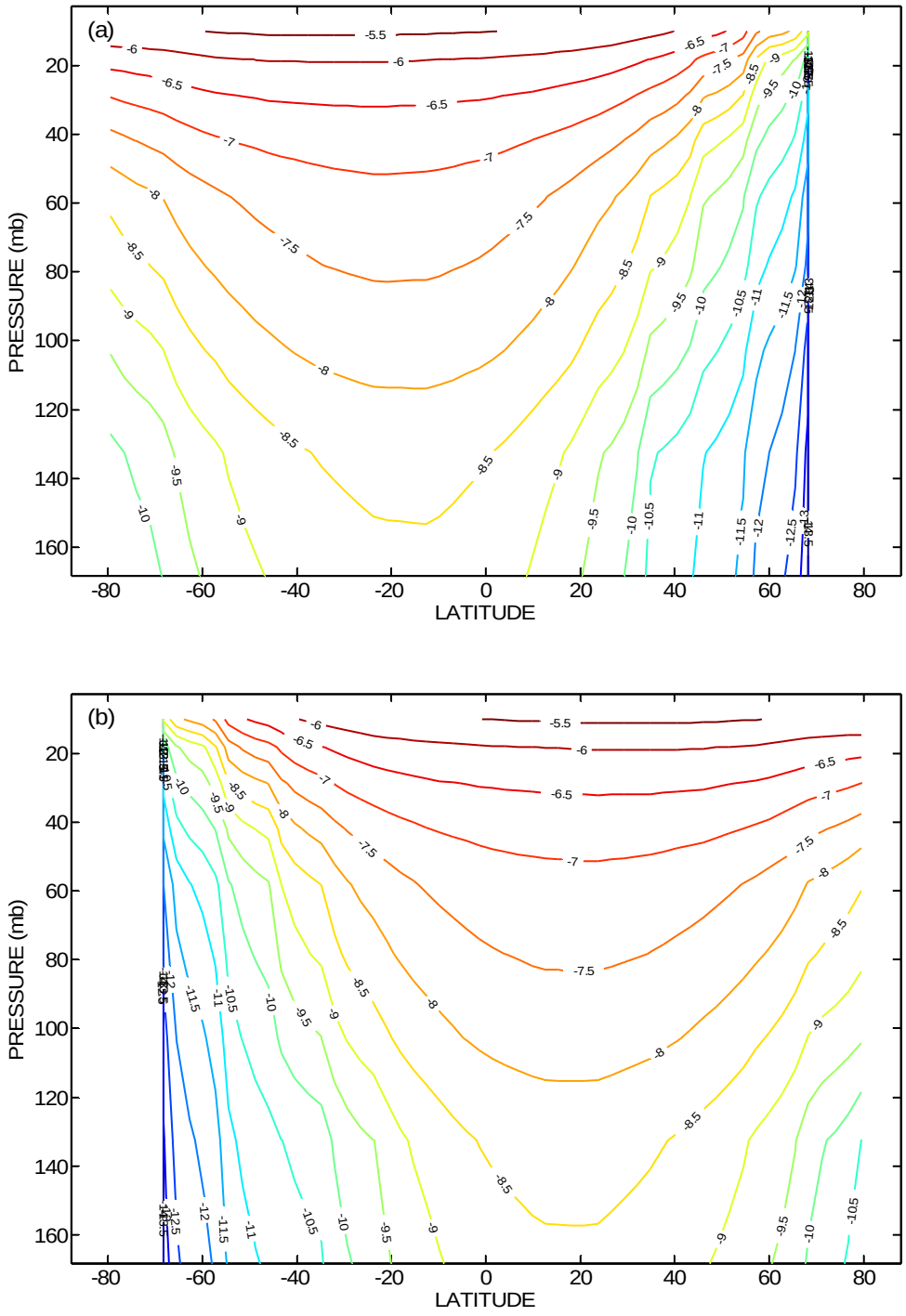

Figure 3.1. The $\log_{10}$ of the stratospheric photodissociation rates (in s^{-1}) for carbon tetrachloride in January (a) and July (b) that correspond to a stratospheric destruction lifetime of 35 years.

Chapter 4

Methodology for Inverse Modeling

Inverse modeling using mathematical methods that optimally combine observations with model calculations is routinely applied in meteorology, oceanography, seismology and remote sensing. Inverse modeling of global biogeochemical cycles has also received much attention because of the recognition of the important roles of chemically and radiatively active species in Earth's environment. This biogeochemical inverse modeling activity is made possible by large observational programs, which include world-wide measurements of trace gas concentrations and their isotopic composition in monitoring station networks.

4.1. The state-space model and the measurement equation

The construction of a number of inversion techniques has been based on a state-space representation. In a state-space representation, we incorporate the underlying dynamics as a stochastic model, to be distinguished from deterministic model. This is because deterministic systems have unavoidable shortcomings so they can not provide a totally

sufficient means of performing the analysis. There are several reasons. First of all, no mathematical description of any dynamic (physical, chemical, etc.) system is perfect. Any such model depicts only those characteristics of direct interest to the modeler's purpose. Secondly, dynamic systems are driven not only by our own inputs, but also disturbances which we can neither control nor model deterministically. Finally, the measurement devices that we use to observe the actual system behavior can not practically provide perfect and complete data about the system. Specifically, we define a practical stochastic model, the basic form of which is the evolution of a state vector $\mathbf{x}(t)$ driven by white Gaussian noise, as expressed by the so-called "state-space" equation or "system" model [e.g., *Gelb et al*., 1974; *Prinn*, 2000]:

$$\mathbf{x}(t) = \mathbf{M}(t-1)\mathbf{x}(t-1) + \boldsymbol{\eta}(t-1) \tag{4.1}$$

Equation (4.1) describes a time-dependent model incorporating a set of rules for computing the state vector at time t from knowledge of its value at previous time $t-1$ by using the matrix operator $\mathbf{M}(t-1)$ (the "evolution" or "transition" matrix, bold capital letters refer to matrices and bold lower case letters refer to vectors hereafter), and the stochastic external or boundary forcing (or the "controls") $\boldsymbol{\eta}(t-1)$ with a zero mean and a covariance matrix $\mathbf{Q} \equiv \boldsymbol{\eta}\boldsymbol{\eta}^{\mathrm{T}}$. The controls can also represent the model random forcing.

Correspondingly available are measurements which are similarly corrupted by white Gaussian noise. The general standard linear form relating the state vector to a time series of observed quantities is:

$$\mathbf{y}^{o}(t) = \mathbf{H}(t)\mathbf{x}(t) + \boldsymbol{\varepsilon}(t) \tag{4.2}$$

where the matrix **H** in general represents arbitrarily complex linear or pseudo-linear relations between the quantities of interest (e.g., the surface fluxes) stored in the state (column) vector $\mathbf{x}$ and the observations (e.g., the concentration measurements) arrayed in the column vector $\mathbf{y}^{o}$ with the inevitable measurement noises arrayed in $\boldsymbol{\varepsilon}$ which has zero mean and the covariance matrix $\mathbf{R} \equiv \boldsymbol{\varepsilon}\boldsymbol{\varepsilon}^{T}$. Equation (4.2) is called the "measurement" equation or model, and the matrix **H** is called the "measurement" or "partial derivative" or "sensitivity" matrix.

The Kalman filter is chosen as the inversion technique throughout the thesis. This "optimal estimation" method uses the measurements to give a "minimum variance" estimate of the state vector taking into account the accuracy of the observations, the nature and accuracy of the physical and chemical processes embodied in the model, the initial conditions and any prior knowledge of the behavior of the state vector [e.g., *Gelb et al*., 1974].

4.2. The Kalman filter

The Kalman filter has been used in a number of studies to estimate the atmospheric lifetime or global source of CFCs [e.g., *Cunnold et al*., 1983; *Hartley and Prinn*, 1993; *Mulquiney and Norton*, 1998; *Prinn et al*., 2000] and other trace gases [e.g., *Xiao et al*., 2007]. The Kalman filter is an optimal recursive data processing algorithm first derived by *Kalman* [1960] for the discrete case and by *Kalman and Bucy* [1961] for the

continuous case. It processes all available measurements, accounting for their precision, to estimate the current values of the quantities of interest (the states), with use of: (1) knowledge of the system and measurement instrument dynamics, (2) the statistical description of the system errors, measurement noises, and uncertainty in the dynamics models, and (3), any available information about the initial conditions of the state variables of interest. The covariance matrix, $\mathbf{P}$, of the error in the state estimate is also computed, and from this we have an estimate of the uncertainty in the state estimate. The Kalman filter, like all filters, aims to reduce the influence of noise in the measurements on the state estimation [*Mulquiney et al*., 1993]. The word "recursive" means that, unlike certain other data processing concepts, the Kalman filter does not require all previous data to be kept in storage and reprocessed every time a new measurement is taken. This will be of importance to assessing the value of each observation and to the practicality of implementation.

In the following, we briefly describe how the Kalman filter inverts the measurement equation. In reality, most of the measurements are not continuous in time, so we replace the time *t* by some discrete time index k as in *Prinn* [2000]. The standard equations of the model and data in the discrete form are:

$$\mathbf{x}_k = \mathbf{M}_{k-1}\mathbf{x}_{k-1} + \boldsymbol{\eta}_{k-1} \tag{4.3}$$

$$\mathbf{y}_k^o = \mathbf{H}_k\mathbf{x}_k + \boldsymbol{\varepsilon}_k \tag{4.4}$$

$$E[\boldsymbol{\varepsilon}_k] = 0,\ E[\boldsymbol{\varepsilon}_k\boldsymbol{\varepsilon}_k^T] = \mathbf{R}_k,\ E[\boldsymbol{\varepsilon}_k\boldsymbol{\varepsilon}_{k'}^T] = 0,\ k \neq k' \tag{4.5}$$

$$E[\boldsymbol{\eta}_k] = 0\,,\ E[\boldsymbol{\eta}_k \boldsymbol{\eta}_k^T] = \mathbf{Q}_k \tag{4.6}$$

$$\tilde{\mathbf{x}}(0) = \mathbf{x}_0\,,\ E[(\tilde{\mathbf{x}}(0) - \mathbf{x}_0^t)(\tilde{\mathbf{x}}(0) - \mathbf{x}_0^t)^T] = \mathbf{P}_0 \tag{4.7}$$

Equation (4.4) (a discrete form of Equation (4.2)) describes the projection of the states onto the observations. The statistics of the measurement errors and the controls are described in Equations (4.5) and (4.6), where E[] denotes the expectation value. $\mathbf{R}_k$ can include the model error, instrumental error, and mismatch (between the measured and modeled atmospheric volumes) error, and $\mathbf{Q}_k$ can represent random forcing in the system model due to transport model errors [*Prinn*, 2000]. Finally, the a priori initial condition and its uncertainty are given by Equation (4.7) where the tilda (~) denotes an estimate and the superscript t denotes the true value (which we never know exactly). The basic Kalman filter recursion is composed of three steps which can be derived from minimum variance or maximum likelihood estimation methods [*Gelb et al*., 1974; *Prinn*, 2000; *Todling*, 2000]:

Step 1: Extrapolation/prediction:

$$\mathbf{x}_k^f = \mathbf{M}_{k-1}\mathbf{x}_{k-1}^a \tag{4.8}$$

$$\mathbf{P}_k^f = \mathbf{M}_{k-1}\mathbf{P}_{k-1}^a\mathbf{M}_{k-1}^T + \mathbf{Q}_{k-1} \tag{4.9}$$

Before the use of $\mathbf{y}_k^o$ and its error covariance matrix $\mathbf{R}_k$, we extrapolate the state vector and its error covariance matrix to the next time step from the knowledge of the mechanics

of the model, where the unknown control terms ($\boldsymbol{\eta}_{k-1}$) have been replaced by the best estimate we can make of them, specifically their mean, which is zero. An "f" or "a" superscript has been added to $\mathbf{x}_k$ and $\mathbf{P}_k$ to show that these are "forecast" values before the use of the data at time k or "analysis" values after the use of time k data. Also we define $\mathbf{x}_0^a = \mathbf{x}_0$ and $\mathbf{P}_0^a = \mathbf{P}_0$ to initialize the filter.

Step 2: Computation of the Kalman gain matrix:

$$\mathbf{K}_k = \mathbf{P}_k^f \mathbf{H}_k^T (\mathbf{H}_k \mathbf{P}_k^f \mathbf{H}_k^T + \mathbf{R}_k)^{-1} \tag{4.10}$$

The effect of $\mathbf{K}_k$ is to construct a weighting factor in which one effectively compares the error covariance $\mathbf{H}_k \mathbf{P}_k^f \mathbf{H}_k^T$ in the predicted measurement ($\mathbf{y}_k = \mathbf{H}_k \mathbf{x}_k^f$) with the error covariance $\mathbf{R}_k$ of the real measurement ($\mathbf{y}_k^o$).

Step 3: State vector correction/improvement:

$$\mathbf{x}_k^a = \mathbf{x}_k^f + \mathbf{K}_k (\mathbf{y}_k^o - \mathbf{H}_k \mathbf{x}_k^f) \tag{4.11}$$

$$\mathbf{P}_k^a = \mathbf{P}_k^f - \mathbf{K}_k \mathbf{H}_k \mathbf{P}_k^f \tag{4.12}$$

Equation (4.11) takes the weighted average between the state vector prediction $\mathbf{x}_k^f$ and the state vector correction inferred from the current $\mathbf{y}_k^o$. In this "predictor-corrector" structure, based on all previous information, a prediction of the values that the desired variables and measurement will have at the next measurement time is made. Then, when

the next measurement is taken, the difference between it and its predicted value (often called the innovation or mismatch $\boldsymbol{\upsilon}_k \equiv \mathbf{y}_k^o - \mathbf{H}_k \mathbf{x}_k^f$; not to be confused with the observation residual $\mathbf{y}_k^o - \mathbf{H}_k \mathbf{x}_k^a$ which is calculated at the optimal solution) is used to "correct" the prediction of the desired variables. A block diagram portrayal of the algorithm is shown in Figure 4.1.

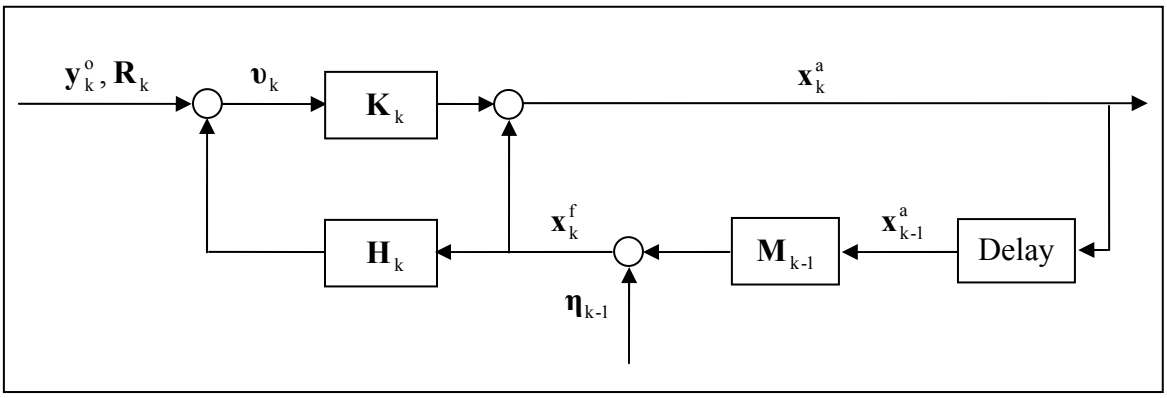

Figure 4.1. Sampled-data Kalman filter block diagram [adapted from *Maybeck*, 1979].

The Kalman filter goes through all the available data up to the final one. The state estimates are optimal in the sense that the trace of the state error covariance matrix is minimized. The Kalman filter requires $\mathbf{M}_k$, $\mathbf{H}_k$, $\mathbf{Q}_k$, and $\mathbf{R}_k$ to be known. These quantities can all vary with time. A guess of the initial state and its error covariance is also required.

The Kalman filter is convenient in that all the previous information before and including the time step k is contained in $\mathbf{x}_k^a$ and $\mathbf{P}_k^a$, and there is no need to reprocess it (as in a "batch" inversion) every time a new measurement is taken. A key feature (advantage) of the Kalman filter is that the error covariance matrix, $\mathbf{P}_k^a$, evolves in time using the state-space model. We use the square root of the diagonal elements of $\mathbf{P}_k^a$ to give the uncertainties ($1\,\sigma$) on our state variable estimates. The off-diagonal elements of $\mathbf{P}_k^a$ contain the error covariances between state variables. Note that the matrix $\mathbf{K}_k\mathbf{H}_k \le \mathbf{I}$, which means that $\mathbf{P}_k^a \le \mathbf{P}_k^f$, and thus that the variances of the errors in the state vector element estimates should decrease with the use of more and more measurements by amounts sensitively dependent on the measurement errors. However, for a measurement at time k whose $\mathbf{R}_k \to \infty$, then $\mathbf{K}_k \to 0$, so that $\mathbf{x}_k^a = \mathbf{x}_k^f$, and $\mathbf{P}_k^a = \mathbf{P}_k^f$ (i.e., there is no improvement of the state vector estimate because the measurement is too noisy to be useful in the filter). The opposite limit occurs when the measurement is perfect so that $\mathbf{R}_k \to 0$, then $\mathbf{K}_k \to \mathbf{H}_k^{-1}$, so that $\mathbf{x}_k^a = \mathbf{H}_k^{-1}\mathbf{y}_k^o$, and $\mathbf{P}_k^a = 0$. This means we totally trust Equation (4.4) at time k (now it effectively becomes $\mathbf{H}_k\mathbf{x}_k + 0 = \mathbf{y}_k^o$) which we can solve directly for $\mathbf{x}_k^a$, and $\mathbf{P}_k^a = 0$ (assuming $\mathbf{Q}_k = 0$ and $\mathbf{x}$ is time-invariant).

4.3. Adaptation of the Kalman filter

4.3.1. Construction of the state vector and its error covariance matrix

In this subsection we adapt the Kalman filter to estimate chloromethane surface fluxes from different sources and sinks at monthly (or 3-month) time resolution on regional or global scales. For this purpose, it is adequate to use monthly mean observations to constrain the monthly (or 3-monthly) surface fluxes. What we actually estimate are the magnitudes of the regional or global fluxes by location and/or process, assuming we know their spatial distributions within each region (referred to as the a priori reference maps). Specifically, the state vector in the Kalman filter contains variables representing the regional or global magnitudes of the surface fluxes of the chloromethanes with month-to-month or quarter-to-quarter variations allowed for the seasonal processes. There are two further features of our definition of the state vector. Firstly, we will actually estimate multiplying factors for the a priori reference magnitudes for the surface fluxes. This concept of normalization avoids the situation in which the magnitudes of the fluxes are orders of magnitude different which can easily lead to near-singular matrices in numerical computations. Secondly, for an Eulerian chemical transport model, it is necessary to define the state vector as the adjustment to its a priori or reference value [*Prinn*, 2000]. Regarding the temporal resolution for estimations, we treat the anthropogenic and natural surface fluxes in different ways. For the natural sources and sinks, we are interested in their possible seasonal variations (e.g., driven by climatological variables) and so we estimate each flux type regionally or globally on a

monthly basis for the time period of 2000-2004. The industrial sources of the three short-lived chlorohydromethanes (CH_3Cl, CH_2Cl_2, and $CHCl_3$) are assumed to not be changing very much either intra-annually or interannually and are therefore treated as constants during 2000-2004. The exception is CCl_4 whose mole fraction trends suggest variations in its industrial sources. We estimate the sources and sinks of CCl_4 at a 3-month (seasonal) resolution, because we expect smaller variability than for the chlorohydromethanes, and because the time period we are interested in (1996-2004) is double the time period for the three chlorohydromethanes and our computer time is limited.

Here we use the "unit pulse" method of *Chen and Prinn* [2006]. Suppose we have n_{as} invariant/constant (aseasonal) and n_s seasonally varying surface flux variables. The full state vector is therefore composed of $n_{as} + n_s * 12$ elements. This is a huge number considering the size of the estimation error covariance matrix of the state vector and imposes a huge demand on computer time and memory during the inversion. However, given the fact that the global horizontal mixing time in the model is about 1 year, namely, an observation cannot meaningfully separate monthly fluxes that are more than one year old [*Chen and Prinn*, 2006], it is a good approximation to use a specific monthly observation at time k to deduce not all but only those monthly fluxes from time k back to time k-T (where T = 11 months), i.e., 12 months' seasonal fluxes. So the resultant down-sized state vector is defined as:

$$\mathbf{x}_k = \begin{bmatrix} \mathbf{X}_k^{as} \\ \mathbf{X}_k^{s} \\ \mathbf{X}_{k-1}^{s} \\ \dots \\ \mathbf{X}_{k-T}^{s} \end{bmatrix} \tag{4.13}$$

where $\mathbf{X}_k^{as}$ is a subvector containing all the n_{as} aseasonal flux variables, and $\mathbf{X}_k^{s}$ is a subvector containing all the n_s monthly/seasonal flux variables at time k. Notice that $\mathbf{X}_{k-T}^{s}$ is the "oldest" seasonal fluxes that the observation $\mathbf{y}_k^{o}$ can provide information about, and therefore it is the final, optimized solution for fluxes at time k-T and is removed from the state vector before a new observation $\mathbf{y}_{k+1}^{o}$ comes in. To achieve this removal, *Chen and Prinn* [2006] borrow the mathematics (but not the underlying concepts) behind the extrapolations of Equations (4.8) and (4.9). A constant transition matrix is used with the following form:

$$\mathbf{M} = \begin{bmatrix} \mathbf{I}_{n_{as}} & 0 & 0 & 0 & 0 \\ 0 & 0 & 0 & 0 & 0 \\ 0 & \mathbf{I}_{n_s} & 0 & 0 & 0 \\ 0 & 0 & \mathbf{I}_{n_s} & 0 & 0 \\ \dots & \dots & \dots & \dots & \dots \\ 0 & 0 & 0 & \mathbf{I}_{n_s} & 0 \end{bmatrix} \tag{4.14}$$

where $\mathbf{I}_{n_{as}}$ and $\mathbf{I}_{n_s}$ represent square identity sub-matrices of sizes n_{as} and n_s corresponding to the n_{as} aseasonal fluxes and n_s seasonal fluxes, respectively. The 0's

represent matrices with all zero elements. The transition matrix operates on the state vector as follows:

$$\begin{bmatrix} \mathbf{I}_{n_{as}} & 0 & 0 & 0 & 0 \\ 0 & 0 & 0 & 0 & 0 \\ 0 & \mathbf{I}_{n_s} & 0 & 0 & 0 \\ 0 & 0 & \mathbf{I}_{n_s} & 0 & 0 \\ \dots & \dots & \dots & \dots & \dots \\ 0 & 0 & 0 & \mathbf{I}_{n_s} & 0 \end{bmatrix} \bullet \begin{bmatrix} \mathbf{X}_k^{as} \\ \mathbf{X}_k^{s} \\ \mathbf{X}_{k-1}^{s} \\ \dots \\ \mathbf{X}_{k-T+1}^{s} \\ \mathbf{X}_{k-T}^{s} \end{bmatrix} \searrow \searrow \searrow \searrow \searrow = \begin{bmatrix} \mathbf{X}_k^{as} \\ 0 \\ \mathbf{X}_k^{s} \\ \mathbf{X}_{k-1}^{s} \\ \dots \\ \mathbf{X}_{k-T+1}^{s} \end{bmatrix} \tag{4.15}$$

$\boxed{\mathbf{X}_{k-T}^{s}}$ = *optimized fluxes*

Multiplying $\mathbf{x}_k$ by $\mathbf{M}$ not only removes $\mathbf{X}_{k-T}^{s}$ which is saved as the final, optimized solution, but also introduces a new $\mathbf{X}_{k+1}^{s}$ whose initial guess is its (zero) a priori value. For the aseasonal components, the transition matrix retains the previous values, which is consistent with the estimation of constant fluxes over all time steps.

Operation of $\mathbf{M}$ on the error covariance matrix $\mathbf{P}_k^a$ of $\mathbf{x}_k$ has similar effects as on $\mathbf{x}_k$ by removing the error covariances of $\mathbf{X}_{k-T}^{s}$, but it introduces zeros for the initial error covariances of $\mathbf{X}_{k+1}^{s}$ to be estimated. This problem is solved by the inclusion of the matrix $\mathbf{Q}_k$ of the following form:

$$\mathbf{Q}_k = \begin{bmatrix} 0 & 0 & 0 & 0 & 0 \\ 0 & E\left[\boldsymbol{\eta}_k \boldsymbol{\eta}_k^T\right] & 0 & 0 & 0 \\ 0 & 0 & 0 & 0 & 0 \\ 0 & 0 & 0 & 0 & 0 \\ \ldots & \ldots & \ldots & \ldots & \ldots \\ 0 & 0 & 0 & 0 & 0 \end{bmatrix} \tag{4.16}$$

where $E[\boldsymbol{\eta}_k \boldsymbol{\eta}_k^T]$ represents our choice of the initial error covariances associated with the new seasonal flux adjustments ($\mathbf{X}_{k+1}^s$). For the seasonal fluxes we use initial errors of ± 30% to ± 100% of their reference magnitudes, which the Kalman filter then reduces through the use of 12 subsequent months of observations. The aseasonal fluxes are also initialized with errors equal to or larger than their reference magnitudes, introduced by the non zero values in the upper-left corner of $\mathbf{P}_0^a$. The large aseasonal a priori errors are always substantially reduced using all observations over the entire time series, since they represent assumed constant fluxes.

4.3.2. Computation of the sensitivity matrix

In the above subsection we discussed the construction of the state vector $\mathbf{x}_k$ and matrices $\mathbf{P}_0^a$, $\mathbf{M}_k$, and $\mathbf{Q}_k$ which are needed in the Kalman filter. In this subsection we discuss the computation of the sensitivity matrix. In canonical form, a chemical transport model is a mapping of input variables (sources, sinks, etc.) onto output variables (concentrations in mole fractions). If this mapping is differentiable, its first derivative is

the Jacobian (sensitivity) matrix $\mathbf{H}_k$. The elements of $\mathbf{H}_k$ for our applications can be written as:

$$h_{ijk} = \frac{\partial y_{ik}^{o}}{\partial x_{j}^{t}} \approx \frac{\partial y_{ik}}{\partial x_{j}} \approx \frac{\Delta y_{ik}}{\Delta x_{j}} \tag{4.17}$$

for aseasonal fluxes or

$$h_{ijkk'} = \frac{\partial y_{ik}^{o}}{\partial x_{jk'}^{t}} \approx \frac{\partial y_{ik}}{\partial x_{jk'}} \approx \frac{\Delta y_{ik}}{\Delta x_{jk'}} \tag{4.18}$$

for seasonal fluxes. Equations (4.17) and (4.18) express the sensitivity of the change in the measurement at location i resulting from a change in the unknown constant state variable x_j (this could be the trace gas source or sink or other estimated parameters such as transport rates) or the seasonal state variable $x_{jk'}$ in a previous month k'. By approximating y_i^o by y_i in the model, we are actually trying to compare the average y_i predicted in a grid volume of the model to an actual measurement y_i^o at a point (measuring site). This "mismatch" between the measured and modeled atmospheric volumes may cause errors that could be considered either measurement or modeling errors. Note that even for a fixed change Δx_j in variable x_j, the sensitivity Δy_i is not invariant because of the evolution of the chemical transport system, which means **H** is time-varying.

A straightforward approach for computing $\mathbf{H}$ for an n-dimensional state vector $\mathbf{x}$ is to do n+1 model runs, the first run using a reference (e.g. a priori best estimate) of $\mathbf{x}$, the other n runs using values of $\mathbf{x}$ with one element slightly perturbed from its reference value, thus enabling computation of $\mathbf{H}$ through Equations (4.17) and (4.18). For a complicated chemical transport model, the equivalent and more efficient way is to do a single model run with n+1 chemically identical (but separately labeled) chemical species. One of the chemical species uses a reference (e.g. a priori best estimate) of $\mathbf{x}$, while the other n species use values of $\mathbf{x}$ with one element slightly perturbed from its reference value.

We use different procedures to generate the aseasonal and seasonal sensitivities. For aseasonal fluxes we perturb a single process/region above the reference level by 1% and run it over the entire data period. The sensitivities are then determined by subtracting the perturbation and reference runs, and dividing by the total emission perturbation to produce a sensitivity time series in terms of parts per trillion (ppt) / (Gg yr^{-1}) (1Gg = 10^9 grams). The aseasonal sensitivity elements thus contain the influence of all previous months from the very beginning of the period. For seasonal fluxes we distinguish each single month during the entire period to study the seasonality. Therefore we calculate the sensitivities to each single month by perturbing a single process/region above the reference level for only that month (k') and then tracking the tracer within the model after that month for a subsequent period over which the emission pulse decays due to atmospheric dispersion and chemical loss. We call this the unit pulse method for the seasonal sensitivity calculations. For the period of 2000-2004 we have done 5 years × 12

months = 60 monthly pulse runs. Each of the 60 monthly pulses is a separate multi-tracer run starting at a different month. As noted before, the global mixing (dispersion) time in the model is about one year, so we have run each of the 60 monthly pulses for 12 months instead of over the full 2000-2004 period.

Figures 4.2 (a) and (b) show some examples of the calculated sensitivities of individual sites to an individual seasonal process of CH_3Cl source as functions of time. Here, a January 2000 emission pulse from the tropical plants in Africa is displayed. It is a uniform pulse with an intensity of 10 Gg yr^{-1} lasting for one month. Note that the sensitivities are greatest in the first 3-4 months and then decrease because of atmospheric mixing and chemical loss. Responses at different sites have different behaviors because of their different locations relative to the source region in the global circulation fields. The Barbados and Samoa stations are located in the tropical easterly wind region and are therefore directly downwind of the African region. Hence, they respond rapidly with sharp peaks. The Barbados station is even closer to the African region than the Samoa station, so its response is even more rapid, followed by a decrease at both stations due to dispersion. The other three stations are either further away from or not in the same zonal wind band as the source region. Therefore their responses are relatively smooth with steady slow increases in mole fractions followed by decreases due to OH destruction. Also note that the responses at the different sites tend to converge to a single value after one year, which is consistent with an emission pulse in a well-mixed atmosphere, and serves to validate our choice of a 12-month estimation period.

We also note that the high frequency (every 40 minutes) sensitivities (Figure (4.2) (a)) show negative values occasionally. They are likely due to the numerical round off (noise) in the MATCH simulations, because these sensitivities are the differences between two very close runs (perturbation and reference runs) for an emission pulse of small magnitude. Because we only need to use the model monthly mean mole fractions, we have averaged these to monthly mean sensitivities (Figure (4.2) (b)) and thus avoided the negative values.

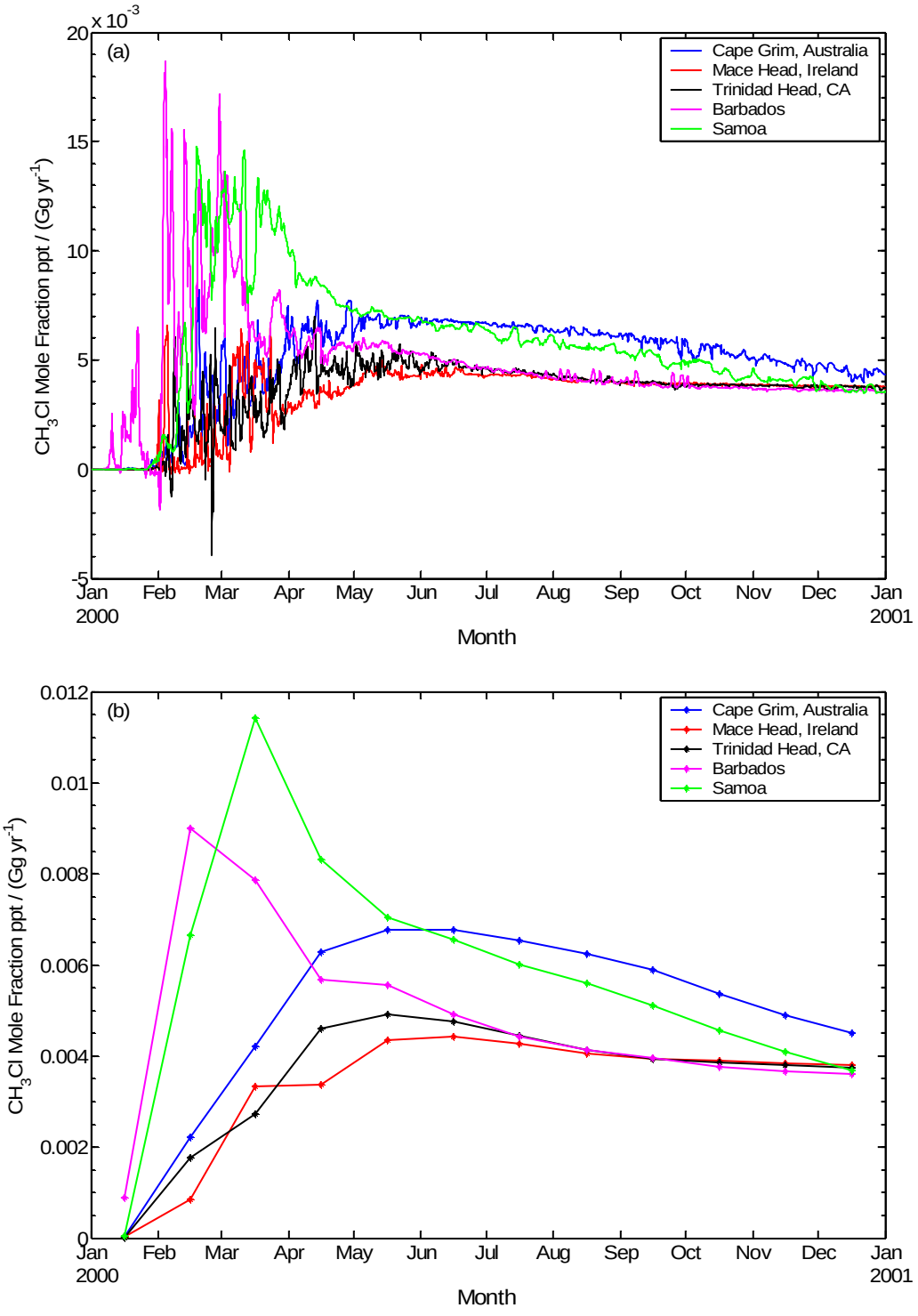

Figure 4.2. MATCH-modeled sensitivities of methyl chloride high frequency (a) and monthly mean (b) mole fractions at the AGAGE measuring stations to a January, 2000

emission pulse from African tropical plants. Eventually the mole fractions reach values consistent with a small methyl chloride emission pulse in a well-mixed atmosphere, followed by a slow decrease due to OH destruction.

In Figure 4.3 we put the sensitivity time series for the whole 60 monthly pulses from African tropical plants together. There is interannual variability as well as seasonal variability. Since the magnitude of the pulse is identical and the OH fields are annually repeating, the interannual variability of the monthly pulse sensitivities is due only to the interannually varying transport.

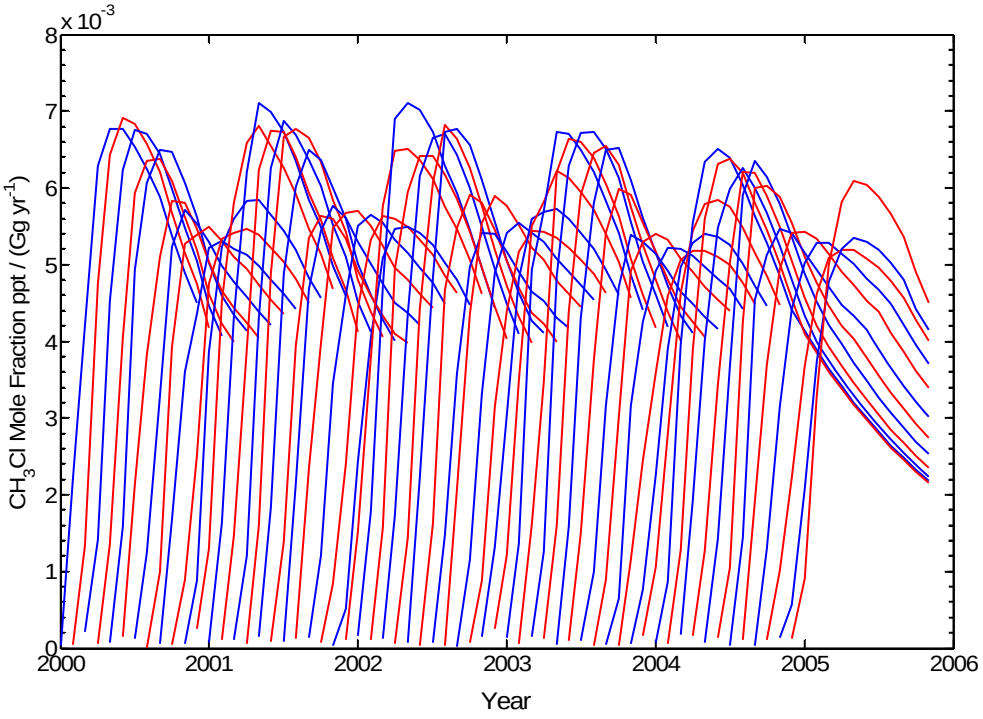

Figure 4.3. MATCH-modeled sensitivities of Cape Grim, Australia (CGO) to the 60 monthly emission pulses from tropical plants in Africa for the period of 2000-2004. For each pulse we have run for 12 months and the sensitivities are displayed.

4.4. Inversion behavior

In this section we study the inversion process when applying this methodology to the optimal estimation of the surface fluxes of methyl chloride. Most of the sources and sinks of methyl chloride are seasonally varying such as emissions from tropical plants, biomass burning, oceans, salt-water marshes, and the soil sink. Certain processes are further divided into several geographical regions of interest, for example emissions from tropical plants have been divided into American tropical plants (Trop AM), Asian tropical plants (Trop AS), and African tropical plants (Trop AF), and the biomass burning source has been divided into Biomass East (BB East) and Biomass West (BB West). The other sources and the soil sink are estimated on the global scale. Note that we actually estimate the integrated flux magnitudes of those processes and regions, and the spatial distributions of the fluxes are remained as their corresponding references. There are hundreds of monthly flux elements in the state vector. Here, for illustration, we focus on the inversion evolution of subvectors representing two months of fluxes (specifically for November, 2001 and September, 2002).

Figures 4.4 and 4.5 show the inversion evolution of CH_3Cl surface fluxes for November, 2001 and September, 2002, respectively, with the use of subsequent monthly observations. Note that the plots do not show fluxes for different months, but how the estimates for a single month's fluxes change with each new month of data. As mentioned before, only one year of subsequent observations are used to constrain a single month's fluxes. The vertical axis is actually the adjustment to the reference value (all are unitless).

The initial value for each seasonal process is therefore zero with an a priori (blue) error bar defined by Equation (4.16), which means we start the inversion from the reference state. With each new observation, the adjustment changes and the error decreases. The amount of the decrease depends on the species and the emission region or process. Note that the changes and the error reductions for a given process are greatest in the first few months, because the strongest sensitivities of the observations to the emission pulse occur in the same time frame. In the following months, flux values and uncertainties stabilize even with the addition of new data. The optimized inversion results for November, 2001 and September, 2002 fluxes are the final values in the plots. These final values represent the adjustments to the reference fluxes that will provide a better fit to the observations. As noted earlier, because only 12 months' data have been used, these final values are phased out of the inversion and stored when a new subvector representing November, 2002 or September, 2003 fluxes enters the inversion process. After all of the months of observations have been utilized, we have computed the optimized adjustments over the entire period. These adjustments plus the reference values give the final, optimized estimates of the surface fluxes. The optimized estimates can be tested using a forward run of MATCH to help check the overall inversion results. These tests will be presented after the inversion results for each of the chloromethanes.

For all gases we also check the calculated error covariance matrix $\mathbf{P}$, and most of its off-diagonal elements are at least one order of magnitude less than the diagonal elements. The variables for different geographical regions are orthogonal to each other. We aggregate some regions to avoid possible large off-diagonal covariances. For example for

the inversion for the industrial emissions of CH_2Cl_2 we aggregate the European and Northwest Asian regions.

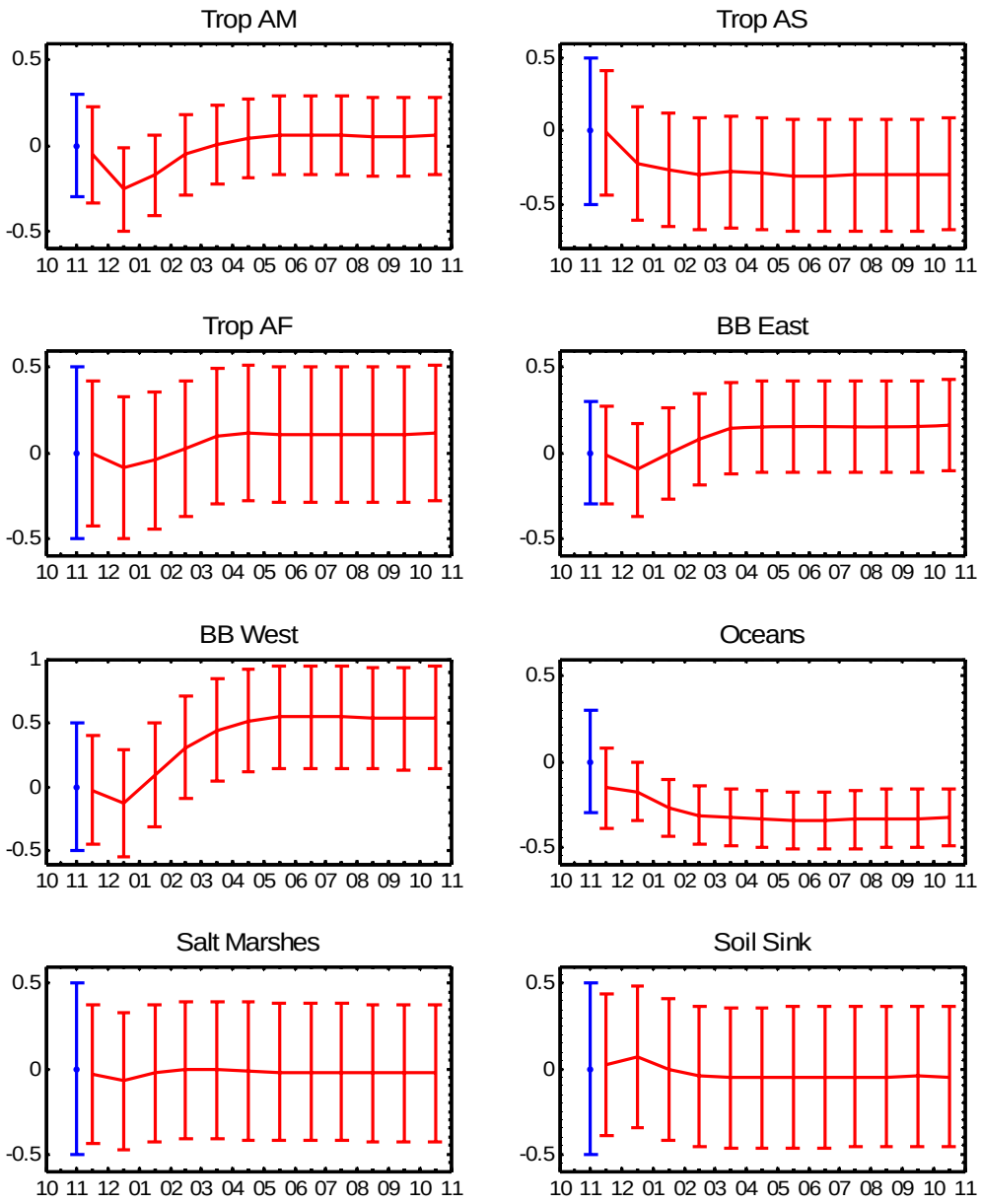

Figure 4.4. The inversion processes of methyl chloride surface fluxes for a single month (November, 2001) with the addition of monthly observations from November, 2001 to October, 2002 (horizontal axis). The vertical axis corresponds to the non-dimensional adjustment from the reference value (unity). The blue bars show the a priori errors for the November, 2001 surface fluxes. The final optimized results are taken as the values at the last step, at which time the inversion has clearly stabilized in all cases.

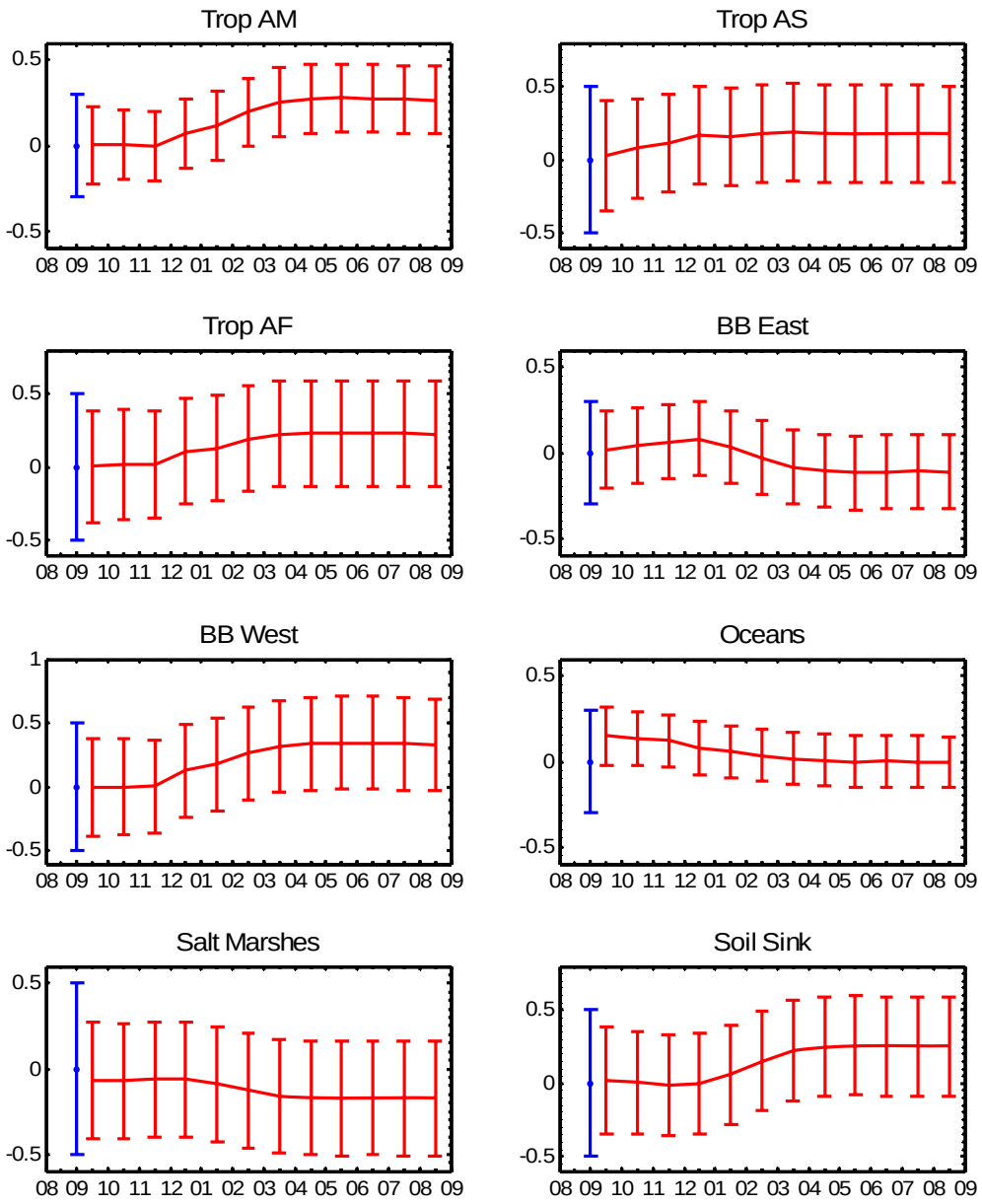

Figure 4.5. The inversion processes of methyl chloride surface fluxes for September, 2002 with the addition of monthly observations from September, 2002 to August, 2003 (horizontal axis).

Chapter 5

Inversion Results for Methyl Chloride

Methyl chloride (CH_3Cl) is the most abundant naturally produced contributor to stratospheric chlorine. Even with the existence of many anthropogenic chlorinated gases, CH_3Cl (together with $CHCl_3$) contributes about 20% of the stratospheric chlorine content [*Solomon et al*., 1995] and, as noted earlier, it is expected to increase in relative importance in the future as anthropogenic chlorine abundances decrease in response to recent emission regulations. The mean mole fraction of CH_3Cl in the remote troposphere is typically at about 550 ppt [*Yokouchi et al*., 2000b, 2002; *Cox et al*., 2003; *Simmonds et al*., 2004]. Measurements also show latitudinal variations in CH_3Cl concentrations, specifically with higher values in the tropics than the poles [570 v.s. 500 ppt, *Yokouchi et al*., 2000b], presumably caused by large tropical terrestrial sources. *Khalil and Rasmussen* [1999b] reported a seasonal cycle with an amplitude of about 10%, while *Cox et al*. [2003] found a clear but much smaller annual cycle with an amplitude of 25 ppt (5%), explicable mainly in terms of seasonal changes in the abundance of the hydroxyl (OH) radial, which is the dominant sink of CH_3Cl in the troposphere.

Mole fractions for methyl chloride were only 5-10% lower than present day in firn air from Antarctica dating back to the early 1900s [*Butler et al*., 1999], which is consistent with the presence of predominantly natural emissions. Recent research has focused on identifying and quantifying its natural sources and sinks, including newly identified sources from tropical plants that have been reported by *Yokouchi et al*. [2002]. The anthropogenic sources (coal combustion, incineration, and industrial processes) were quantified in the Reactive Chlorine Emissions Inventory [*McCulloch et al*., 1999] and sum to 160 Gg yr^{-1}, which is only 5.4% of the total estimated sources. Before 1996, the oceans were thought to be the dominant source of methyl chloride, accounting for 20% of the total. *Yokouchi et al*. [2002] later suggested that methyl chloride emissions from tropical plants might be the largest known source. They determined that a specific group of ferns and trees in Southeast Asia alone produce 910 Gg yr^{-1}, using the average emission rate from three species of Dipterocarpaceae and the leaf biomass reported for mature tropical lowland rainforest. Considering the large variability of CH_3Cl emissions among species of a family and among individual plants of a species, this estimation is regarded to have very great uncertainty. Moreover, only contributions from Dipterocarpaceae in Southeast Asia are listed in this inventory. What about CH_3Cl emission from Dipterocarpaceae all over the world, as well as other CH_3Cl-emitting tropical plants? This vegetation source certainly warrants additional investigation which is the goal of the inversions presented in this chapter.

Reaction with the OH free radical is the dominant pathway for removal of CH_3Cl from the atmosphere, resulting in a corresponding OH-removal lifetime of 1.5 years (this

"process" lifetime is defined as the total atmospheric content divided by the rate of removal by that process). Other minor loss processes include reaction with chlorine radicals in the marine boundary (13-year lifetime), microbially mediated uptake by soils (28-year lifetime), and uptake in polar oceans (70-year lifetime). These in total result in an atmospheric lifetime of about 1.3 years. The best estimate of the magnitude of the identified CH_3Cl sources is 26% less than the best estimate of the magnitude of the better quantified known sinks. This suggests that there are still missing and/or under-estimated CH_3Cl sources. Moreover, due to the complicated natural behavior of the known sources, significant uncertainties exist in their magnitudes and variability such as variations caused by seasonal and climate changes. Using a 3-D global model of atmospheric CH_3Cl, *Lee-Taylor et al*. [2001] were able to reproduce the observations of *Khalil and Rasmussen* [1999b] by adding a massive tropical terrestrial source of 2500 Gg yr^{-1} and reducing emissions from Southeast Asia. Any major as-yet-unidentified source must necessarily show a similar global distribution to be consistent with observations.

In this chapter, we present the inversion results for methyl chloride surface fluxes using the methodology described in Chapter 4. The optimized surface fluxes include seasonal, annual, and interannual values for specific emitting and depleting processes and regions. The raw inversion results are the 60 monthly surface flux values plus an aseasonal emission magnitude, from which the averaged seasonal and annual surface flux magnitudes are derived. The seasonal, annual and interannual inversion results are presented and discussed in sequence. We derive emission anomalies for 2002/2003 that appear to coincide with the 2002/2003 globally wide-spread heat and drought which was

partly caused by the 2002/2003 El Niño event. We also test the sensitivity of the inversion results to different combinations of the observations.

5.1. Definition of the state vector and its a priori flux maps

As described in the inverse modeling methodology, reference (a priori) flux distributions are necessary as the initial guesses for our unknown surface fluxes. In addition, the sensitivities of the model output variables (concentrations) with respect to input variables (surface flux magnitudes) must be computed by perturbing the reference surface fluxes in the Taylor expansion sense [Prinn, 2000]. It is important that the spatial distributions of the reference fluxes be as accurate as possible but not their magnitudes or time dependence.

Considerable effort has been put into estimating anthropogenic and natural emissions of reactive chlorine to the atmosphere [e.g., *Graedel and Keene*, 1995, 1996; *Singh*, 1995; *Khalil*, 1999; *Keene et al*., 1999]. The Reactive Chlorine Emissions Inventory (RCEI) carried out under the auspices of the International Global Atmospheric Chemistry Program's Global Emissions Inventory Activity (GEIA) [*Graedel and Keene*, 1999] is particularly notable. It provides high resolution (1º × 1º latitude, longitude) annual emission fields for major reactive tropospheric Cl species (including CH_3Cl, CH_2Cl_2, and $CHCl_3$) integrated across source types (terrestrial biogenic and ocean emissions, biomass burning, industrial emissions, fossil-fuel combustion, and incineration, etc.) for the reference year 1990. *Lee-Taylor et al*. [2001] modified and extended these estimates in their 3-D modeling of CH_3Cl by parameterizing month by month seasonal variations.

These emissions represent our best initial guess of CH_3Cl fluxes before optimization of individual processes to get emission estimates.

As suggested by *Yokouchi et al*. [2002] , methyl chloride emissions from tropical plants might be the largest known source, but it is not however included in this inventory. We assume in this study that tropical plants have a significant role in CH_3Cl production and incorporated this process into the inversion to estimate its magnitude and seasonality on regional scales. For our reference emissions we attribute the imbalance of the global CH_3Cl budget between known sources and sinks to this tropical plant process and distribute the resultant global magnitude proportionally to modeled net primary productivity (NPP) of tropical plant ecosystems [*McGuire et al*., 2001]. The measurements of *Yokouchi et al*. [2000b] show close correlations between local enhancements of CH_3Cl and of biogenic compounds emitted by tropical plants, and foliar emissions of the latter have been assumed proportional to foliar density, temperature, and available light [*Guenther et al*., 1995]. Therefore it is reasonable to assume that CH_3Cl fluxes are also proportional to foliar density of the emitting plants. *Guenther et al*. [1995] further assumed that foliar density is proportional to the net primary productivity of certain species. The monthly tropical plant NPP database ($0.5^o \times 0.5^o$ latitude, longitude) by *McGuire et al*. [2001] represents the net production of organic matter in tropical ecosystems and accounts for the influences by atmospheric CO_2, and seasonal and climatic changes in temperature, precipitation, and available light.

These flux maps have been interpolated to the MATCH T42 grid system (2.8º × 2.8º) while conserving their global magnitudes by using the SCRIP (Spherical Coordinate Remapping and Interpolation Package) software. Figures 5.1 and 5.2 show the annually averaged spatial distributions (T42) of the surface fluxes from tropical plants, oceans, biomass burning, anthropogenic activities, and other processes. As can be seen, most of the emissions are concentrated in the Northern Hemisphere. Tropical emissions are intensely located around the equator and are divided into three regions (America, Asia, and Africa) for our inversions. Emissions from biomass burning are further divided into Western (North and South America) and Eastern (Africa, Europe, Asia, and Australia) regions. Oceans are a source at lower latitudes and a sink at higher latitudes for methyl chloride and correction factors for its reference map are estimated globally. We also estimate correction factors for the maps of global emissions from salt marshes and the global uptake rates by soils (soil sink). Emissions from freshwater wetlands are very small and are kept at their reference values with assumed seasonal changes that are not estimated here. Seasonality of the fungal emissions is not considered here (as *Lee-Taylor et al*., [2001]) and its global emissions are solved as an aseasonal flux. The annual industry/incineration flux in the model is not estimated here because of its spatial correlation with the fungal emissions. The corresponding state vector at time k can be expressed as:

$$\mathbf{x}_k = \begin{bmatrix} \mathbf{X}_k^{as} \\ \mathbf{X}_k^{s} \\ \mathbf{X}_{k-1}^{s} \\ \cdots \\ \mathbf{X}_{k-T}^{s} \end{bmatrix} \tag{5.1}$$

where

$$\mathbf{X}_k^{as} = x_k^{fungal} \qquad \mathbf{X}_k^{s} = \begin{bmatrix} x_k^{tropam} \\ x_k^{tropas} \\ x_k^{tropaf} \\ x_k^{bbeast} \\ x_k^{bbwest} \\ x_k^{ocean} \\ x_k^{salt} \\ x_k^{soil} \end{bmatrix} \tag{5.2}$$

We use data and do estimates for the period from 2000 to 2004 (total of 60 months). The global magnitudes of the reference emissions and their mode of incorporation in the state vector are listed in Table 5.1. The a priori errors for the state vector elements are ± 30% to ± 50% of their reference values. Table 5.2 summarizes the surface sites whose measurements are used in the inversions for CH_3Cl. If we have both high frequency in situ data and low frequency flask data for the same site, we choose the high frequency measurements due to their capability to capture major variations in time (see Chapter 2 for more details).

Table 5.1. Reference annual average strengths of the sources and sink of atmospheric methyl chloride (CH_3Cl) and their participation in the inversion.

Source/Sink Type [reference]	Seasonality (Y/N ?)	Strength (Gg yr^{-1})	State Vector ?
Biomass burning [*Lobert et al*., 1999]	Y	918	Y (2 regions)
Wood-rotting fungi [*Watling and Harper*, 1998; *Khalil et al*., 1999]	N	128	Y
Industry/incineration [*McCulloch et al*., 1999]	N	162	N (reference)
Oceans, NCEP 10m winds [*Khalil et al*., 1999, etc.]	Y	477	Y
Salt marshes [*Rhew et al*., 2000]	Y	170	Y
Soil sink [*Keene et al*., 1999; *Khalil and Rasmussen*, 1999b]	Y	-256	Y
Freshwater wetlands [*Varner et al*., 1999]	Y	48	N (reference)
Tropical plants [*Yokouchi et al*., 2002]	Y	2089	Y (3 regions)
Net source (soil sink excluded)	Y	3992	-
Composite (soil sink subtracted)	Y	3736	-

Table 5.2. List of the stations whose measurements are used in the inversions for CH_3Cl, along with their corresponding numbers as in Table 2.1.

(1) MHD	(2) THD	(3) RPB	(5) CGO	(6) JUN
(7) MTE	(8) ZEP	(9) HAT	(10) BRW	(11) MLO
(12) NWR	(13) SMO	(14) SPO	(23) PSA	(21) KUM
(15) ALT	(17) LEF	(18) HFM		

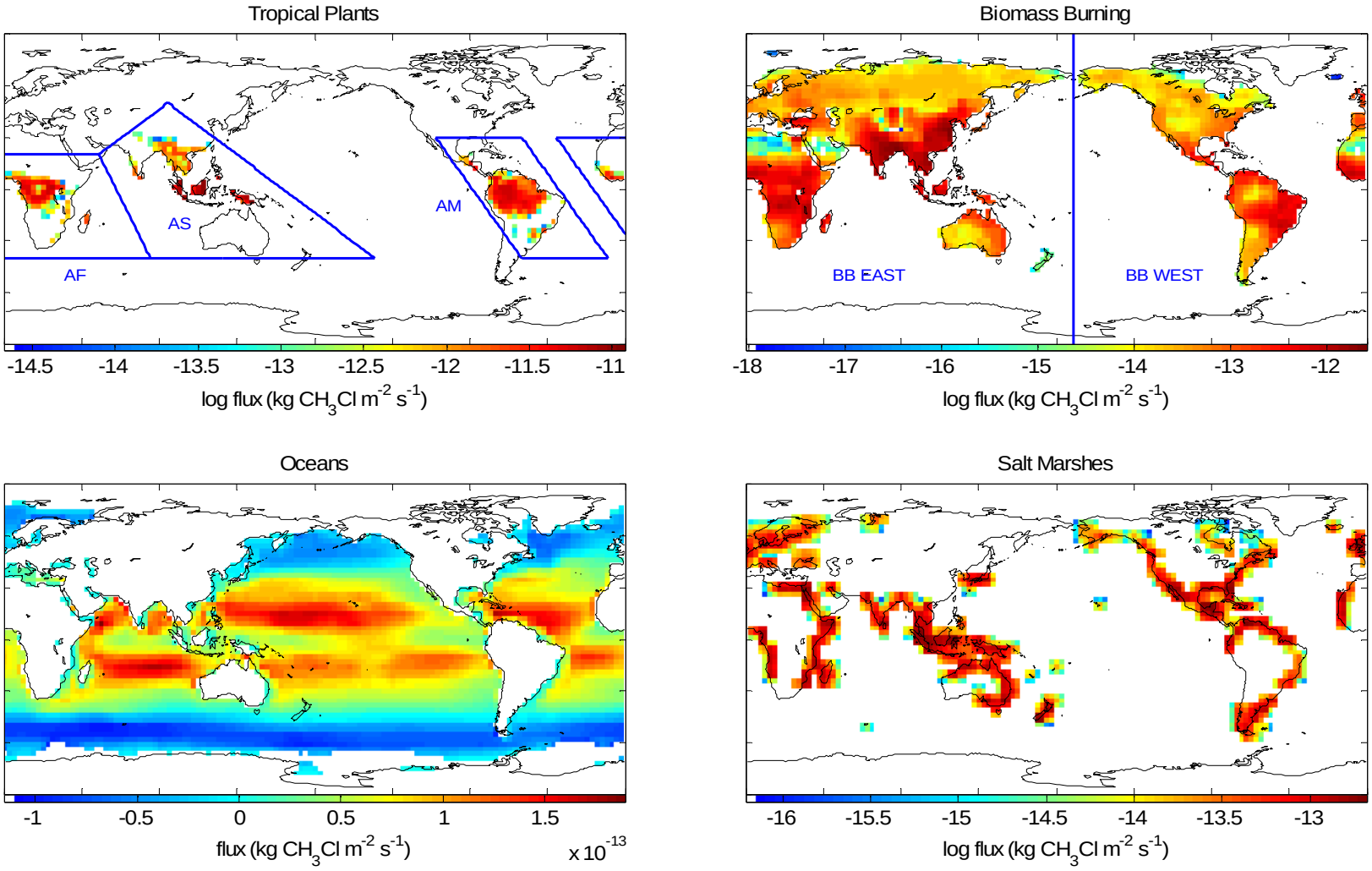

Figure 5.1. Annual average distributions of methyl chloride emissions. Emission magnitudes and patterns vary by month. Tropical plants (America, Asia, and Africa) and biomass burning (East and West) have been further subdivided for use in the inversion.

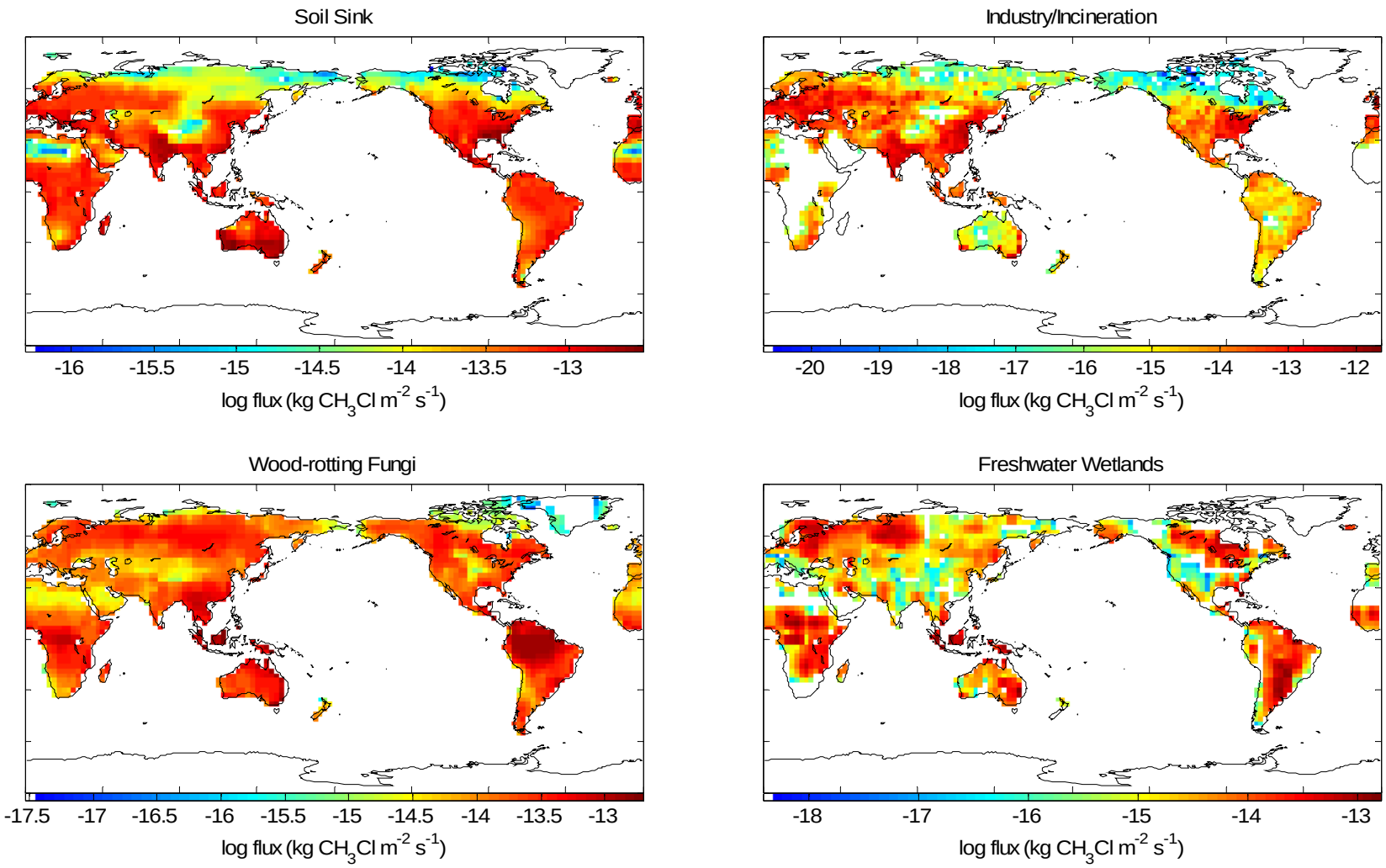

Figure 5.2. Annual average distributions of additional methyl chloride emissions and the soil sink. Note that industrial and wetland sources are assumed to be equal to their references and are not estimated. Seasonality of fungal emissions is not considered in the inversion.

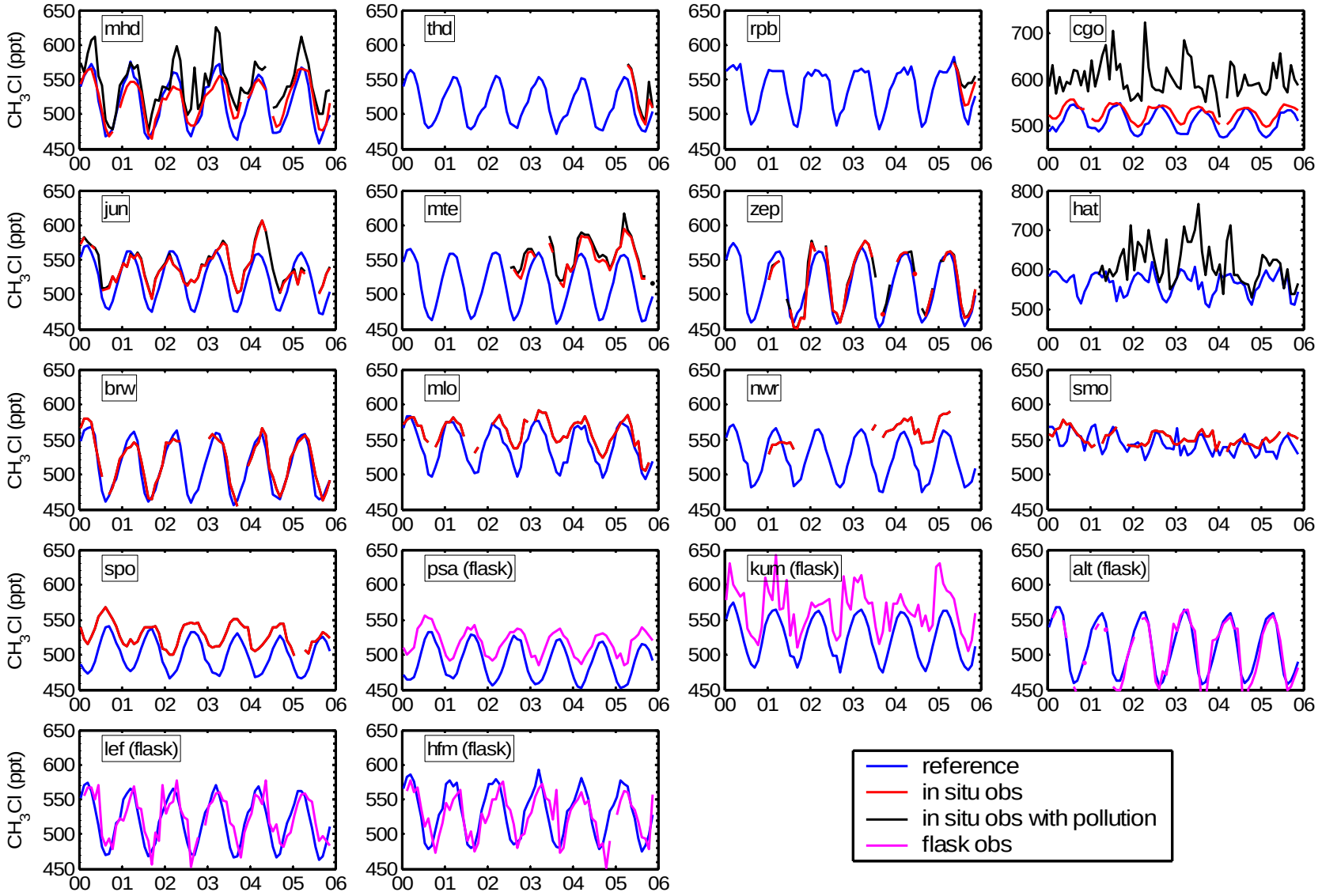

Figure 5.3. Time series of monthly mean methyl chloride mole fractions from a forward (reference) run of the MATCH model driven by the reference (a priori) surface fluxes are compared to the observations (with and without pollution events).

5.2. Forward modeling

A first step in this modeling study was to assess the ability of the a priori emission fields to reproduce methyl chloride observations, using the annually repeating sources and sink in forward runs of MATCH. We initialized the atmospheric 3-D distribution of CH_3Cl using the output from a previous multi-year run, scaled to fit the observed mole fractions at the remote sites such as Alert, Mauna Loa, and Cape Grim during January, 2000. These stations were chosen because they represent well the global background interhemispheric gradient due to their distance from strongly emitting sources. The reference run was then made from January, 2000 to November, 2005. The "perturbation" run accounting for sensitivities to the constant global fungal emissions was also made simultaneously using the method described in Chapter 4. Figure 5.3 shows the monthly mean modeled versus observed mole fractions of CH_3Cl at the indicated stations (with and without local pollution events) over the 6-year period of the simulation. As can be seen, MATCH at T42 can generally reproduce the seasonal cycles of CH_3Cl at most of the sites, with especially good fits at Pt. Barrow and Alert, but MATCH does not have the resolution to cope with local influences such as the pollution events at Cape Grim, Cape Kumukahi, WLEF tower, and Harvard Forest stations. Since industrial emissions (which are not estimated) usually dominate these pollution events, we have only used the data with pollution excluded in the inversion.

5.3. Inversion results

Figure 5.4 shows the optimized monthly fluxes (red lines) from January, 2000 to December, 2004, compared to the annually repeating reference values (blue lines). The inversion also simultaneously solved for the aseasonal fungal emissions as a constant. There are significant deviations from the reference case for some processes. Overall there are larger seasonal oscillations than the reference for almost all of the seasonal processes.

The optimized values also contain the full interannual variability in the fluxes. Among the interannual oscillations, the flux anomalies for the time period of late 2002 to late 2003 for several processes are worthy of notice. There were anomalous decreases of CH_3Cl emissions from all three tropical regions. There was anomalously high emission from the eastern biomass burning source in the late spring of the year 2003, and also an anomalous emission rise from global salt marshes in the summer of 2003. There was also an anomalous reduction in the global soil uptake in September of 2003.

These anomalies are likely to be attributed to the extreme 2002/2003 globally wide-spread heat and drought which was partly caused by the 2002/2003 El Niño event (the 2002/2003 El Niño event lasted from the September of 2002 to the August of 2003). Recent studies show a consistent link between El Niño and drought in the tropics [*Lyon*, 2004] and mid latitudes [*Zeng et al*., 2005b]. While the El Niño event during this time was moderate compared to the extreme 1997/1998 El Niño, the period 2002/2003 appears unusual with global land precipitation very low, leading to a very dry and hot condition [*Knorr et al*., 2007].

Ciais et al. [2005] find reduction in primary productivity apparently caused by the heat and drought in 2003. And this reduction in primary productivity is probably the cause of the reductions in tropical plant emissions because of the correlation of primary productivity and foliar emission as noted before [*Guenther et al*., 1995].

The extremely dry and hot season might also lead to increased insect damage to vegetation and increased susceptibility of the boreal biome to fire [*Kobak et al*., 1996; *Ayres and Lombardero*, 2000]. *Balzter et al*. [2005] show that 2002/2003 were the two years with the largest fire extent in Central Siberia since 1996 using measurements of burned forest area in Central Siberia (approx. 79-119ºE, 51-78ºN). This is the region within our Biomass Burning (BB) East map. These enhanced fire events are expected to emit more CH_3Cl than usual.

CH_3Cl is produced in coastal salt-marsh regions by vegetation or microflora intimately associated with the plants, with greater emissions in the growing season than in the non-growing season [*Rhew et al*., 2000]. For these regions, temperature plays a more dominant role than the moisture in plant growth, because tidal sea water provides the required soil moisture for the plant to grow. Therefore the anomalous hot summers might have led to increased plant growth in the summer of 2003, thus increasing the production of CH_3Cl.

CH_3Cl is degraded in soils by microbial activity. *Lee-Taylor et al*. [2001] parameterized soil uptake of CH_3Cl by assuming: proportionality to a methyl bromide (CH_3Br) soil sink extrapolation [*Lee-Taylor et al*., 1998]; observations of *Shorter et al*.

[1995]; and a microbial activity / soil temperature relationship [*Cleveland et al*., 1993; *Holland et al*., 1995] which assumes that the microbial activity is stronger at higher temperatures. This is why the reference global soil uptake rate is greatest in the summer of the Northern Hemisphere. However, the inversion indicates an unexpected decrease of the soil sink in the summer of 2003. The microbial activity / soil temperature relationship neglects the influence of the soil moisture on microbial activity and uptake efficiency. Laboratory and field experiments of *Shorter et al*. [1995] did show the general relationship of decreasing CH_3Br uptake activity with decreasing moisture and organic matter content. The period 2002/2003 appeared unusual with global land precipitation very low for only a moderate El Niño event. Therefore the anomalously low global soil uptake might have been caused by extremely widespread drought conditions in 2003, because extreme dryness might cause the microorganisms consuming CH_3Cl to be inactive.

The possible future climate change in the Northern Hemisphere, toward an increasingly dry and hot summer climate, may lead to increased susceptibility of the reduction in emissions from the tropical biosphere and in uptake by soils, and a rise of the emissions by salt marshes and biomass burning sources.

Figure 5.5 shows the corresponding uncertainties of the optimized estimates by superimposing the optimized (a posteriori) uncertainties (red bars) on top of the reference (a priori) uncertainties (blue bars). Note that the inversion always acts to reduce the initial uncertainty by amounts depending on the value of the observations in constraining each

emission process or region. Uncertainties for Trop AM and Oceans shrink the most, those for Trop AS, Trop AF, and BB East have some reductions, while the uncertainties for BB West, Salt Marshes, and Soil Sink have the least reductions.

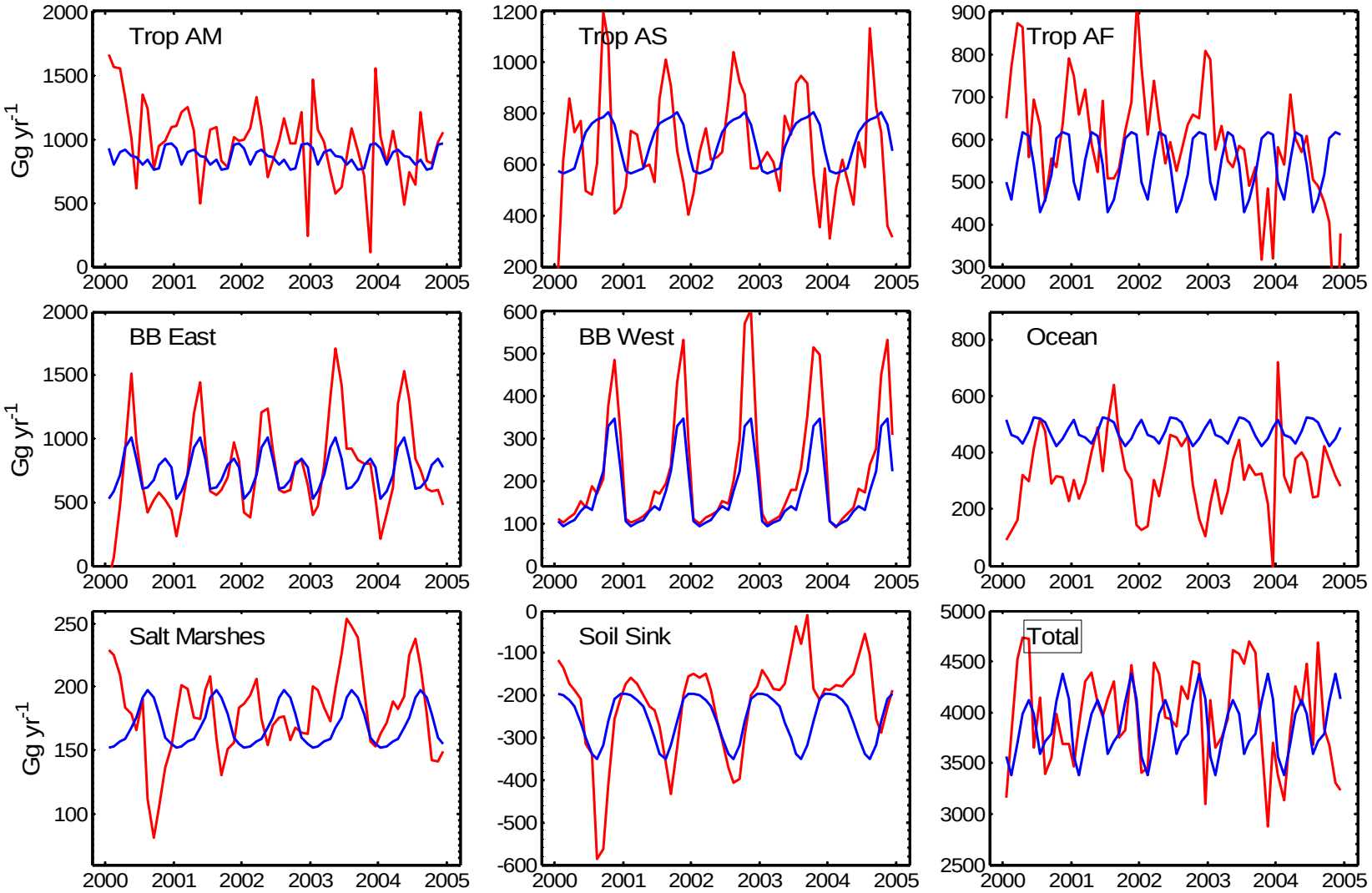

Figure 5.4. Inversion results for the seasonal processes for emissions of methyl chloride. Blue lines show the reference magnitudes, which are annually repeating. Red lines show the optimized estimates, which contain interannual variability. The total value is the sum of the eight seasonal processes plus the aseasonal fungal emission estimate and the reference industrial and wetland emissions.

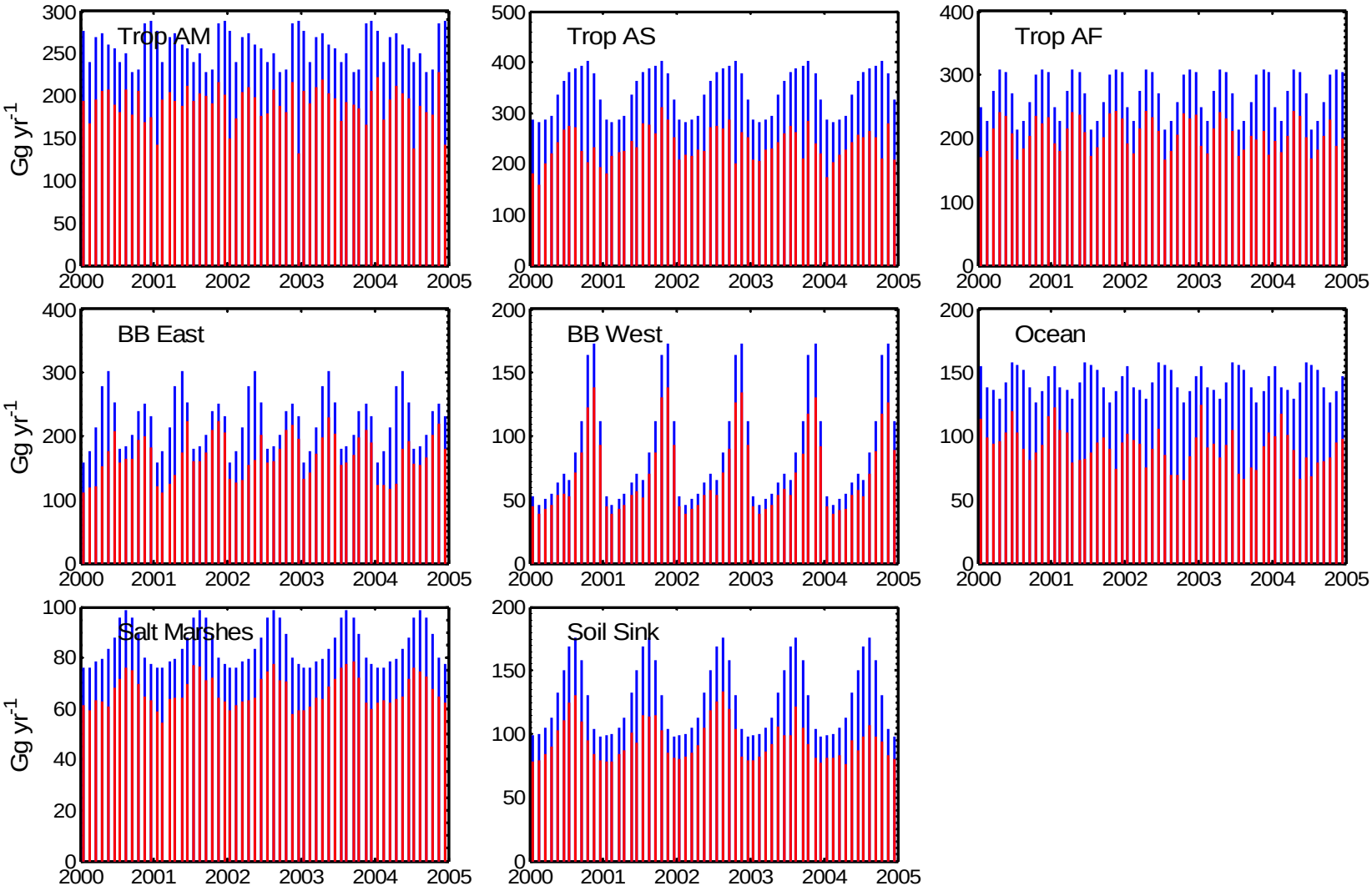

Figure 5.5. The corresponding uncertainties (1 σ error bars) of the inversion results in Figure 5.4, with the optimized error bars (red) superimposed upon the reference error bars (blue).

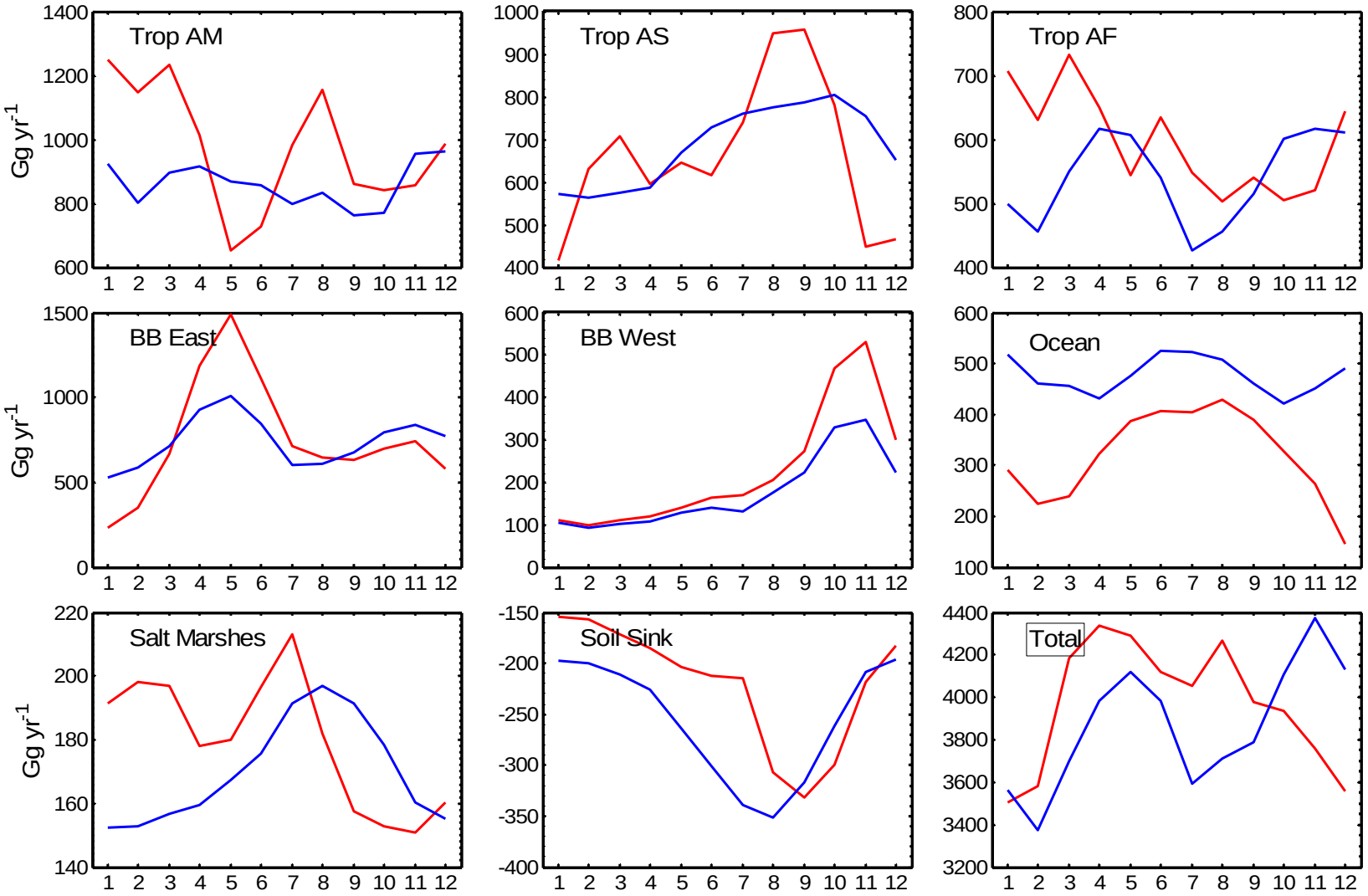

Figure 5.6. 5-year averaged seasonal results of methyl chloride. Blue lines show the reference magnitudes. Red lines show the optimized estimates.

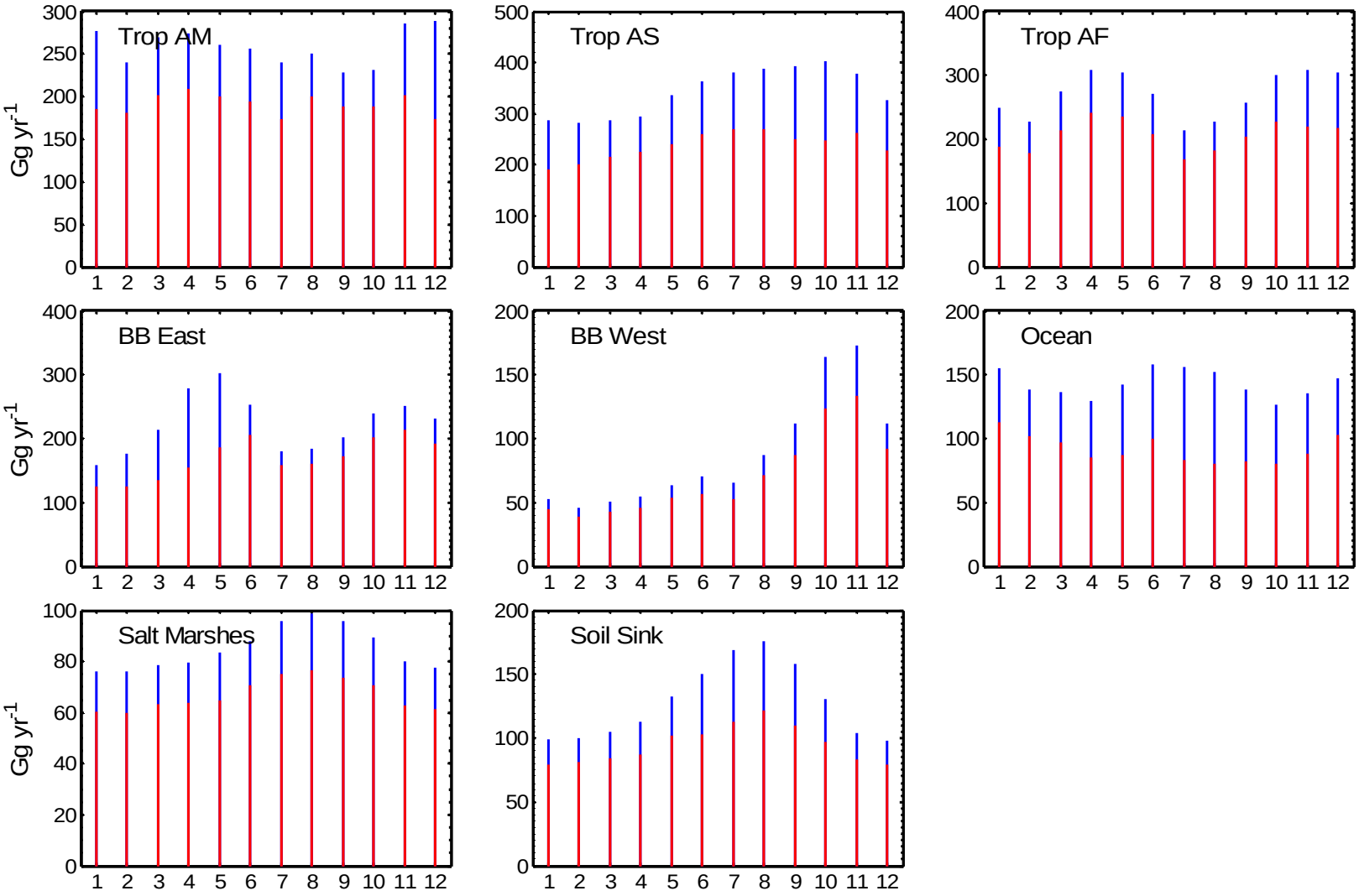

Figure 5.7. The corresponding uncertainties (1 σ error bars) of the inversion results in Figure 5.6, with the optimized error bars (red) superimposed upon the reference error bars (blue).

5.3.1. Average seasonal results

To show a single representative seasonal cycle of the seasonal processes, we take the arithmetic average of the five year results (i.e., the five Januarys are averaged to indicate a representative January, etc.). The corresponding associated uncertainties are estimated as:

$$\overline{\sigma}_t = \sqrt{\frac{\sum_{1}^{N} \sigma_{t,n}^2}{N}} \tag{5.3}$$

where t represents a particular month (e.g., January) and $n = 1$ to N = 5, for the five years of the inversion.

Figure 5.6 shows the averaged seasonal results (red lines) compared to the reference ones (blue lines), and Figure 5.7 shows their corresponding uncertainties as one standard deviations bars with the optimal ones (red bars) superimposed on top of the reference uncertainties (blue bars). For the tropical plant emissions, the seasonal variations generally retain their shapes for the three regions, with the most significant deviations from the reference values for the tropical American region. There are two tropical American emission peaks. One is in March (early spring) when the available sunlight is the strongest during the year at the equator, and the other is in August (summer) when the northern tropical temperature is the highest during the year. While tropical plants in the Africa have their strongest emissions in the spring, their summer emissions are least,

probably because in Africa it is a very dry season in summer and therefore the plant growth activities (NPP) are inhibited.

Biomass burning emissions are concentrated in tropical regions, especially India and Southeast Asia. To study the seasonal behavior of the biomass burning source, we first examine the partitioning of the seasonal cycles of the Eastern and Western biomass burning sources (Figure 5.6) into the Northern and Southern Hemispheres in Figure 5.8. Note that the spring (April and May) peak of the Eastern biomass burning source (BB East) comes from the Northern Hemisphere, and the October and November (Southern spring) emission peak comes from the Southern Hemispheric biomass burning region. The Western biomass burning emission peak in November (Southern spring) comes from Southern America. For both Hemispheres the biomass burning emissions are strongest during the spring term associated with dry conditions and therefore the amount of biomass burned is the largest [*Hao and Liu*, 1994]. The inversion enhanced the BB Eastern emission peak in the Northern Hemisphere in spring, and decreased the BB Eastern emission peak in the Southern Hemisphere in spring. The inversion also increased the BB Western emission peak in the Southern Hemisphere in spring.

Global ocean emissions generally retain the same seasonal variability as the reference values, but with an overall reduction. The highest emission rates occur during the summer, resulting from the combined effects of the monthly mean wind speeds and sea surface temperatures [*Lee-Taylor et al.*, 2001]. For the global salt marshes, its emission

peak shifts to be a little earlier (from August to July). Finally, the global soil sink peak shifts from August to September.

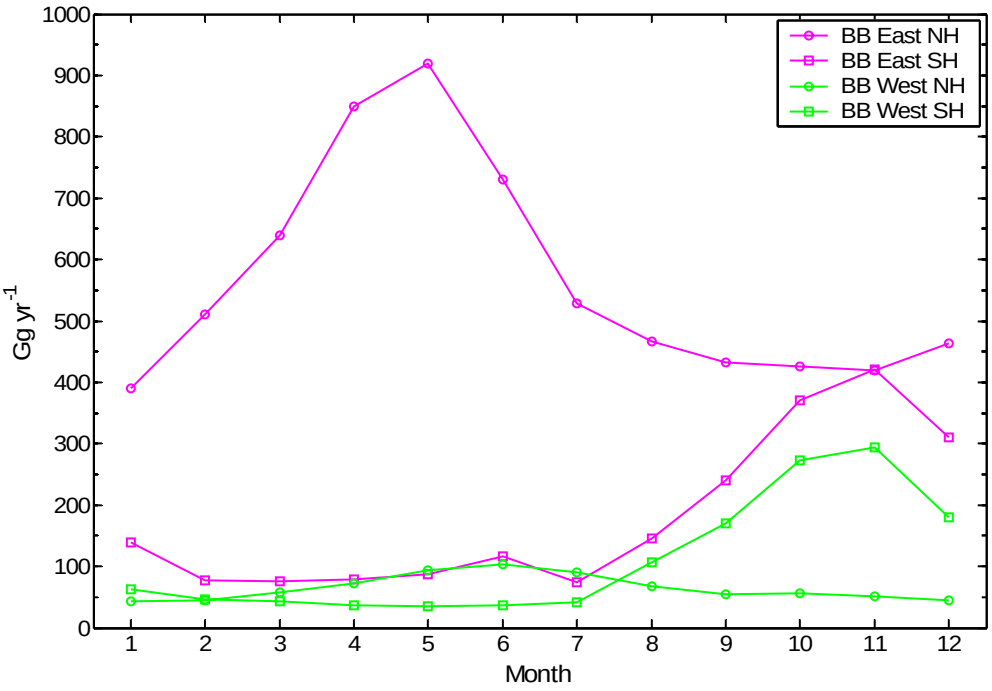

Figure 5.8. Partitioning of the seasonal cycles of the Eastern and Western biomass burning sources into the Northern and Southern Hemispheres. Note the dominance of the Eastern Northern Hemispheric emissions of methyl chloride. Also the emission peaks of the Northern and Southern Hemispheres occur in their respective springs consistent with dry conditions conducive to burning.

5.3.2. Average annual results

The inversion results are finally aggregated to illustrate the global budget of CH_3Cl. Figure 5.9 and Table 5.3 contain the CH_3Cl fluxes averaged over the entire period between 2000-2004. The total emissions in Table 5.3 are the sum of the estimated sources, the constant industrial source, and the annual average wetland emission magnitude (with soil sink excluded). We have aggregated individual processes into tropical plants and biomass burning emissions; their individual fluxes are listed in Table 5.4. The averages for the seasonal processes are derived by averaging the results shown in Figure 5.4. The inversion has directly solved the aseasonal process emissions as annually averaged differences from the reference. Figure 5.9 and Table 5.3 also include the optimized errors, which are always less than the reference errors due to their reduction by the observations in the Kalman filter. For the seasonal processes, Equation (5.3) has been extended to all months to determine the annual average errors. In Figure 5.9 the aseasonal uncertainty is taken from the last step of the Kalman filter. Note that the final error for the fungal emission estimate is much smaller than for the seasonal flux estimates. This is because the inversion solves the global fungal emission as a time-invariant variable over the entire period, thus allowing error reduction at every time step. Also, we have assumed a perfect model which leads to the system random errors to be zero. To better estimate the realistic uncertainty of the fungal emission estimate, we have multiplied the initial uncertainty of the fungal emission estimate by the averaged percentage standard deviation reduction computed for the eight seasonal processes/regions to obtain the final error estimate, as

shown in Table 5.3. The seasonal processes, in contrast, have been solved as monthly fluxes which already add greater uncertainty to their five-year averages.

The CH_3Cl inversion results indicate large CH_3Cl emissions of 2240 ± 370 Gg yr^{-1} from tropical plants, which account for 53.4% of the total emissions. The second largest emissions come from biomass burning accounting for 23.4%. The other source strengths are relatively small, and their percentages are 7.6% for the oceans, 6.2% for the fungi, 4.3% for the salt marshes, 3.9% for the industry/incineration, and 1.1% for the wetlands. The total global emissions are ~ 4200 Gg yr^{-1}. Relative to their a priori magnitudes, the inversion nearly doubles global fungal emissions, slightly increases emissions from tropical plants, biomass burning and salt marshes, and reduces the global ocean source and soil sink.

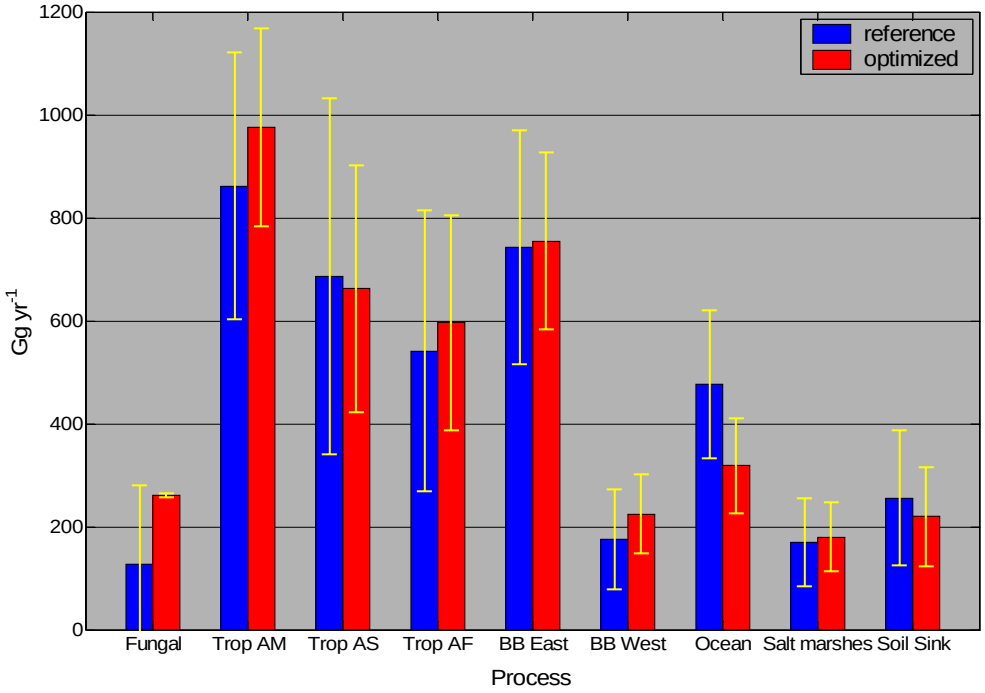

Figure 5.9. Annual average methyl chloride surface flux magnitudes. Shown are the reference (blue bars) and optimized (red bars) values with their 1 σ error bars (yellow). The errors on the references are the assumed a priori inversion uncertainties.

We also tested the sensitivity of the inversion results to different combinations of the observations used in the Kalman filter. Inversion with the AGAGE observations only has the least effect in modifying the a priori surface flux magnitudes, and the error reductions are the least. This is because there are only two AGAGE stations with CH_3Cl data (Mace Head and Cape Grim) during most of the inversion period (see Figure 5.3). Inversion using the data from only the NOAA flask sites has the second least error reductions,

because we have added great errors to these low frequency measurements, thus much lowering their influence in determining the optimal surface fluxes (see Section 2.2).

5.4. Inversion check

The forward model has been run with the final optimal emission estimates, and the predicted mole fractions have been compared with the measurements. Figure 5.10 shows the residuals between the optimized and observed monthly mean mole fractions, compared to the residuals between the reference and observed monthly mean mole fractions at each observing site. The optimization lowers the residuals at some but not all the sites.

5.5. Summary and conclusions

We solved for seasonal, annual, and interannual surface fluxes of methyl chloride during 2000-2004 using the measurements from the AGAGE, NOAA-GMD, SOGE, and NIES sampling networks, a 3-D global chemical transport model, and the Kalman filter. The state vector in the Kalman filter includes scaling factors which multiply the a priori values of the unknown variables at monthly resolution. Then the optimal emission estimates were input into the model to check the inversion results.

Large CH_3Cl emissions of ~ 2240 Gg yr^{-1} are estimated for tropical plants. Relative to their a priori magnitudes, the inversion nearly doubles global fungal emissions, slightly increases emissions from tropical plants, biomass burning and salt marshes, and reduces the global ocean source and soil sink. The inversion implies greater seasonal oscillations

of the natural sources and sink of CH_3Cl compared to the a priori values. The inversion also exhibits strong effects of the 2002/2003 globally wide-spread heat episodes and droughts on the global emissions from tropical plants, eastern region biomass burning, global salt marshes, and on the global soil sink. The 2002/2003 El Niño event was a moderate one compared to the 1997/1998 event, while the global land precipitation appeared unusually low. There is evidence showing that the global land dryness leads to a strong NPP decrease and this is expected to lead to the subsequent decrease in emissions from tropical plants. The anomalously dry and hot climate may also lead to increased insect damage to vegetation and increased susceptibility of the biomass to large-scale burning, resulting in a decrease in global soil consumption and an increase in global biomass burning emissions of CH_3Cl. Possible future climate change involving increasingly dry and hot summers may lead to increased occurrence of decreased NPP (and hence decreased tropical CH_3Cl emissions), increased biomass burning, increased salt marsh plant growth, and decreased soil organic matter and microbial activity (and hence the corresponding effects on CH_3Cl surface fluxes).

Table 5.3. Five-year averaged optimal surface flux values and errors for aseasonal and seasonal processes (units of Gg yr^{-1}).

Flux type	Reference	In situ + NOAA flask (5 sites)	All without SPO	in situ	in situ without SPO	Only AGAGE (2 sites)	Only NOAA flask (13 sites)	in situ without NIES	in situ without SOGE
Fungal	128 ± 153	216 ± 109	157 ± 111	261 ± 112	186 ± 114	190 ± 133	91 ± 121	261 ± 112	273 ± 112
Tropical	2089 ± 511	2337 ± 366	2191 ± 372	2235 ± 371	2078 ± 378	2126 ± 436	2360 ± 406	2235 ± 372	2208 ± 372
Bio. Burn.	918 ± 247	932 ± 182	985 ± 184	979 ± 188	1029 ± 192	912 ± 226	921 ± 201	979 ± 188	989 ± 189
Oceans	477 ± 143	341 ± 85	455 ± 92	319 ± 92	465 ± 106	475 ± 134	480 ± 106	319 ± 92	319 ± 93
Salt marsh	170 ± 85	169 ± 66	166 ± 67	180 ± 67	175 ± 68	171 ± 69	171 ± 68	180 ± 67	181 ± 67
Soil sink	-256 ± 131	-250 ± 87	-240 ± 88	-220 ± 96	-215 ± 97	-258 ± 108	-260 ± 89	-220 ± 96	-217 ± 97
Total Emi.	3992	4205	4164	4184	4143	4084	4233	4184	4180

Table 5.4. Five-year averaged individual optimal values and their errors for emissions from tropical plants and biomass burning in Table 5.3. All values are in Gg yr^{-1}.

Flux type	Reference	In situ + NOAA flask (5 sites)	All without SPO	in situ	in situ without SPO	Only AGAGE (2 sites)	Only NOAA flask (13 sites)	in situ without NIES	in situ without SOGE
Trop AM	862 ± 259	1033 ± 189	903 ± 193	976 ± 192	837 ± 198	887 ± 239	1000 ± 221	976 ± 192	962 ± 192
Trop AS	686 ± 346	680 ± 236	723 ± 239	662 ± 240	708 ± 244	689 ± 285	753 ± 262	662 ± 240	656 ± 240
Trop AF	541 ± 273	624 ± 207	565 ± 209	597 ± 208	533 ± 211	550 ± 227	607 ± 218	597 ± 209	590 ± 209
BB East	743 ± 227	709 ± 167	797 ± 169	754 ± 172	842 ± 175	731 ± 211	723 ± 187	754 ± 172	767 ± 173
BB West	175 ± 97	223 ± 73	188 ± 74	225 ± 77	187 ± 79	181 ± 81	198 ± 73	225 ± 77	222 ± 77

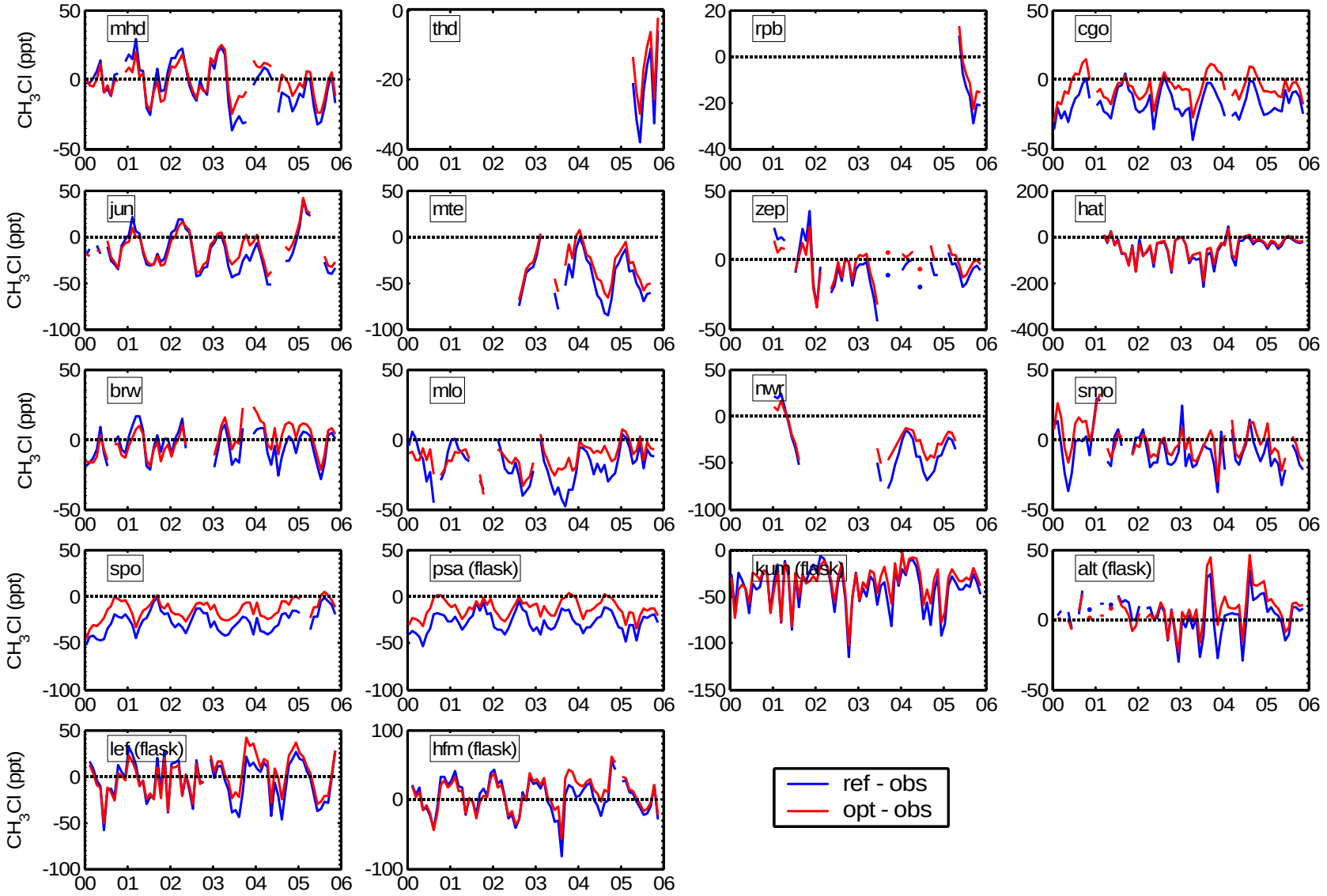

Figure 5.10. Residuals between the optimized and observed monthly mean mole fractions of methyl chloride (red lines), compared to the residuals between the reference and observed monthly mean mole fractions (blue lines) at each observing site.

Chapter 6

Inverse Results for Chloroform

Chloroform ($CHCl_3$) is one of several chlorine-containing gases in the atmosphere that are, individually, small contributors to the global chlorine budget, but become significant if taken together. The globally averaged mole fraction of chloroform at the earth's surface was previously reported to be about 18.5 ppt contributing about 60 ppt of chlorine to the lower troposphere and about 40 ppt of chlorine to the total troposphere [*Khalil and Rasmussen*, 1999a]. Later measurements from the AGAGE network during 1994-1998 show a much lower global average baseline concentration of 8.9 ± 0.1 ppt with no appreciable trend [*O'Doherty et al*., 2001]. The Northern Hemispheric (NH) mixing ratios of $CHCl_3$ are about twice as high as its southern hemisphere (SH) values [*Elkins et al*., 1998; *Khalil and Rasmussen*, 1999a; *O'Doherty et al*., 2001]. These observations also show that $CHCl_3$ has a very pronounced seasonal cycle with a summer minimum and winter maximum, presumably resulting from enhanced destruction by OH in the summer. The amplitude of the cycle is dependent on the sampling location.

The chloroform flux into the atmosphere was estimated to be approximately constant at some 630 Gg yr^{-1} by *Keene et al*. [1999]. About 90% of chloroform emissions are of natural origin: the largest single source appears to be in offshore seawater (contributing about 360 Gg yr^{-1}), presumed to be natural, but from an undefined biological process [*Khalil et al*., 1999]. Soil processes are the next most important source and the formation of chloroform has been shown to depend on oxidation of humic material in the presence of chloroperoxidase enzymes and chloride ions [*Hoekstra et al*., 1998a, b]. Rice fields and termite bearing soils have been identified as $CHCl_3$ sources [*Khalil et al*., 1990, 1998]. The world's soils contribute about 200 Gg yr^{-1} [*Khalil et al*., 1999]. The industrial sources total 66 Gg yr^{-1} [*Aucott et al*., 1999] and are predominantly the result of using strong oxidizing agents on organic material in the presence of chloride ions, which is a direct parallel with the natural processes occurring in soils. The wool pulp and paper industry, together with drinking and other water treatments, account for about 55 Gg yr^{-1} and the chemical and pharmaceutical industries account for the remainder. *Khalil and Rasmussen* [1999a] estimated that the global emissions are around 470 Gg yr^{-1} to balance the calculated losses due to OH and stratospheric destruction using the observed concentrations, which is much less than the composite global emission estimate of 630 Gg yr^{-1} [*Keene et al*., 1999]. Using a 2-D 12-box model and the AGAGE observations, *O'Doherty et al*. [2001] optimally estimated that 64 ± 5% of the emissions originate from the NH, supporting a larger role for land based soil sources (largely NH) and/or a diminished role for oceanic sources (largely SH). This disagreement with the previously

reported high oceanic emission estimates shows that our understanding of the sources of chloroform is still incomplete.

Chloroform has a short, but uncertain, tropospheric lifetime of about 0.5 year, and as such, less than 2% of the $CHCl_3$ emitted at the earth's surface reaches the lower stratosphere to deplete stratospheric ozone [*Kindler et al.*, 1995]. $CHCl_3$ also has a low global warming potential [*Solomon et al.*, 1995]. For these reasons, and its largely natural origin, $CHCl_3$ has not been included in either the Montreal or Kyoto Protocols. The principal removal process from the environment is atmospheric oxidation by the OH free radical. Chloroform is also removed by anaerobic and aerobic soil microorganisms and, although not important to the global balance, this can have a significant effect on local concentrations in soils that cannot equilibrate quickly with the atmosphere. The best estimated magnitude of the composite identified $CHCl_3$ sources is 37% greater than the better quantified known OH sink [*Cox et al.*, 2003], suggesting the current strengths of one or more $CHCl_3$ sources are overestimated.

In this chapter we present and discuss the inversion results for the natural surface fluxes of chloroform ($CHCl_3$) in a similar format to Chapter 5.

6.1. Definition of the state vector and its a priori flux maps

Years of evidence show significant natural origins of some or most of the chloroform found in the atmosphere, as well as industrial sources. There are however very few chloroform flux measurements carried out to date. The Reactive Chlorine Emissions

Inventory (RCEI) under the auspices of the International Global Atmospheric Chemistry Program's Global Emissions Inventory Activity (GEIA) [*Graedel and Keene*, 1999] provides high resolution (1º × 1º latitude, longitude) annual emission fields for biomass burning and anthropogenic industrial sources for the reference year of 1990. We have converted these maps to MATCH T42 grids (Figure 6.1) and imposed seasonality on the biomass burning source by assuming proportionality to the seasonality of methyl chloride (CH_3Cl) biomass fuel emissions [*Lee-Taylor et al*., 2001]. This is a reasonable analogy because both $CHCl_3$ and CH_3Cl emissions are approximately correlated with CO and CO_2 emissions [*Lobert et al*., 1999] and therefore they are correlated with each other also. We assume constant industrial emissions for $CHCl_3$.

Although the oceans and soils are the largest sources of chloroform, their relative roles in the global budget of $CHCl_3$ are poorly known. *O'Doherty et al*. [2001] and *Khalil et al*. [1999] have contrary conclusions on whether the oceans or the soils are the dominant source of $CHCl_3$. Although *Khalil et al*. [1999] provide some information on the semihemispheric distributions of the oceanic and soil sources, the inferred global chloroform source is larger than the global sink. We adjust these semihemispheric oceanic and soil sources by a single factor (~ 69%) [*Cox et al*., 2003] to roughly balance the calculated losses using the observed concentrations [*Khalil and Rasmussen*, 1999a] and take them as our reference values. For the oceanic emissions we distribute them evenly to the MATCH T42 grids within each semihemisphere (Figure 6.1). For the microbially-related soil emissions we assume a spatial analogy with the microbial soil sink of methyl chloride within each semihemisphere, because both processes have a

common dominating factor – temperature, and the soils consuming high CH_3Cl (which means the microbial activity is strong) would emit high $CHCl_3$ whose process also depends on microbial enzyme activity. Moreover, CH_3Cl taken up by the soils could provide more of the required chloride ions to produce $CHCl_3$. There assumptions are subject to verification by soil flux measurements.

It is likely that the natural production processes in soils would be species dependent and seasonal. For example, chloroform release from termite mounds showed a seasonal dependence with significantly lower emissions during the winter [*Laturnus et al*., 2002]. It is also reasonable to assume that enzymatic activities that facilitate the formation of reactive chlorine species are stronger during the warmer seasons. Therefore, we impose a seasonality on the soil source of chloroform by assuming proportionality to the seasonality of the soil sink of methyl chloride (CH_3Cl) [*Lee-Taylor et al*., 2001], with the latter assuming a positive microbial activity / soil temperature relationship. Since there is little information on the seasonal variability of the oceanic emissions of $CHCl_3$, we assume constant intra-annual emission rates in our reference model but allow seasonality in the subsequent inversions.

Figure 6.1 shows the annual average distributions of the $CHCl_3$ emissions from the four source types. The biomass burning emissions are concentrated in tropical regions, especially in India, Southeast Asia, Central Africa, and South America. The industrial emissions are mainly from the Northern Hemisphere, especially from India, Southeast Asia, Europe, and Northeastern America.

The dominant $CHCl_3$ removal process in the troposphere is reaction with the hydroxyl (OH) radical, accounting for more than 98% of the total destruction rate [*Keene et al*., 1999]. This process is simulated using the 3-D OH fields in the MATCH model. The same OH fields also account for most of the destruction in the stratosphere.

Given the spatial resolution of the available best estimates and the availability of the observations, we also estimate the oceanic and soil emissions on a semihemispheric scale at a monthly resolution. Within each semihemispheric region, the spatial distributions (but not magnitudes) of the source types remain at their reference distributions. We estimate global monthly biomass burning source strengths despite its small contribution to the global source strength [*Lobert et al*., 1999] because we expect significant month to month variations. The global industrial emissions are kept at their reference values, because of their expected relatively small time variations and their spatial correlation with the soil distributions. Therefore, the state vector at time k can be expressed as:

$$\mathbf{x}_k = \begin{bmatrix} \mathbf{X}^s_k \\ \mathbf{X}^s_{k-1} \\ \cdots \\ \mathbf{X}^s_{k-T} \end{bmatrix} \tag{6.1}$$

where

$$\mathbf{X}_k^s = \begin{bmatrix} x_k^{\text{Bio Burn}} \\ x_k^{\text{HNH Ocean}} \\ x_k^{\text{LNH Ocean}} \\ x_k^{\text{LSH Ocean}} \\ x_k^{\text{HSH Ocean}} \\ x_k^{\text{HNH Soil}} \\ x_k^{\text{LNH Soil}} \\ x_k^{\text{LSH Soil}} \\ x_k^{\text{HSH Soil}} \end{bmatrix} \tag{6.2}$$

for the period from 2000 to 2004 (i.e., k=1 to 60 months). The terms "HNH" and "LNH" denote higher (30º - 90º) and lower (0º - 30º) latitude Northern Hemisphere, and "HSH" and "LSH" denote higher (30º - 90º) and lower (0º - 30º) latitude Southern Hemisphere. The global magnitudes of the reference emissions and their involvement in the state vector are listed in Table 6.1. The a priori errors for the state vector elements are ubiquitously ± 100% of their reference values, which encompass the uncertainty ranges in most of the literature. Table 6.2 lists the surface sites whose measurements are used in the inversions for $CHCl_3$.

Table 6.1. Reference annual average strengths of the sources of atmospheric chloroform ($CHCl_3$) and their participation in the inversion.

Source/Sink Type [reference]	Seasonality (Y/N ?)	Strength (Gg yr^{-1})	State Vector ?
Biomass burning [*Lobert et al*., 1999]	Y	2	Y
Industry [*Aucott et al*., 1999]	N	64	N (reference)
Oceans [*Khalil et al*., 1999, adjusted]	Y	252	Y (4 regions)
Soils [*Khalil et al*., 1999, adjusted]	Y	141	Y (4 regions)
Composite	Y	459	-

Table 6.2. List of the stations whose measurements are used in the inversions for $CHCl_3$, along with their corresponding numbers as in Table 2.1.

(1) MHD	(2) THD	(3) RPB	(5) CGO	(6) JUN
(7) MTE	(8) ZEP	(9) HAT	(16) BRW	(20) MLO
(19) NWR	(22) SMO	(24) SPO	(23) PSA	(21) KUM
(15) ALT	(17) LEF	(18) HFM		

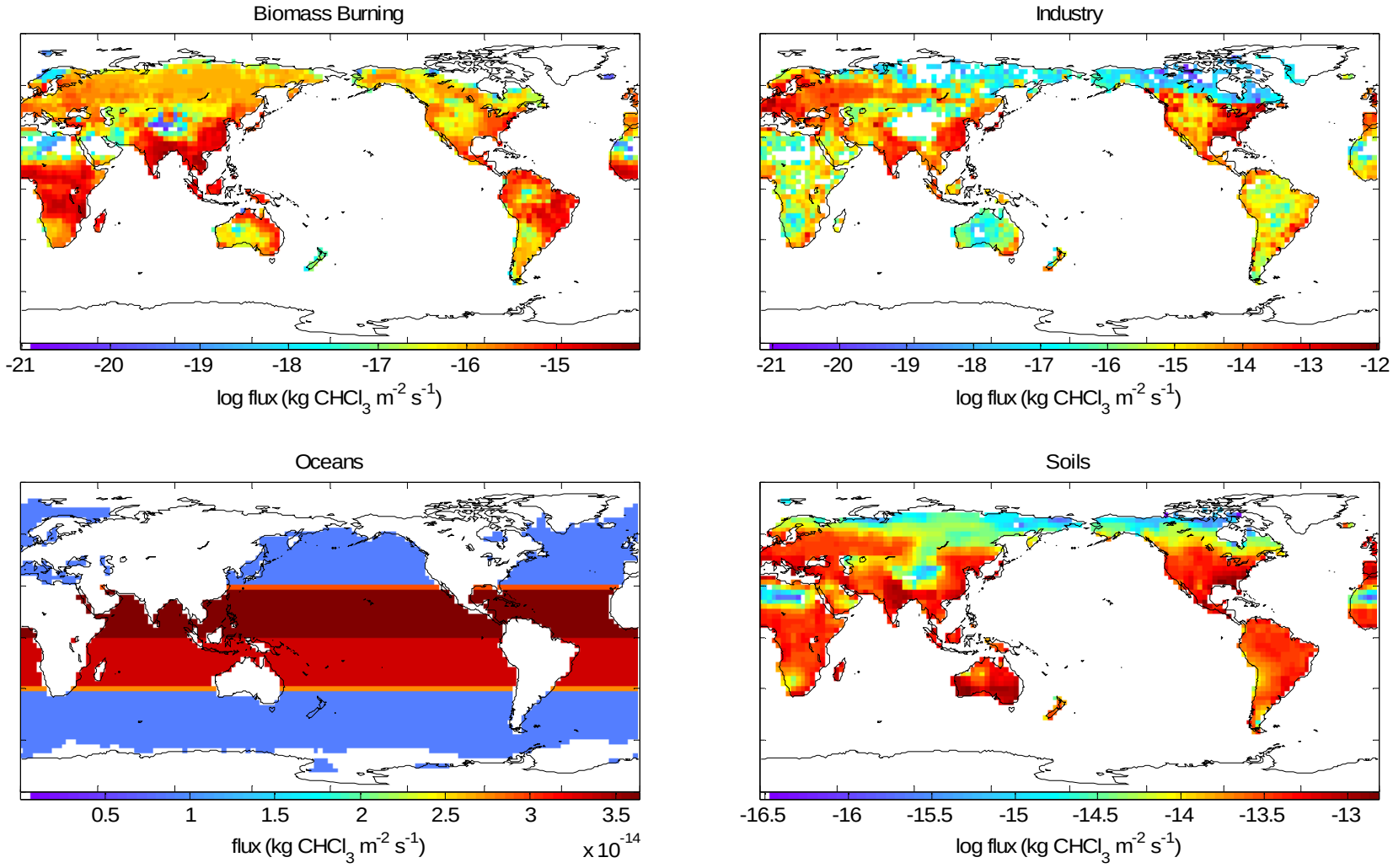

Figure 6.1. Annual average distributions of chloroform emissions. Emission magnitudes and patterns vary by month. Global oceanic and soil emissions have been further divided into semihemispheric regions in the inversion.

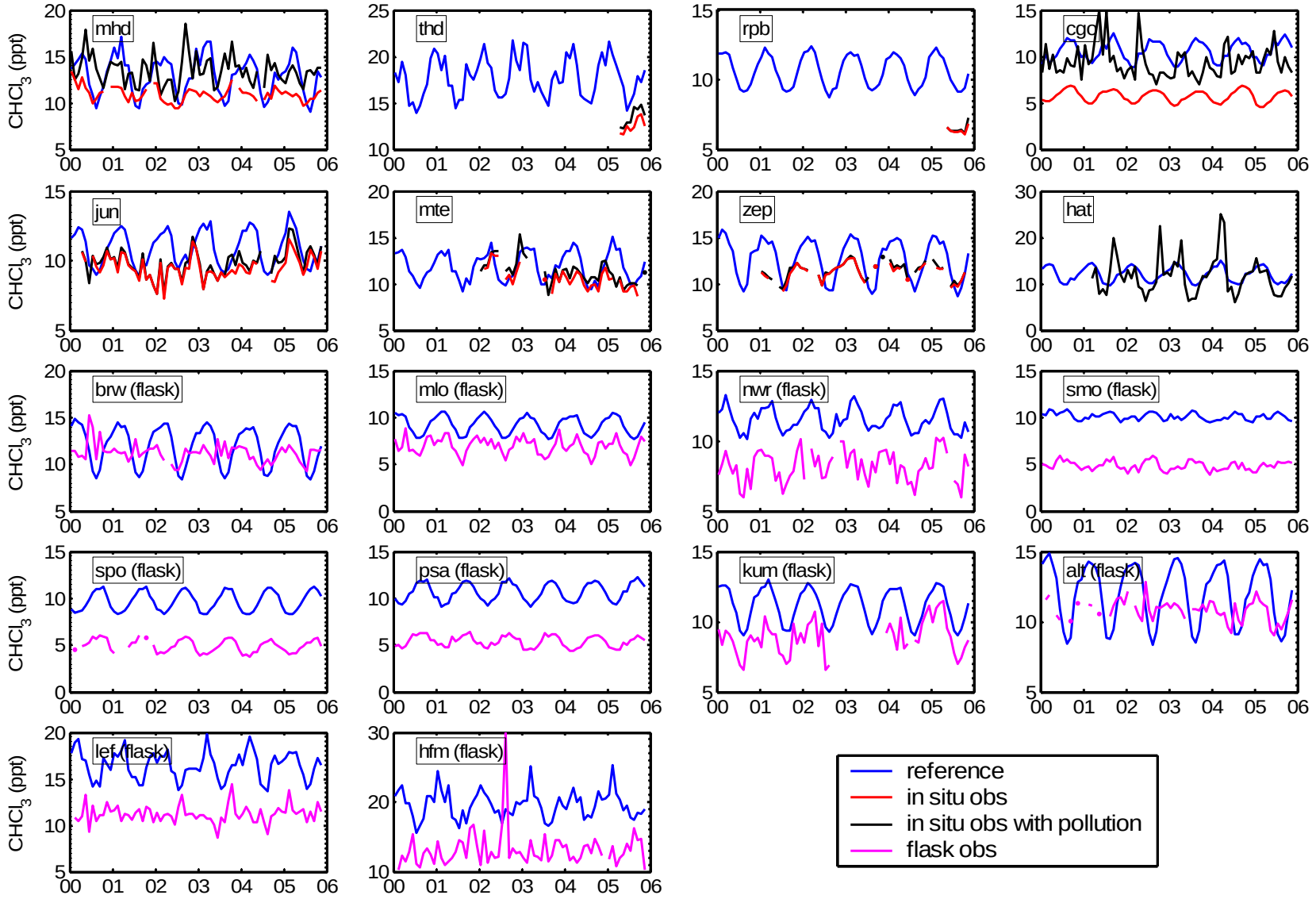

Figure 6.2. Time series of monthly mean chloroform mole fractions from the reference model using the a priori surface fluxes versus the observations.

6.2. Forward modeling

A first step in this modeling study was to assess the ability of the a priori emission fields to reproduce chloroform observations, by using these annually repeating reference sources in the forward runs of MATCH. We initialized the atmospheric 3-D distribution of $CHCl_3$ using the output from a previous multi-year run, scaled to fit the observed mole fractions at remote sites such as Alert, Mauna Loa, and Cape Grim during January, 2000. These stations were chosen because they represent well the global background interhemispheric gradient due to their long distance from strongly emitting sources. The reference run was then made from January, 2000 till November, 2005. Figure 6.2 shows the monthly mean modeled versus observed mole fractions of $CHCl_3$ at the indicated stations over the 6-year period of simulation. The model overall substantially overestimated the concentrations of $CHCl_3$, which indicated that the reference emission magnitudes derived from *Khalil and Rasmussen*'s [1999a] observations still overestimated one or more sources.

6.3. Inversion results

Figure 6.3 shows the optimized monthly fluxes (red lines) from January, 2000 to December, 2004, compared to the annually repeating reference values (blue lines). Overall there is not much update of the global biomass burning source strengths. The update of a particular emission-related element of the state vector is dependant on the sensitivity of the observations to that element. The small contribution of the biomass

burning emissions to the global $CHCl_3$ budget makes the sensitivity to this process very small. Therefore, it is not surprising that the global biomass burning source did not see much improvement. There are significant deviations from the reference cases for the semihemispheric oceanic sources and soil sources. Note that we used constant annual oceanic emission rates in our reference model, while the inversion results show obvious seasonal variations during the five years within each semihemisphere.

Figure 6.4 shows the corresponding uncertainties of the optimized estimates by superimposing the optimized uncertainties (red bars) on top of the reference uncertainties (blue bars). Note that the inversion always acts to reduce the initial uncertainties by amounts depending on the value of the observations in constraining each emission process or region. There are only small error reductions for the global biomass burning sources.

The optimized values also show interannual variability in the fluxes. The inversion shows summer high and winter low oceanic emissions in both the HNH and HSH. Given the relationship between saturation anomaly and sea surface temperature (SST), higher SST in the summer should cause larger emissions. Note the anomalously high oceanic flux in the HNH for the two summers of 2002/2003, which might have been caused by the high sea surface temperature anomalies during the 2002/2003 El Niño event [*Knorr et al.*, 2007]. The low emission anomalies from the HNH and LNH soils in the summer of 2003 and from the LSH and HSH soils in the winters (SH) of 2002 and 2003 might have also been caused by the extreme droughts in these two consecutive years, since extreme

dryness might have caused the microbial activity to be unusually weak and organic matter to be decreased.

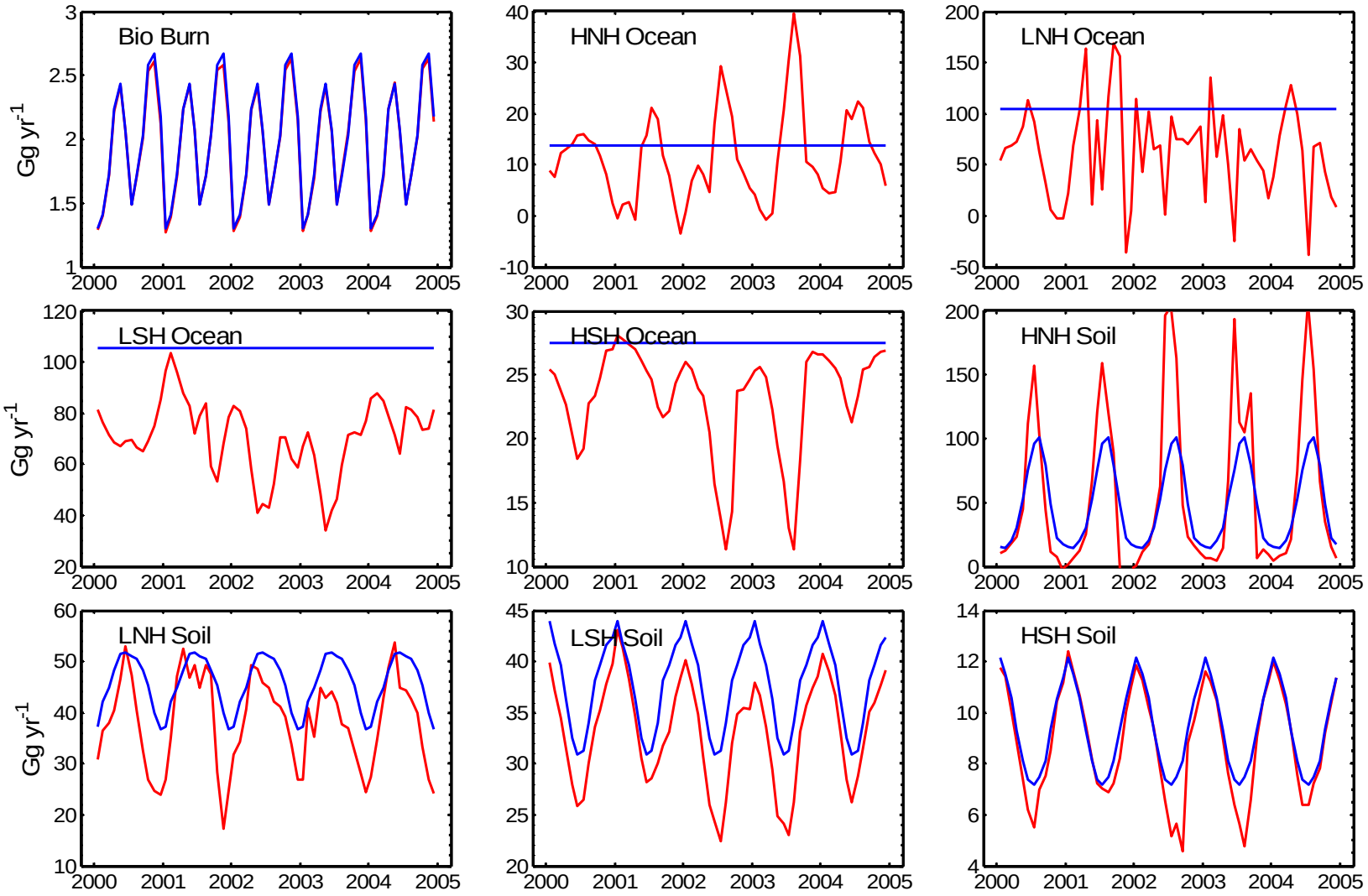

Figure 6.3. Inversion results for the seasonal processes of chloroform. Blue lines show the reference magnitudes, which are annually repeating. Red lines show the optimized estimates, which contain interannual variability.

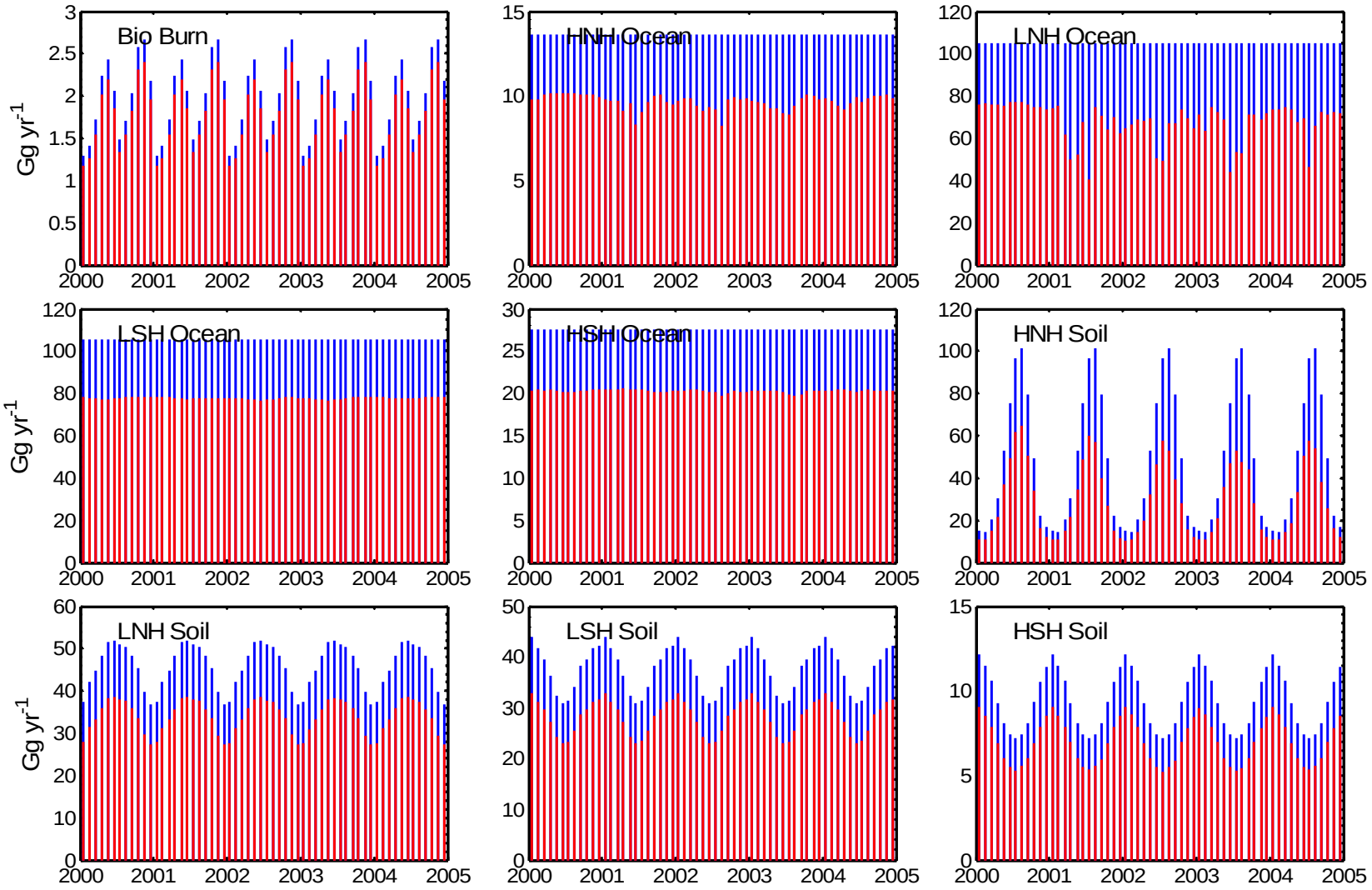

Figure 6.4. The corresponding uncertainties (1 σ error bars) of the inversion results in Figure 6.3, with the optimized error bars (red) superimposed upon the reference error bars (blue).

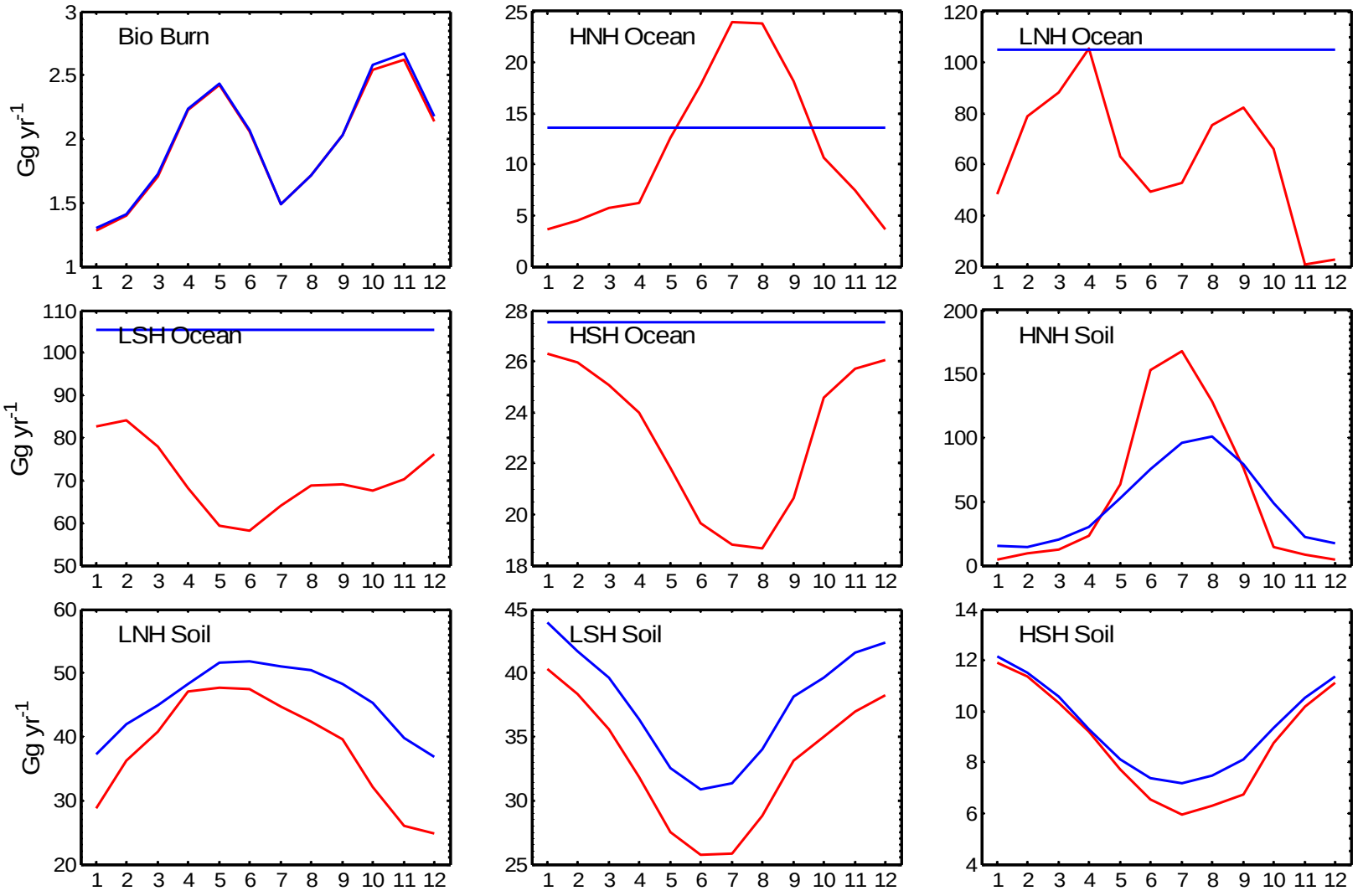

Figure 6.5. 5-year averaged seasonal emissions for chloroform. Blue lines show the reference magnitudes. Red lines show the optimized estimates.

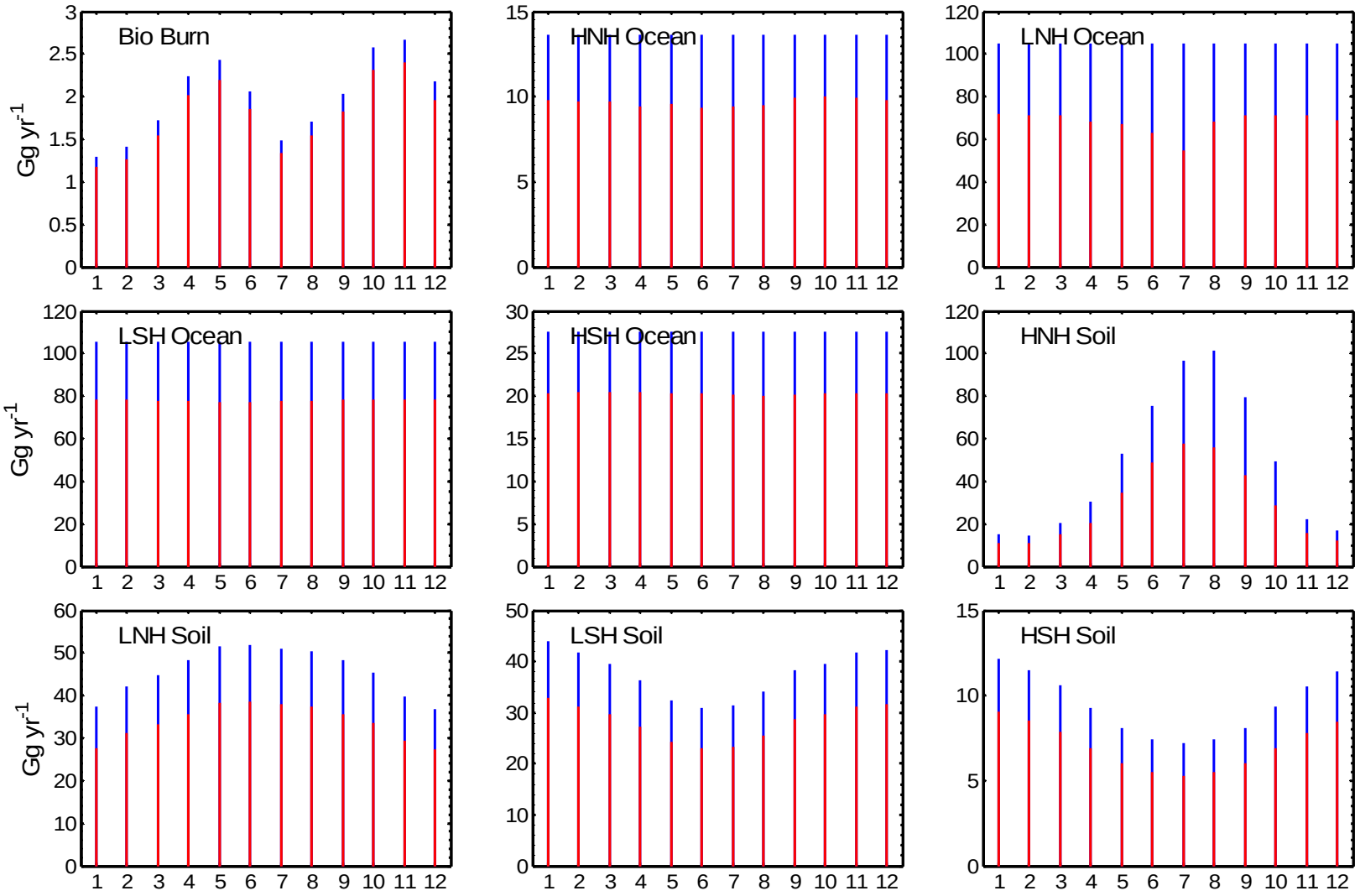

Figure 6.6. The corresponding uncertainties (1 σ error bars) of the inversion results in Figure 6.5, with the optimized error bars (red) superimposed upon the reference error bars (blue).

6.3.1. Average seasonal results

To show a single representative seasonal cycle of the natural processes, we take the arithmetic average of the five year results (e.g., the five Januarys are averaged to indicate a representative January). The corresponding associated uncertainties are estimated using:

$$\overline{\sigma}_t = \sqrt{\frac{\sum_{1}^{N} \sigma_{t,n}^2}{N}} \tag{6.3}$$

where t represents a particular month (e.g., January) and $n = 1$ to N = 5, for the five years of the inversion.

Figure 6.5 shows the averaged seasonal results (red lines) compared to the reference ones (blue lines), and Figure 6.6 shows their corresponding 1σ uncertainties with the optimal ones (red bars) superimposed on top of the reference uncertainties (blue bars). As noted earlier, there is no significant deviation from the reference case for the global biomass burning source.

The derived oceanic emissions show well-established seasonal variations in the HNH and HSH. Both regions show a summer maximum and a winter minimum in the oceanic emissions. Despite the importance of the oceanic flux of chloroform, not much information on the processes that are involved in chloroform formation is available. Presumably these processes are biological. If we assume that the NOAA-GMD proxy relationship between CH_3Cl saturation anomaly and sea surface temperature (SST)

[*Khalil et al*., 1999] is also applicable to chloroform, higher sea surface temperature in the summer should imply higher saturation and transfer velocities across the air-sea interface, and the opposite for the lower SST in the winter [*Khalil et al*., 1999]. There is a less clear seasonality of the tropical oceanic emissions, presumably resulting from the smaller summer-winter contrast in the sea surface temperature of the tropical oceans. There is however a tendency for highest emissions in February-April in both tropical semihemispheres.

Forest, grasslands, and peat moorland soils are a possible terrestrial sources of chloroform [*Laturnus et al*., 2002]. Measurements of the high ratios of the top soil air to ambient air $CHCl_3$ concentrations ($C_{soil}/C_{ambient}$) and the maximum $CHCl_3$ concentrations observed in the top organic rich soil layer [*Hoekstra et al*., 1998b; *Haselmann et al*., 2000a] indicated a biogenic formation of chloroform in the upper layers of the soil. This also leads to the question of whether seasonal variations exist. Our inversion shows distinct seasonal variations of the soil sources for chloroform in the four semihemispheres, generally with summer maximum and winter minimum. These results resemble the findings of the year-round study in a spruce forest conducted by *Haselmann et al*. [2002], which showed highest production in warm and humid periods and lower activity in dry and/or cold periods. The mechanism for chloroform release from soils has been demonstrated to be chlorination of soil acids, mainly humic materials, by hypochlorous acid (HOCl). This is generated from the chloride ion that is ubiquitous in soil, and hydrogen peroxide (H_2O_2), in the presence of chloroperoxidase (CPO) enzyme. Chloroperoxidase activity has been observed in many soil extracts [*Asplund et al*., 1993;

Laturnus et al., 1995] and has been shown in the laboratory to catalyze the chlorination by hydrogen peroxide (H_2O_2) and chloride ion of simple organic compounds to produce chloroform [*Walter and Ballschmiter*, 1992]. The source of chloroperoxidase enzyme is likely to be fungal [*Hoekstra et al*., 1998b; *Hjelm*, 1996]. Rice paddy soils and termite bearing soils have also been identified as $CHCl_3$ sources [*Khalil et al*., 1990, 1998]. The chloroform release from termite mounds also showed a seasonal dependence with significantly lower emissions during the winter [*Khalil et al*., 1990]. No attempt has been made in this work to determine the detailed seasonal behavior of different types of terrestrial soil sources of chloroform. The inversions give a general idea of the annual cycles of the aggregated terrestrial sources on a semihemispheric scale, for the limited measurements taken from a small number of observation sites and from the very few $CHCl_3$ in situ flux experiments carried out to date.

6.3.2. Average annual results

The inversion results enable quantification of the global average annual budget of chloroform ($CHCl_3$). Figure 6.7 and Table 6.3 contain the $CHCl_3$ fluxes averaged over the entire period between 2000-2004. We have further aggregated individual regions into global oceanic and soil emissions (Table 6.4); their individual fluxes are listed in Table 6.3. The averages for the seasonal processes have been derived by averaging the results shown in Figure 6.3. Figure 6.7 and Table 6.3 also include the optimized errors for which Equation (6.3) has been extended to all months to determine the annual average errors. The optimization errors are always less than the reference errors due to the reductions in

the Kalman filter driven by the observations. The seasonal processes, which have been solved as monthly fluxes, have greater uncertainty in their five-year averages.

As noted before there is no significant update for the global biomass burning source. Our inversion results show greater reductions for the tropical oceanic emissions relative to the a priori ones than they show for the extratropical regions. The inversion still indicates the greater importance of the tropical relative to higher latitude oceanic emissions, probably related to the higher sea surface temperature in the tropical regions. The oceanic fluxes are expected to decrease poleward along with the SSTs, and we suspect that the polar oceans are actually a sink of chloroform, thus also contributing to smaller net oceanic fluxes in the extratropical regions. The global annual oceanic emission totals 168 ± 106 Gg yr^{-1}, and the percentages in the 4 regions are 7%, 37%, 42%, and 14% respectively, from north to south. The bias of the oceanic emissions toward the Southern Hemisphere probably results simply from the larger oceanic area in the Southern Hemisphere. The deduced soil sources in the four regions deviate slightly from their a priori values, and the (north to south) percentages are 41%, 28%, 24%, and 7%, respectively, again approximately proportional to the terrestrial (land) area in the four semihemispheres.

The estimated total oceanic emissions (45%) are still greater than the soil emissions (37%). The partitioning of the total sources into the Northern and Southern Hemispheres are 62% and 38% respectively, which is very close to the estimate of *O'Doherty et al*. [2001] who deduced 64 ± 5% of the emissions originating from the Northern Hemisphere.

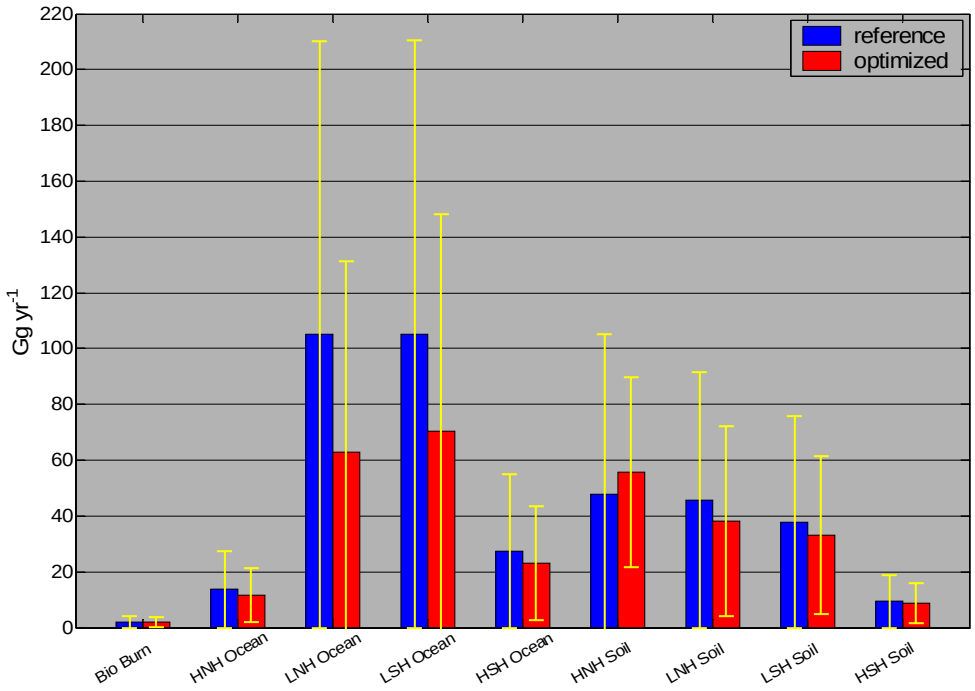

Figure 6.7. Annual average chloroform surface flux magnitudes. Shown are the reference (blue bars) and optimized (red bars) values with their 1 σ error bars (yellow). The errors on the references are derived from the assumed a priori inversion uncertainties.

6.4. Inversion check

To check the inversion we ran the forward model with the final optimal emission estimates, and compared the predicted mole fractions with the measurements. Figure 6.8 shows the residuals between the optimized and observed monthly mean mole fractions, compared to the residuals between the reference and observed monthly mean mole

fractions at each observing site. The optimized mole fractions tend to be much closer to the observations at most of the sites compared to the reference. Also note that the fit to measurements at WLEF tower and Harvard Forest stations received least improvement. This is because these two flask sites are located in an inland region which is subject to greater mismatch errors compared to other sites (due to their greater trace gas variability caused from local influences). Also data for these flask sites received larger errors (less weight) due to low sampling frequencies.

6.5. Summary and conclusions

We solved for seasonal, annual, and interannual surface fluxes of chloroform during 2000-2004 using the adapted Kalman filter as described in Chapter 4. The main conclusions are summarized below.

Biomass burning is still indicated as a minor source of chloroform. The oceanic emissions are greater than the soil emissions. Seasonal cycles have been derived for both the oceanic and terrestrial sources, with summer maxima and winter minima emissions, presumably because both processes are microbially activated and the microbial activities favor warmer environments.

The interannual variability of the derived oceanic and soil fluxes reflects the impact of the 2002/2003 globally wide-spread warming and droughts. The anomalously high emissions from the HNH oceans in the two summers of 2002 and 2003 are likely caused by high sea surface temperature anomalies, and the low emission anomalies from the

HNH and LNH soils in the summer of 2003 and from the LSH and HSH soils in the winters (SH) of 2002 and 2003 are likely caused by the extreme droughts in these two consecutive years.

Table 6.3. Five-year averaged optimal surface flux values and their 1 σ errors for seasonal processes/regions (units of Gg yr^{-1}).

Flux type		*Khalil et al*., 1999	Reference	Optimization
Biomass burning		-	1.98 ± 2.03	1.97 ± 1.83
Oceans	90ºN-30ºN	20.2	13.6 ± 13.6	11.5 ± 9.7
	30ºN-0º	150.4	105.1 ± 105.1	62.8 ± 68.4
	0º-30ºS	150.4	105.3 ± 105.3	70.5 ± 77.8
	30ºS-90ºS	40.4	27.5 ± 27.5	23.1 ± 20.3
	Subtotal	361.3	251.6 ± 151.9	167.9 ± 106.0
Soils	90ºN-30ºN	67.3	47.9 ± 57.3	55.6 ± 34.0
	30ºN-0º	67.3	45.6 ± 45.9	38.2 ± 34.1
	0º-30ºS	56.1	37.7 ± 37.9	33.1 ± 28.4
	30ºS-90ºS	11.2	9.4 ± 9.6	8.8 ± 7.1
	Subtotal	202.0	140.7 ± 83.2	135.7 ± 56.4

Table 6.4. Five-year averaged optimal surface flux values and their errors for seasonal processes (aggregated regions). All values are in Gg yr^{-1}.

Flux type	*Keene et al*., 1999	Reference	This work
Industry	65	64.5	64.5
Biomass burning	2	1.98 ± 2.03	1.97 ± 1.83
Oceans	361	252 ± 152	168 ± 106
Soils	202	141 ± 83	136 ± 56
Total	630	459 ± 173	370 ± 120

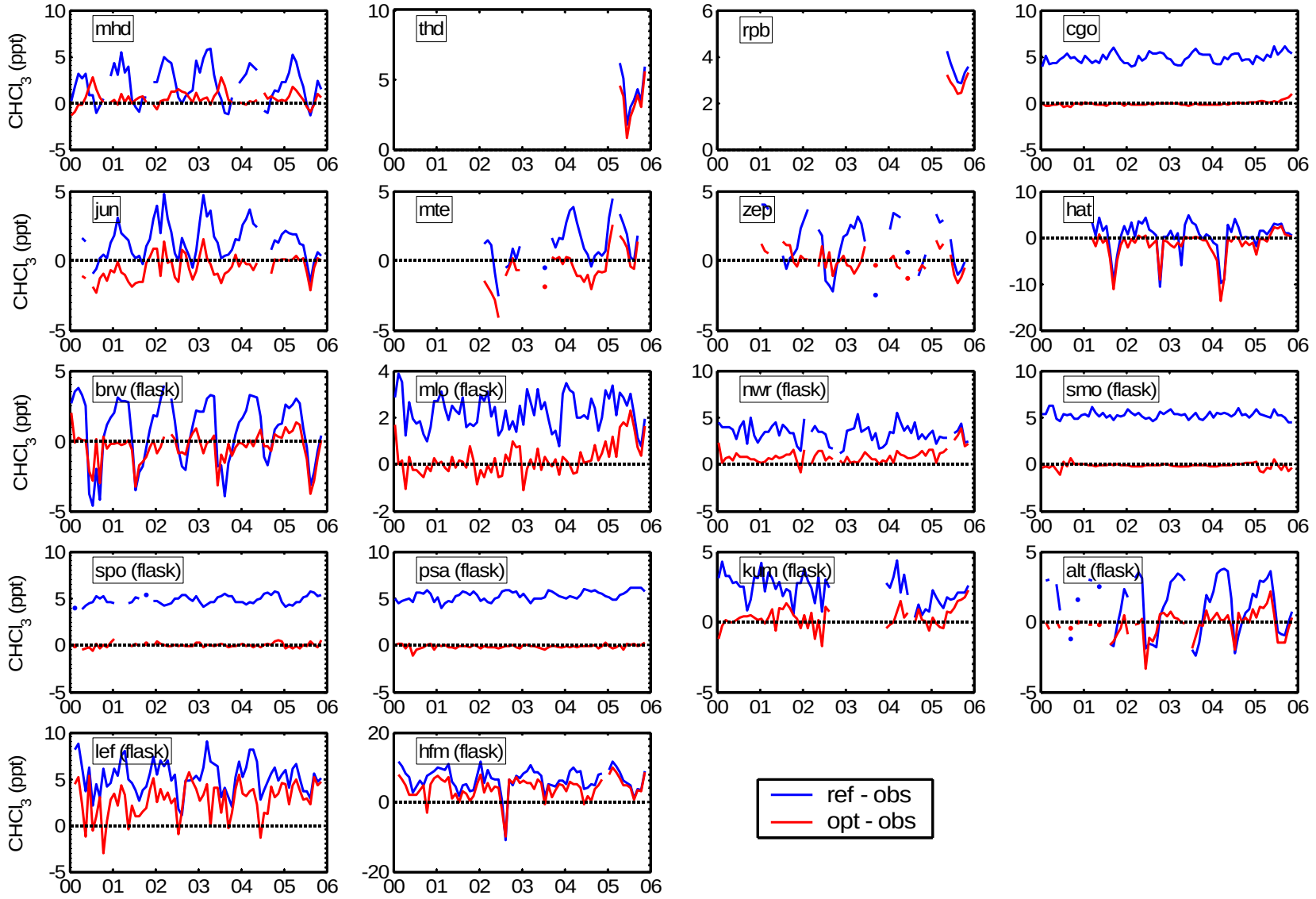

Figure 6.8. Residuals between the optimized and observed monthly mean mole fractions of chloroform (red lines), compared to the residuals between the reference and observed monthly mean mole fractions (blue lines) at each observing site.

Chapter 7

Inversion Results for Dichloromethane

The global average mole fraction of dichloromethane, or methylene chloride (CH_2Cl_2), was estimated at about 25 ppt. The corresponding tropospheric chlorine burden was approximately 0.25 Tg Cl (in CH_2Cl_2). Mixing ratios of CH_2Cl_2 in the Northern and Southern Hemispheres were about 40 and 17 ppt, respectively [*Khalil*, 1999; *Khalil et al*., 1999]. This large interhemispheric difference reflects the significant contribution of anthropogenic emissions to ambient concentrations in the Northern Hemisphere. In more recent studies, six years (1998-2004) of in situ observations of CH_2Cl_2 from the AGAGE station at Cape Grim, Tasmania show the average background level there was 8.74 ± 0.03 ppt, with a small but significant growth of 0.05 ± 0.01 ppt yr^{-1}, while the AGAGE station at Mace Head, Ireland shows an average mole fraction of 30.8 ± 0.2 ppt with a downward trend of 0.3 ± 0.1 ppt yr^{-1} [*Simmonds et al*., 2006]. All CH_2Cl_2 observations show strong annual cycles as expected from the fact that reaction with the OH radical is the primary CH_2Cl_2 sink.

CH_2Cl_2 is a mainly anthropogenic trace gas and more than 70% of its emissions originate from industrial sources [*Keene et al*., 1999]. CH_2Cl_2 is a highly volatile solvent which finds application in a wide variety of industrial and commercial processes. It is used in paint removers, degreasing and cleaning fluids, and even as an extraction solvent in the decaffeination of coffee. However, concerns about its health effects have led to a search for alternatives to it in many of these applications. Global industrial emissions from audited sales data were estimated at about 580 Gg yr^{-1} in 1990, and have declined steadily since then at a rate of about 12 Gg yr^{-2} [*McCulloch et al*., 1999, updated]. Natural sources are not well characterized. Oceans and biomass burning have been identified and estimated to contribute about 25% and 5% respectively to global emissions [*Keene et al*., 1999]. The best estimated magnitude of the composite identified CH_2Cl_2 sources is 38% greater than the better quantified known OH sink [*Cox et al*., 2003], suggesting that the current strengths of one or more of the CH_2Cl_2 sources are overestimated.

As noted earlier, CH_2Cl_2 is removed from the atmosphere primarily by reaction with OH yielding atmospheric partial OH-removal lifetime of about 150 days. Compared to longer-lived chlorocarbons, this significantly lowers its chances of reaching the stratosphere where it would be damaging ozone. Because of its low impact on stratospheric ozone it is not regulated by the Montreal Protocol. However, it is classified as a hazardous air pollutant and toxic volatile organic compound in regional air quality inventories [*Simmonds et al*., 2006]. Because of its short lifetime, CH_2Cl_2 concentrations are largely influenced by local/regional emissions. *Simmonds et al*. [2006] used the observations at Mace Head to deduce the European emissions of CH_2Cl_2 and found that

they were much lower than the industry estimates based on industry sales data [*McCulloch et al*., 1999, updated]. The differences could be attributed to errors in either or both estimating procedures, and more work is needed to resolve these issues.

In this chapter we present and discuss the inversion results for the CH_2Cl_2 industrial emissions and the seasonally varying CH_2Cl_2 emissions from the oceanic and biomass burning sources, using a similar approach to that used in Chapters 5 and 6.

7.1. Definition of the state vector and its a priori flux maps

The sources of dichloromethane are both anthropogenic and natural. The Reactive Chlorine Emissions Inventory (RCEI) under the auspices of the International Global Atmospheric Chemistry Program's Global Emissions Inventory Activity (GEIA) [*Graedel and Keene*, 1999] provides high resolution (1º × 1º latitude, longitude) annual emission fields for the biomass burning and anthropogenic industrial sources for the reference year of 1990. We have converted these maps to MATCH T42 grids (Figure 7.1) and imposed seasonality on the biomass burning source by assuming proportionality to the seasonality of methyl chloride (CH_3Cl) biomass fuel emissions [*Lee-Taylor et al*., 2001]. This is a reasonable assumption because both CH_2Cl_2 and CH_3Cl emissions are correlated with CO and CO_2 emissions [*Lobert et al*., 1999] and are therefore also correlated with each other. Since the interannual variations of the mole fractions in the NH and SH were only about ± 1% and ± 0.6% per year respectively [*Simmonds et al*., 2006], the industrial sources presumably remained at fairly stable levels for the five-year period (2000-2004) investigated here. Therefore in this work we estimate five-year

average magnitudes for the industrial sources, so that the corresponding state vector elements in the Kalman filter are time-invariant constant variables. We have further divided the global industrial source into eight regions: Europe (IND Europe), Northwest Asia (IND NW Asia), South Asia (IND So Asia), Southeast Asia (IND SE Asia), Africa (IND Africa), Australia (IND Australia), North America (IND N. Amer), and South America (IND S. Amer), as shown in Figure 7.2.

Although evidence has been presented that the oceans are another natural source of dichloromethane, the nature and their roles in the global budget of CH_2Cl_2 are poorly known [*Moore*, 2004]. There are very few flux measurements for the natural oceanic source of dichloromethane, and the magnitude of the flux is therefore extremely uncertain at present [*Khalil et al*., 1999; *Moore*, 2004]. For the forward modeling we used two kinds of oceanic emission distribution fields as described below. For the first one, *Khalil et al*. [1999] provide semihemispheric oceanic emission rates of CH_2Cl_2, which have been distributed evenly to the MATCH T42 grids within each region. We call this the "uniform" oceanic emissions case. For the second distribution field, we note that there is evidence showing that the net CH_2Cl_2 source in the lower latitudes and the net uptake of CH_2Cl_2 in the higher latitudes [*Moore*, 2004], are similar to those for methyl chloride (CH_3Cl). Therefore, we use the CH_3Cl monthly emission fields as our proxy for the regional distribution and seasonal variability of the oceanic emissions of CH_2Cl_2, and call this the "non-uniform" oceanic emissions case. The global magnitudes of both kinds of oceanic emission fields are set to be equal to the estimate of *Khalil et al*., 1999 scaled by a single factor (as described below). We then compared the two forward runs (with the

two different cases of oceanic emissions) with the observations, and chose the non-uniform case, which was closer to the observations, as our reference.

The dominant removal process for CH_2Cl_2 in the troposphere is reaction with the hydroxyl (OH) radical, accounting for more than 98% of its total destruction rate [*Keene et al*., 1999]. This process is simulated by the 3-D OH fields in the MATCH model. The OH fields also account for most of the CH_2Cl_2 destruction in the stratosphere. Since, like $CHCl_3$, the best estimated magnitude of the composite identified CH_2Cl_2 sources is much greater than the better quantified known OH sink [*Cox et al*., 2003], we further adjust the global industrial and oceanic emissions (the two dominant sources) by a single factor (~ 70%) [*Cox et al*., 2003] to roughly balance the calculated losses before optimization and take them as our reference values.

Given the spatial resolution of the available best estimates and the available observations, we estimate the biomass burning and oceanic emissions on a semihemispheric scale at a monthly resolution. Within each semihemispheric region, the spatial distributions of the source types remain as their reference values. The state vector at time k is expressed as:

$$\mathbf{x}_k = \begin{bmatrix} \mathbf{X}_k^c \\ \mathbf{X}_k^s \\ \mathbf{X}_{k-1}^s \\ \cdots \\ \mathbf{X}_{k-T}^s \end{bmatrix} \tag{7.1}$$

where

$$\mathbf{X}_k^c = \begin{bmatrix} x_k^{\text{IND Europe}} \\ x_k^{\text{IND NW Asia}} \\ x_k^{\text{IND So Asia}} \\ x_k^{\text{IND SE Asia}} \\ x_k^{\text{IND Africa}} \\ x_k^{\text{IND Australia}} \\ x_k^{\text{IND N. Amer}} \\ x_k^{\text{IND S. Amer}} \end{bmatrix} \quad \text{and} \quad \mathbf{X}_k^s = \begin{bmatrix} x_k^{\text{HNH BB}} \\ x_k^{\text{LNH BB}} \\ x_k^{\text{LSH BB}} \\ x_k^{\text{HSH BB}} \\ x_k^{\text{HNH Ocean}} \\ x_k^{\text{LNH Ocean}} \\ x_k^{\text{LSH Ocean}} \\ x_k^{\text{HSH Ocean}} \end{bmatrix} \tag{7.2}$$

with the observations and the inversions covering the period from 2000 to 2004 (60 months total). The terms "HNH" and "LNH" denote higher (30º - 90º) and lower (0º - 30º) latitude Northern Hemisphere, and "HSH" and "LSH" denote higher (30º - 90º) and lower (0º - 30º) latitude Southern Hemisphere. The global magnitudes of the reference emissions and their roles in the state vector are listed in Table 7.1. The a priori errors for the industrial elements are ± 100% of their reference values except Southeast Asia which has ± 200% initial uncertainty. For the seasonal elements the a priori errors are ubiquitously ± 50% of their reference values, which encompass the uncertainty ranges in most of the literature. The surface sites whose observations are used in the inversions for CH_2Cl_2 are summarized in Table 7.2.

Table 7.1. Reference annual average strengths of the sources of atmospheric dichloromethane (CH_2Cl_2) and their participation in the inversion.

Source/Sink Type [reference]	Seasonality (Y/N ?)	Strength (Gg yr^{-1})	State Vector ?
Industry [*McCulloch et al*., 1999, adjusted]	N	408	Y (8 regions)
Biomass burning [*Lobert et al*., 1999]	Y	59	Y (4 regions)
Oceans [*Khalil et al*., 1999, adjusted]	Y	138	Y (4 regions)
Composite	Y	604	-

Table 7.2. List of the stations whose measurements are used in the inversions for CH_2Cl_2, along with their corresponding numbers as in Table 2.1.

(1) MHD	(2) THD	(3) RPB	(5) CGO	(6) JUN
(7) MTE	(8) ZEP	(9) HAT	(16) BRW	(20) MLO
(19) NWR	(22) SMO	(24) SPO	(23) PSA	(21) KUM
(15) ALT	(17) LEF	(18) HFM		

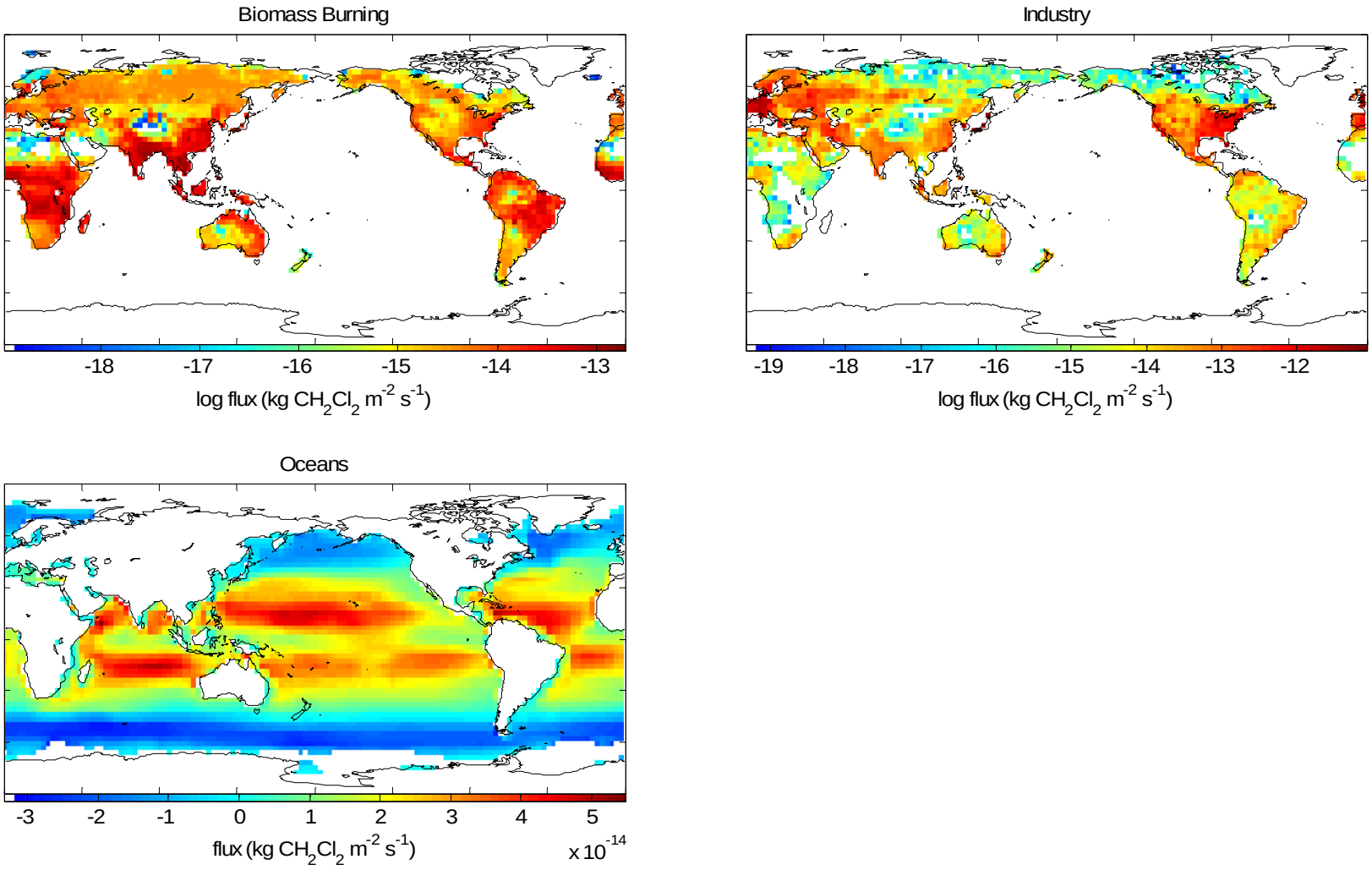

Figure 7.1. Annual average distributions of the reference dichloromethane emissions. Natural emission magnitudes and patterns vary by month. Global industrial emissions have been divided into eight regions as shown in Figure 7.2, and global biomass burning and oceanic emissions have been further divided into semihemispheric regions in the inversion (see text).

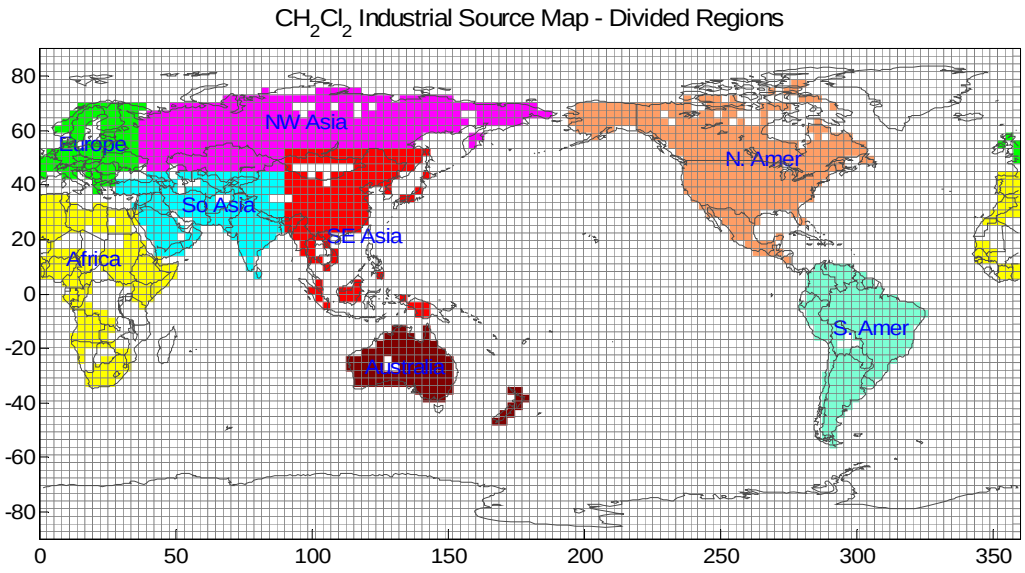

Figure 7.2. We show the partitioning of the global industrial source into the eight chosen regions. Also shown are the MATCH T42 grids. The regional magnitudes are estimated in the Kalman filter as five-year average values, and the spatial distribution within each region remains at its a priori distribution.

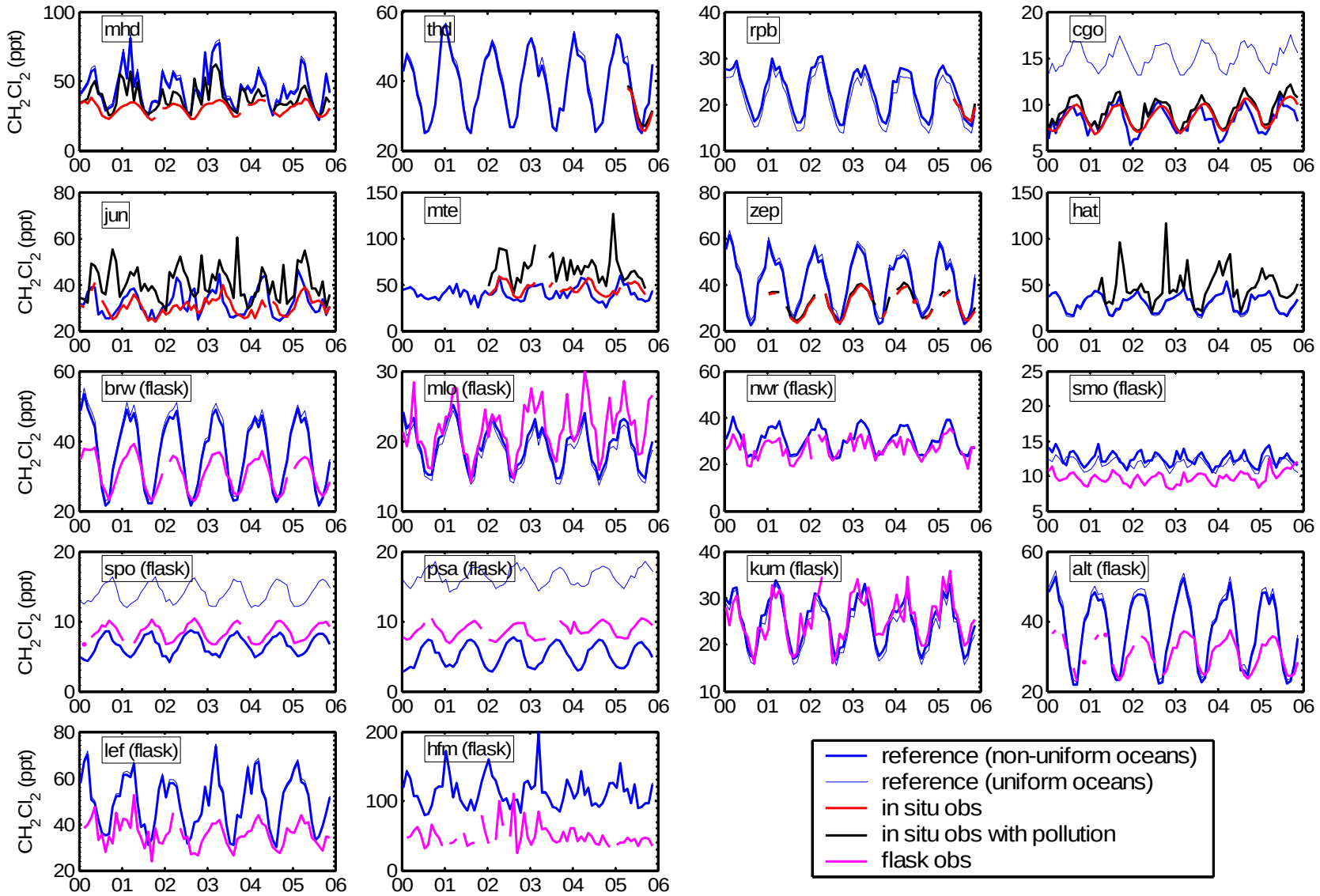

Figure 7.3. Time series of monthly mean dichloromethane mole fractions from the reference model run using the a priori surface fluxes are compared to the observations (with and without pollution for the high frequency in situ observations).

7.2. Forward modeling

To assess the ability of the a priori emission fields to reproduce dichloromethane observations, we used the annually repeating reference sources in forward runs of MATCH. We initialized the atmospheric 3-D distribution of CH_2Cl_2 using the output from a previous multi-year run, scaled to fit the observed mole fractions at remote sites such as Alert, Mauna Loa, and Cape Grim during January, 2000. These stations were chosen because they represent well the global background interhemispheric gradient due to their distance from strongly emitting sources. The reference run was then made from January, 2000 to November, 2005. The "perturbation" runs needed to compute sensitivities of model mole fractions to the eight regional industrial sources were also made simultaneously using the method described in Chapter 4. Figure 7.3 shows the monthly mean modeled versus observed mole fractions of CH_2Cl_2 at the indicated stations over the 6-year period of the simulation. As noted before, we have carried out two forward runs, one with uniform oceanic emissions (thinner blue lines), and the other with the oceanic emissions proportional to the methyl chloride oceanic emissions (thicker blue lines). The largest differences between the two runs occur at Cape Grim, South Pole, and Palmer stations, with the non-uniform oceans case showing a closer fit to the observations. This indicates that the non-uniform oceans case possesses more realistic oceanic surface flux rates and this case is therefore used as our reference.

7.3. Inversion results

7.3.1. Industrial emissions

For the presumed constant industrial sources, convergence towards a solution occurs over all time steps, as shown in Figure 7.4. It turns out that there is not enough data to separately resolve the European region and the Northwest Asia region, so we have aggregated these two regions into one element in the state vector, with the relative ratio of their emissions being kept at the reference value. Note that for the regions such as Europe and Northwest Asia, Southeast Asia, and North America with larger a priori emission magnitudes, the initial errors (blue bars) are very high (± 100% to ± 200%), and decrease more rapidly. The optimized value is the final value in each plot, corresponding to the use of the final observations in November, 2005. Because the aseasonal emissions are only fully optimized at the final step of the time series, earlier seasonal emissions (whose estimates also depend on the aseasonal values) at the beginning of the filter will not be fully optimized. In order to fully optimize all seasonal monthly values, we run the Kalman filter a second time fixing the aseasonal values to their optimized values from the first run of the Kalman filter.

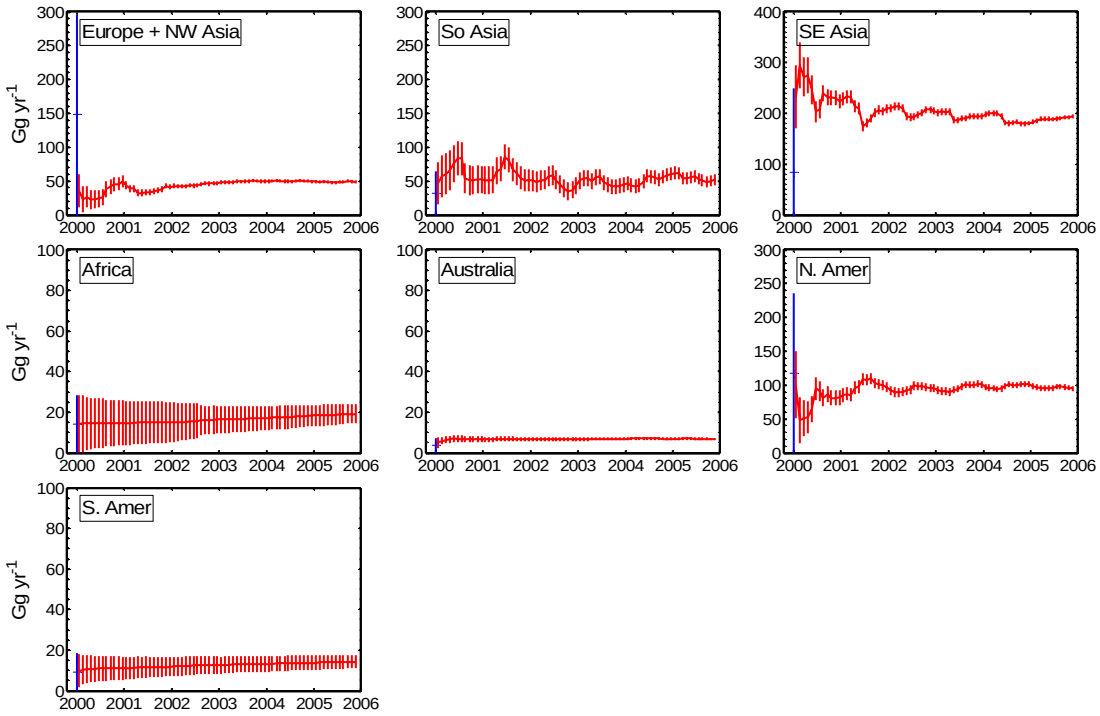

Figure 7.4. Convergence of the estimates of the magnitudes (and their 1 σ errors) for the regional industrial sources in the Kalman filter. Unlike the seasonal inversions, which solve for monthly fluxes, a single optimized flux estimate is made for each aseasonal source over the entire 6-year time period. The optimized value is the last value, after all observations have been used.

Figure 7.5 shows the comparison of the a posteriori optimal estimates and the a priori reference estimates and their relative regional importance to the global total industrial emission. The global optimal estimate of the industrial source is 430 ± 12 Gg yr^{-1}. Our derived European emissions of 42 ± 2 Gg yr^{-1} are much lower than the estimate of 130 Gg yr^{-1} from industry sales data [*McCulloch et al.*, 1999], and marginally lower than the

estimates of *Simmonds et al*. [2006] using model inversions (55 Gg yr^{-1}) and the CO ratio method (50 Gg yr^{-1}) using CO inventory [*Reimann et al*., 2005]. Our derived Southeast Asian emission of 195 ± 4 Gg yr^{-1} is nearly double its reference value, and the North American emission of 95 ± 4 Gg yr^{-1} is slightly less than its reference. Emissions from other regions are all small but also show differences from their reference values.

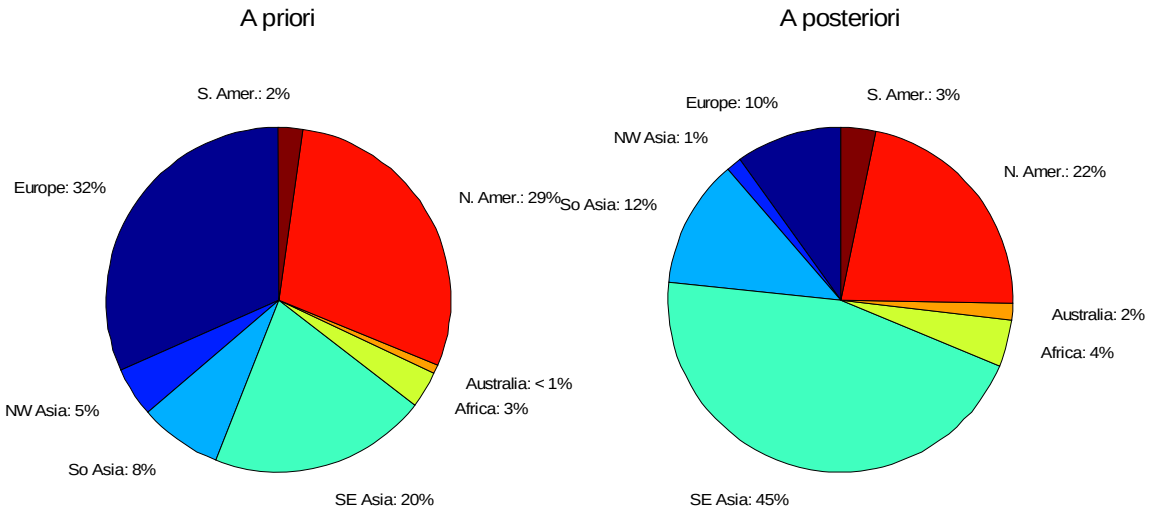

Figure 7.5. A priori (left chart) and a posteriori (right chart) regional contributions to the global industrial emission of dichloromethane.

7.3.2. Natural emissions

Figure 7.6 shows the optimized monthly fluxes (red lines) from January, 2000 to December, 2004, compared to the annually repeating reference values (blue lines). There are significant deviations from the reference cases for both the biomass burning and

oceanic sources. Overall there are larger seasonal variations than the references for almost all of the processes/regions.

The optimized values also capture the full interannual variability in the fluxes. There were relatively higher emissions from biomass burning in the LNH and LSH in the two-year frame 2002/2003. Like the CH_3Cl emissions, these anomalies could be attributed to the extreme 2002/2003 globally wide-spread heat and drought conditions (which were partly caused by the 2002/2003 El Niño event that lasted from September 2002 to August 2003 [*Knorr et al*., 2007]). Recent studies show a consistent link between El Niño and drought in the tropics [*Lyon*, 2004] and mid latitudes [*Zeng et al*., 2005b]. While the El Niño event during this time was moderate compared to the extreme 1997/1998 El Niño, the period 2002/2003 appears unusual with global land precipitation very low, leading to very dry and hot conditions [*Knorr et al*., 2007]. These dry and hot conditions might lead to increased insect damage to vegetation and increased susceptibility of the boreal biome to fire [*Kobak et al*., 1996; *Ayres and Lombardero*, 2000]. The enhanced fire events are expected to emit more CH_2Cl_2 than usual in agreement with our inversion.

As for the oceanic fluxes, the inversion retains the phasing of the seasonal variations (summer maxima and winter minima) of the reference HNH oceanic fluxes, but with larger and interannually varying amplitudes. The HSH oceans, which are shown in their reference as a net sink of CH_2Cl_2 during the year, are generally indicated by the inversion as a net source of CH_2Cl_2 during summer and a net sink during winter, but with other

complicated variations. There are larger seasonal and interannual variations in the tropical oceanic fluxes compared to their a priori values.

Figure 7.7 shows the decrease of uncertainties resulting from the inversions by superimposing the optimized uncertainties (red bars) on top of the reference uncertainties (blue bars). As noted for the other chloromethanes, the inversion acts to reduce the initial uncertainties by amounts depending on the value of the observations in constraining each emission process or region. Uncertainties for the oceans shrink the most; those for biomass burning sources have smaller reductions.

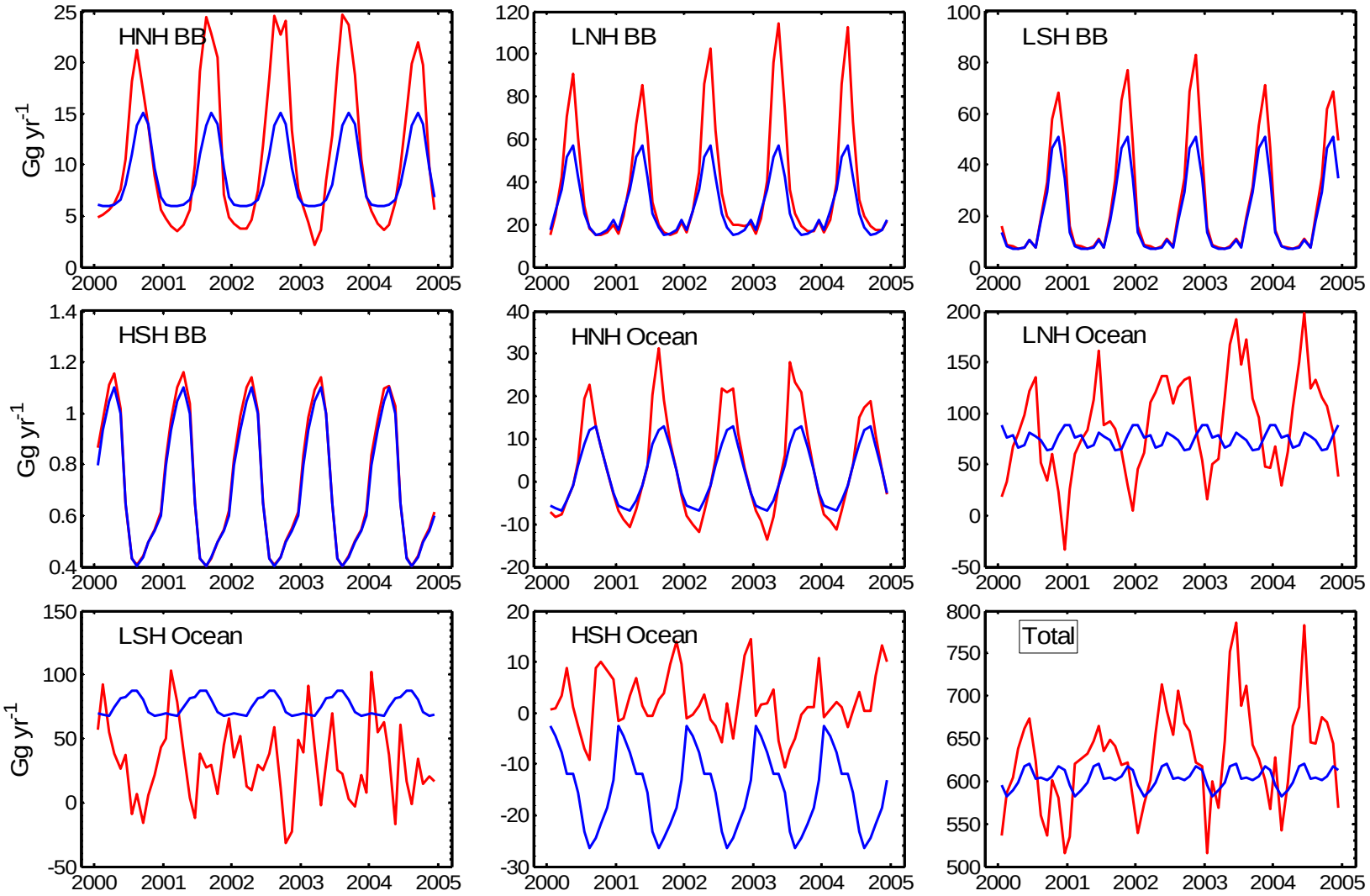

Figure 7.6. Inversion results for the seasonal processes of dichloromethane. Blue lines show the reference magnitudes, which are annually repeating. Red lines show the optimized estimates, which contain interannual variability. The total value is the sum of the eight seasonal processes plus the aseasonal industrial emission estimates (Figure 7.4).

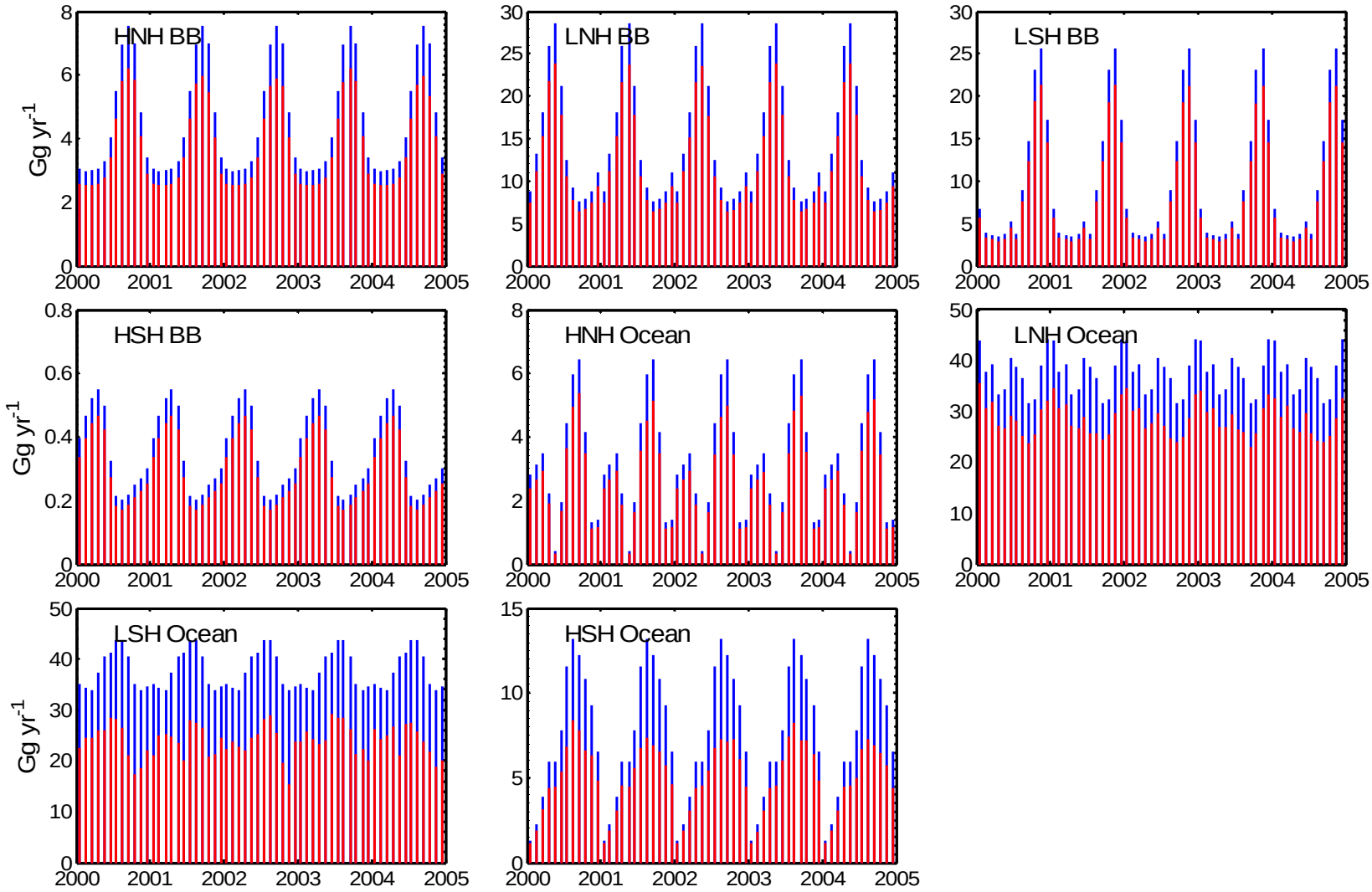

Figure 7.7. The corresponding uncertainties (1 σ error bars) of the inversion results in Figure 7.6, with the optimized error bars (red) superimposed upon the reference error bars (blue).

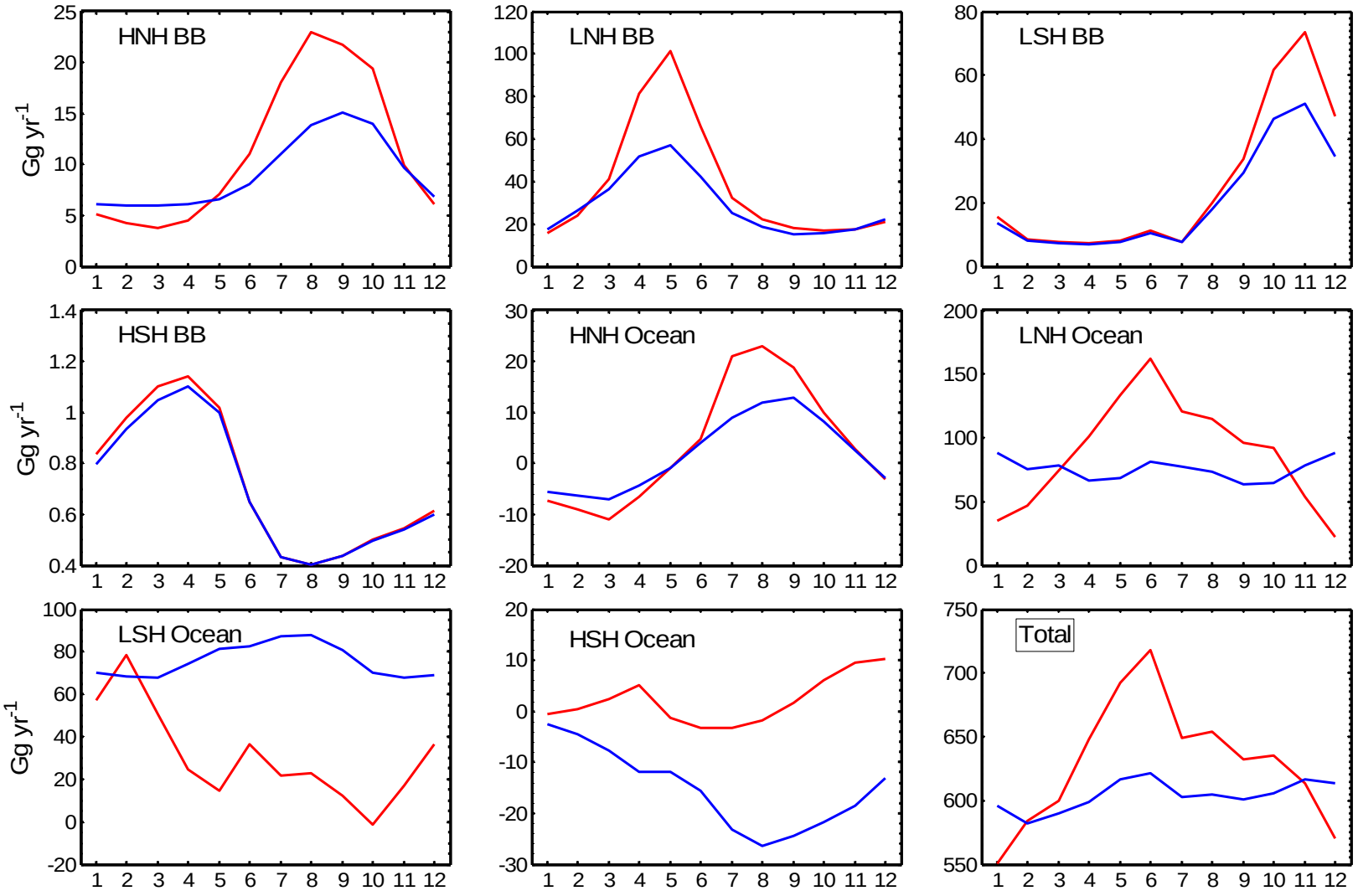

Figure 7.8. 5-year averaged seasonal results for dichloromethane emissions. Blue lines show the reference magnitudes. Red lines show the optimized estimates.

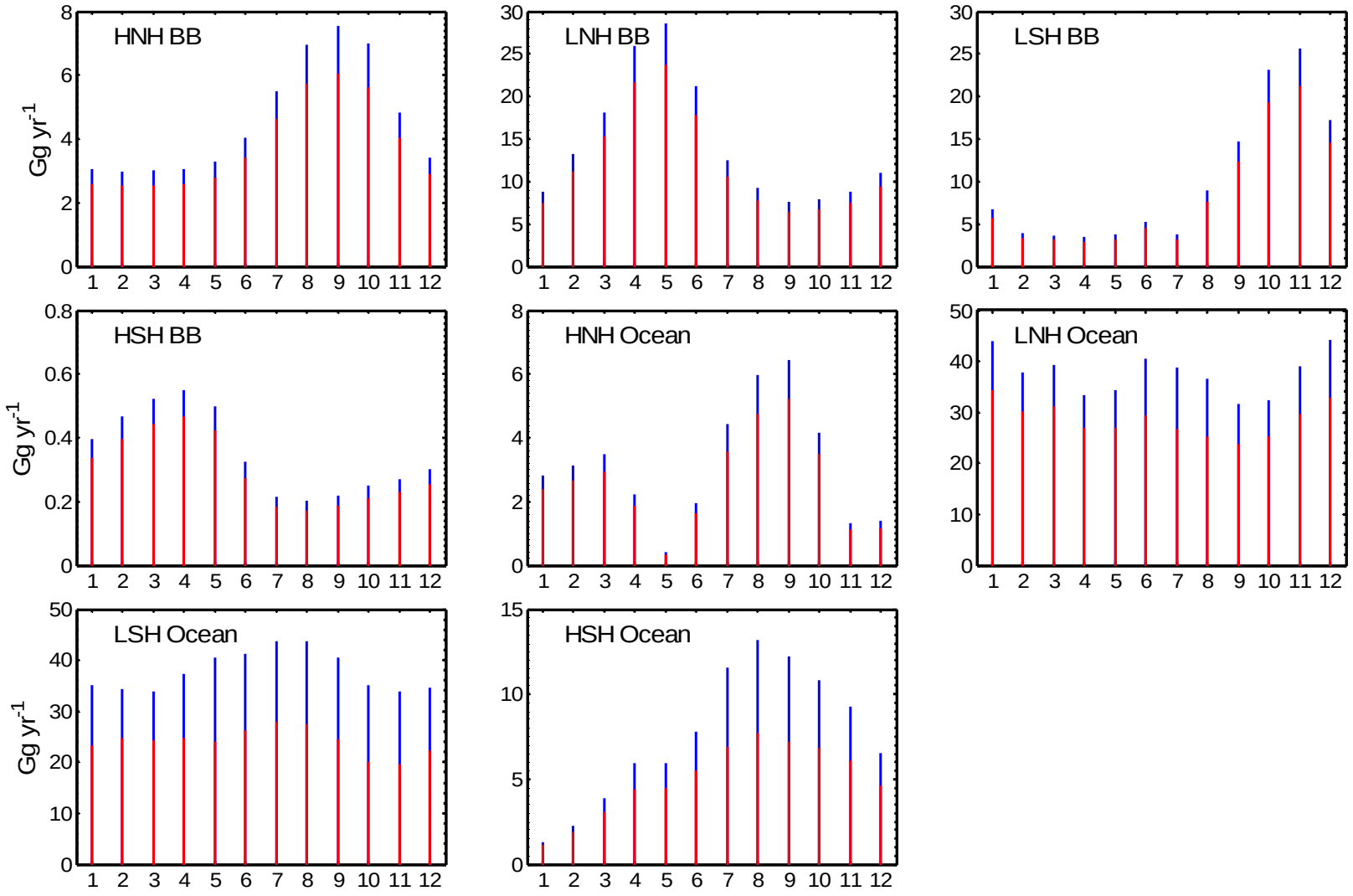

Figure 7.9. The corresponding uncertainties (1 σ error bars) of the inversion results in Figure 7.8, with the optimized error bars (red) superimposed upon the reference error bars (blue).

7.3.3. Average seasonal results

As before, we compute the average seasonal cycles for the seasonal emission processes, by taking the arithmetic average of the five year results. The corresponding associated uncertainties are estimated using:

$$\overline{\sigma}_t = \sqrt{\frac{\sum_{1}^{N} \sigma_{t,n}^2}{N}} \tag{7.3}$$

where t represents a particular month (e.g., January) and $n = 1$ to N = 5, for the five years of the inversion.

Figure 7.8 shows the averaged seasonal results (red lines) compared to the reference ones (blue lines), and Figure 7.9 shows their corresponding 1σ uncertainties with the optimal ones (red bars) superimposed on top of the reference ones (blue bars). Biomass burning emissions are concentrated in tropical regions, especially in India, Southeast Asia, Central Africa, and South America. To study the seasonal behavior of the biomass burning source, we show the seasonal cycles of the biomass burning sources in the four semihemispheres in Figure 7.10. Note that emissions from biomass burning in Central Africa, India, and Southeast Asia (LNH BB) peak in April and May (Northern Spring), and emissions from South America and South Africa (LSH BB) peak in October and November (Southern spring). Similar to CH_3Cl, the biomass burning emissions for both tropical regions are strongest during the spring dry season that has the largest amount of

biomass burned [*Hao and Liu*, 1994]. Our inversion generally retains the seasonal cycles of the reference emissions, but enhances the peaks for HNH BB, LNH BB, and LSH BB.

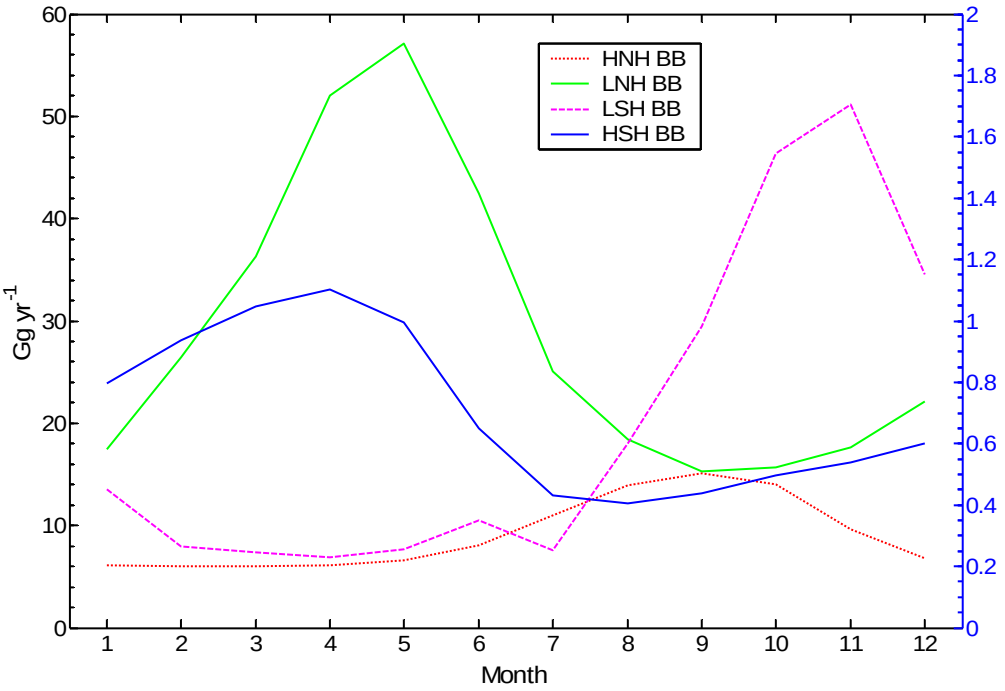

Figure 7.10. Seasonal cycles of the semihemispheric biomass burning sources of dichloromethane. Note the dominance of the tropical emissions. Biomass burning emissions from the HSH are very small and use the right-hand axis as their scale. Also the emission peaks for the tropical Northern and Southern Hemispheres occur in their respective (dry season) springs.

The derived oceanic emissions show well-established seasonal variations in the HNH, LNH and HSH (Figure 7.8). These three regions show summer maxima and winter minima in their oceanic emissions. Weakly soluble gases like CH_2Cl_2 may show

supersaturation in ocean surface waters in summer on account of warmer water temperatures and thus diminished solubility. Also, the tropical regions are expected to have larger emissions than higher latitude regions, consistent with their higher water temperatures. This effect is amplified for CH_2Cl_2 by the summertime decrease in its concentration in the atmosphere due to OH destruction. On the basis of measurements of oceanic supersaturation of CH_2Cl_2 from *Khalil and Rasmussen* [1998] and *Singh et al*. [1983], *Khalil et al*. [1999] estimated a CH_2Cl_2 flux of 160 Gg yr^{-1} from the ocean to the atmosphere. As noted before, it is significant that the previous budget of CH_2Cl_2 had an excess of sources over sinks (230 Gg yr^{-1}, [*Cox et al*., 2003]) that was even larger than the previous estimated ocean emission. Our inversion indicates a global oceanic emission total of only 124 ± 38 Gg yr^{-1}. Despite the importance of the oceanic flux of dichloromethane, not much information on the processes that are involved in dichloromethane production is available. Measurements of dichloromethane in the North Atlantic and Labrador Sea show that its distribution closely matches that of CFC 11 [*Moore*, 2004], which is known to have an entirely land-based source. Although CH_2Cl_2 has a short lifetime in the atmosphere, it appears to persist for years to decades in the intermediate and deep ocean. The work of *Moore* [2004] points strongly to a transfer of CH_2Cl_2 to the deep ocean during winter, followed by horizontal transport, upwelling to the ocean surface and re-emission to the atmosphere in the summer. Measurement of oceanic saturation levels throughout the year would be needed to establish whether the ocean is indeed a net source or is simply re-emitting in summer the CH_2Cl_2 that was taken up in the previous winter.

7.3.4. Average annual results

The inversion results have been aggregated to compute the global budget of dichloromethane. Figure 7.11 and Table 7.3 contain the CH_2Cl_2 regional fluxes averaged over the entire 5-year period between 2000-2004. We have further aggregated the semihemispheric seasonal processes into global biomass burning and global oceanic emissions as listed in Table 7.4; their individual fluxes are listed in Table 7.3. The average regional industrial sources are solved directly in the filter as single constant values. The averages for the seasonal processes are derived by averaging the results shown in Figure 7.6. Figure 7.11 and Table 7.3 also include the optimized errors. For the seasonal processes, Equation (7.3) has been applied to all months to determine their annual average errors. The errors for the optimized industrial sources are much less than the reference errors due to the reductions by all of the observations used in the Kalman filter. The seasonal processes, which are solved as monthly fluxes, have greater uncertainty in their five-year averages than the aseasonal processes, due to the fewer observations used to deduce them.

The global biomass burning emission magnitude is 75 ± 18 Gg yr^{-1}. Our inversion results show increases for the Northern tropical oceanic emissions and decreases for the Southern tropical oceanic emissions relative to the a priori ones. The inversion still indicates the greater importance of the tropical oceanic emissions, probably related to the higher sea surface temperatures and resultant supersaturations in the tropical regions. The oceanic fluxes are expected to decrease poleward, and we suspect that the polar oceans

are actually net sinks of dichloromethane, thus contributing to the smaller net oceanic fluxes in the extratropical regions. The global annual oceanic emission totals 124 ± 38 Gg yr^{-1}, and the percentages of the emissions in the 4 regions are 3%, 70%, 25%, and 2%, from north to south respectively.

The derived total global source for CH_2Cl_2 is 629 ± 44 Gg yr^{-1}. The relative importance of the industrial, oceanic and biomass burning sources are 68%, 20% and 12%, respectively.

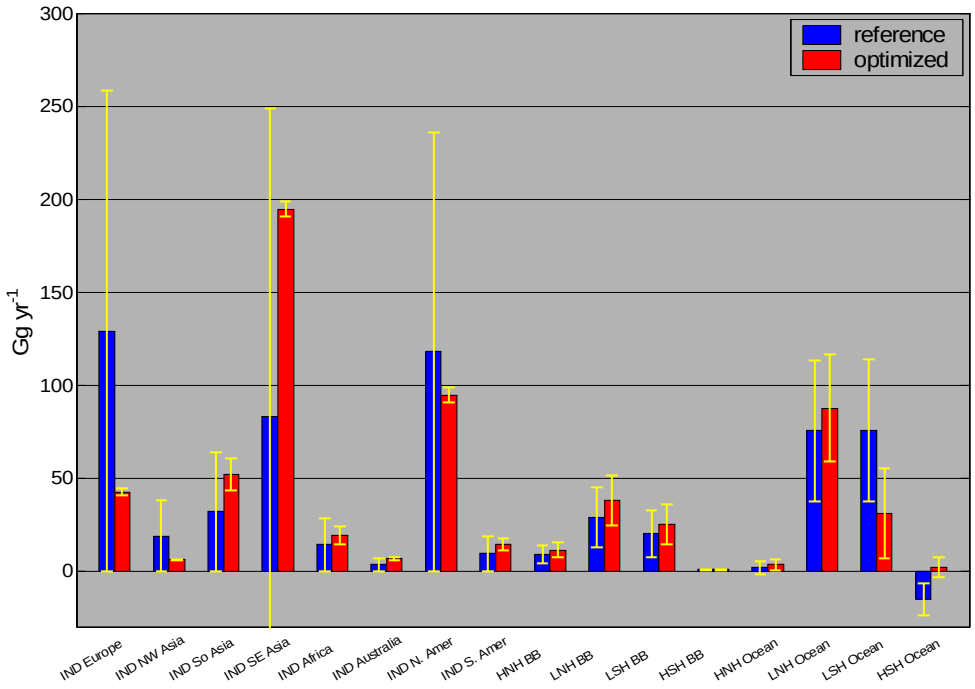

Figure 7.11. Annual multi-year average dichloromethane surface flux magnitudes. Shown are the reference (blue bars) and optimized (red bars) values with their 1 σ error bars (yellow). The errors on the references are derived from aggregating the assumed a priori inversion uncertainties.

Table 7.3. Five-year averaged optimal surface flux values and their errors for the industrial and natural processes/regions (units of Gg yr^{-1}).

Flux type		*Keene et al*., 1999	Reference	Optimization
Industry	Europe	184	129 ± 129	42 ± 2
	NW Asia	27	19 ± 19	6 ± 0.3
	So Asia	46	32 ± 32	52 ± 9
	SE Asia	118	83 ± 166	195 ± 4
	Africa	20	14 ± 14	19 ± 5
	Australia	5	3 ± 3	7 ± 1
	N. Amer	168	118 ± 118	95 ± 4
	S. Amer	13	9 ± 9	14 ± 3
	Subtotal	581	408 ± 244	430 ± 12
Biomass burning	90ºN-30ºN	9.1	9.1 ± 4.9	11.2 ± 4.0
	30ºN-0º	29	29 ± 16	38 ± 13
	0º-30ºS	20	20 ± 13	25 ± 11
	30ºS-90ºS	0.7	0.7 ± 0.4	0.7 ± 0.3
	Subtotal	59	59 ± 21	75 ± 18
Oceans	90ºN-30ºN	23	1.8 ± 3.6	3.5 ± 3.0
	30ºN-0º	51	75 ± 38	88 ± 29
	0º-30ºS	52	76 ± 38	31 ± 24
	30ºS-90ºS	70	-15 ± 8	2 ± 5
	Subtotal	196	138 ± 54	124 ± 38
Total		836	604 ± 251	629 ± 44

Table 7.4. Five-year averaged optimal surface flux values and their errors for the industrial and natural processes (aggregated regions). All values are in Gg yr^{-1}.

Flux type	*Keene et al*., 1999	Reference	This work
Industry	581	408 ± 244	430 ± 12
Biomass burning	59	59 ± 21	75 ± 18
Oceans	196	138 ± 54	124 ± 38
Total	836	604 ± 251	629 ± 44

7.4. Inversion check

Once again, we check the inversions by running the forward model with the final optimal estimates, and comparing the predicted mole fractions with the measurements. Figure 7.12 shows the residuals between the optimized and observed monthly mean mole fractions, compared to the residuals between the reference and observed monthly mean mole fractions at each observing site. The mole fractions computed using the optimal emissions tend to be much closer to the observations at most of the sites than the reference. Also note the fits to measurements at WLEF tower and Harvard Forest stations showed least improvement, because these two flask sites are located in inland regions, and are thus subject to greater mismatch errors compared to other sites due to their greater trace gas variability driven by nearby local sources.

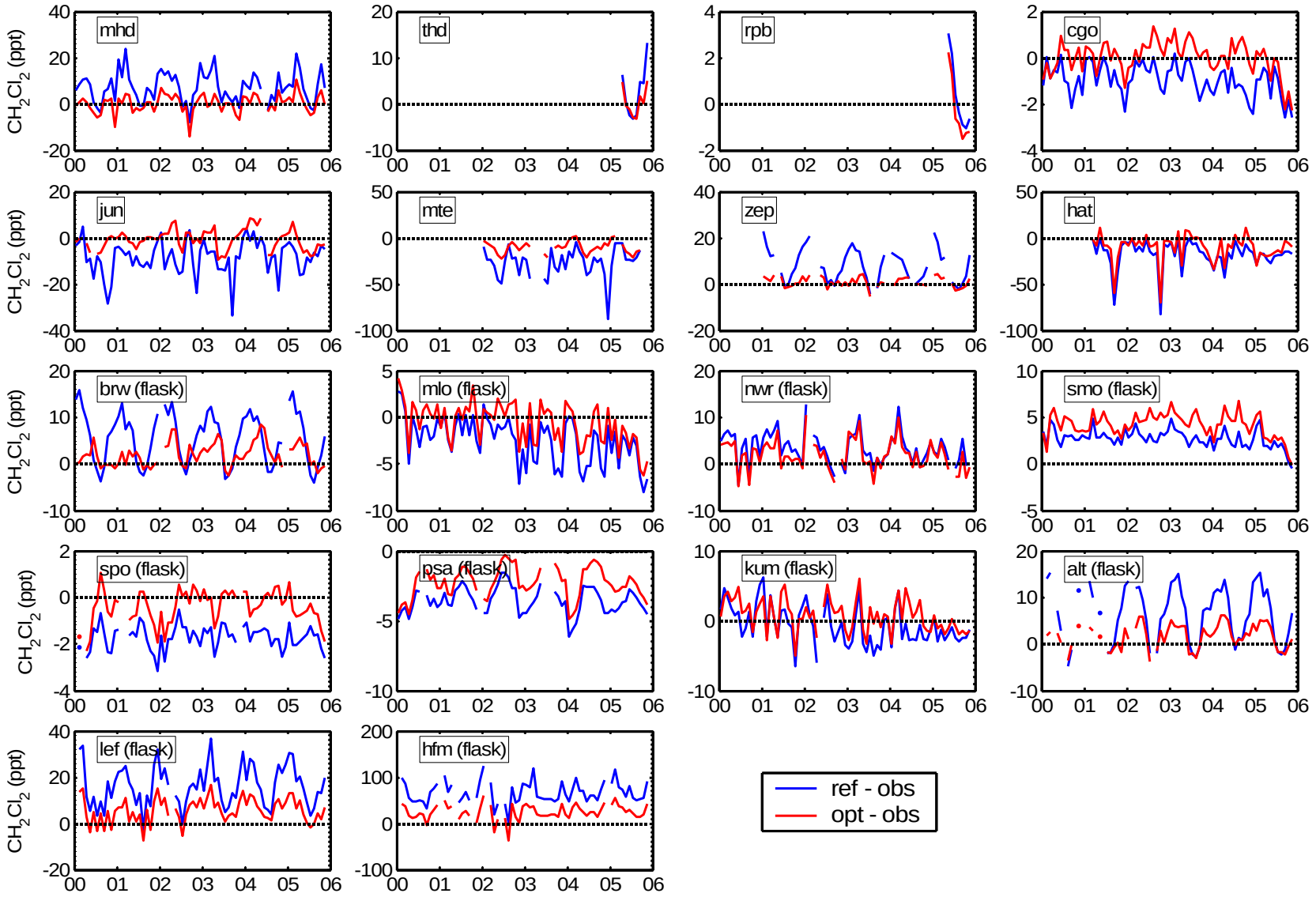

Figure 7.12. Residuals between the optimized and observed monthly mean mole fractions of dichloromethane (red lines), compared to the residuals between the reference and observed monthly mean mole fractions (blue lines) at each observing site.

7.5. Summary and conclusions

We solved for annual industrial, and seasonal and interannual biomass burning and oceanic monthly fluxes of dichloromethane during 2000-2004 using MATCH, observations, and the discrete Kalman filter as described in Chapter 4. The main conclusions are given here.

For the industrial emissions, our derived European emissions are much lower than the estimates from the industry sales data, but are only marginally lower than the estimates from the back-attribution technique and the CO ratio method using the CO emission inventories. Our inversion results show very significant emissions from the Southeast Asian region, while the North American emissions are slightly smaller than the a priori. Emissions from other regions are relatively small.

For the biomass burning source, emissions are concentrated in the tropical regions. Our inversion generally retains the phases of the seasonal cycles of the reference emissions, with emissions in Central Africa, India, and Southeast Asia (LNH BB) peaking in April and May (Northern spring), and emissions in South America and South Africa (LSH BB) peaking in October and November (Southern spring). For both tropical regions, the biomass burning emissions are strongest during the spring which is associated with warm and dry conditions leading to the largest amount of biomass burned. Relatively high emissions from biomass burning in the LNH and LSH in the two-year time frame of

2002/2003 might have been caused by the global wide-spread heat and drought conditions in that time period.

The derived oceanic emissions show well-established seasonal variations in the HNH, LNH and HSH with summer maxima and winter minima. The inversion, like the reference, indicates a greater importance of the tropical oceanic emissions relative to higher latitudes, probably related to the higher sea surface temperature and thus CH_2Cl_2 supersaturation in the tropical regions. The actual mechanisms of the processes that are involved in dichloromethane production warrant investigation, and measurement of oceanic saturation levels throughout the year would be needed to establish whether the ocean is indeed a net source or is simply re-emitting in summer the CH_2Cl_2 that was taken up in the winter.

Chapter 8

Inversion Results for Carbon Tetrachloride

Unlike the other three chloromethanes, carbon tetrachloride (CCl_4) is controlled by the Montreal Protocol and its various amendments due to its much longer lifetime (26 years) and much larger ozone depletion potential (0.73 relative to unit 1 of CFC-11) [*WMO 2002*]. CCl_4 is also a greenhouse gas with a global warming potential of 1380 per kg (compared to unit 1 per kg for CO_2) on a 100-year time frame [*WMO 2002*]. CCl_4 is thought to originate almost exclusively from anthropogenic emissions [*Simmonds et al*., 1998a], although analysis of polar firn air indicates there may be a small natural source [*Butler et al*., 1999]. Tropospheric concentrations of CCl_4 increased steadily from the mid-1970s, reaching a peak mixing ratio of ~ 105 ppt in 1990 and then began decreasing since then at a constant rate of 0.7 to 0.8 ppt yr^{-1} [*Simmonds et al*., 1998a; *Prinn et al*., 2000]. The current global average tropospheric concentration of CCl_4 is ~ 90 to 92 ppt. The interhemispheric difference has also been fairly constant at about 2% (NH > SH) since 1993 which indicates that significant emissions of carbon tetrachloride still remain today [*WMO 2002*].

The principle identified uses of carbon tetrachloride are as a general purpose solvent and also, since 1931, as a feedstock for the production of CFC-11 (CCl_3F) and CFC-12 (CCl_2F_2). Releases to the atmosphere from this CFC production arise only from fugitive losses [*WMO 2002*]. Historically it has been more difficult to estimate the industrial production of CCl_4 and its emissions to the atmosphere than for the CFCs. CCl_4 fugitive emission estimates have been derived indirectly from the more accurately known production records of CFC-11 and CFC-12. Large discrepancies existed in UNEP consumption data for past years owing to confusion over reporting procedures, and although these have been addressed, there may still be significant omissions and unrecorded sources. The principal sink for CCl_4 is stratospheric photodissociation, which is known to produce phosgene [*Kindler et al*., 1995]. Using an assumed partial atmospheric lifetime of ~ 42 years, combined with atmospheric measurements during the last several decades, *Simmonds et al*. [1998a] used a 2-D model inverse method and estimated that the global CCl_4 emissions averaged around 94 Gg yr^{-1} from 1979-1988 and 49 Gg yr^{-1} from 1991-1995. Based on stratospheric observations, and assuming that nearly all of the CCl_4 emitted eventually entered the stratosphere [*Volk et al*., 1997], it has been estimated that 35 years is a more accurate estimate of the CCl_4 atmospheric lifetime [*WMO 1998*]. Recently, the oceans have been quantified as a global sink of CCl_4 with a partial lifetime of 94 years [*Yvon-Lewis and Butler*, 2002]. The ocean sink, combined with a stratospheric partial lifetime of 35 years gives a total atmospheric lifetime of 26 years [*WMO 2002*]. These estimates of additional sinks (or lower total lifetime) suggest that the above global emissions of CCl_4 may be underestimated. More

recently soils have been proposed to be a global sink of CCl_4 which is even stronger than the oceanic sink [*Happell and Roche*, 2003]. This additional identified sink lowers the global lifetime of CCl_4 down to 20 years. However, the measured interhemispheric gradient of CCl_4 seems to be inconsistent with an overall lifetime of 20 years, and therefore the lifetime of 26 years given in *WMO 2002* is still recommended by *WMO 2006*.

8.1. Definition of the state vector and its a priori flux maps

As noted in the introduction, there have been estimates of CCl_4 industrial emissions from the industrial sales data and from the 2-D model inverse modeling approach. Figure 8.1 shows the yearly global industrial emission estimates from the industrial sale data [*McCulloch*] and recent updating of the estimates from the 2-D model inverse modeling approach [*Cunnold et al*., 1997; *Simmonds et al*., 1998a; updated by *D. Cunnold*]. Also shown are the corresponding linearly fitted lines. Note that there are two regimes in the 2-D model emission estimates, and the linearly fitted yearly global emissions for 1996-2004 are used as our references. For the a priori spatial distributions of CCl_4 industrial sources, global emissions were first subdivided regionally, followed by a country-by-country subdivision based on GDP. Population density was then used as a spatial proxy for emissions within countries. The 1996-2004 average global distribution of industrial emissions is shown in Figure 8.2 (left-hand graph). As can be seen, the a priori industrial emissions of CCl_4 are concentrated in Europe, North America, South Asia, and Southeast Asia. For the optimization, we have further divided the global industrial source into eight

regions: Europe (IND Europe), Northwest Asia (IND NW Asia), South Asia (IND So Asia), Southeast Asia (IND SE Asia), Africa (IND Africa), Australia (IND Australia), North America (IND N. Amer), and South America (IND S. Amer), as shown in Figure 8.3. CCl_4 production should be decreasing due to the Montreal Protocol and its amendments which is qualitatively consistent with the globally decreasing CCl_4 mole fractions after 1992. For this and other reasons, the regional emissions of CCl_4 are expected to vary both intra-annually and interannually. For the optimization, we therefore estimate the eight regional industrial sources at a 3-month time resolution for 1996-2004. We also estimate the global oceanic sink at a 3-month resolution. For convenience and consistency with the seasonal oceanic sink estimation in the Kalman filter, we set the 3-month time periods to be DJF, MAM, JJA, and SON (note that there is no assumption here that there are seasonal variations in the industrial emissions of carbon tetrachloride).

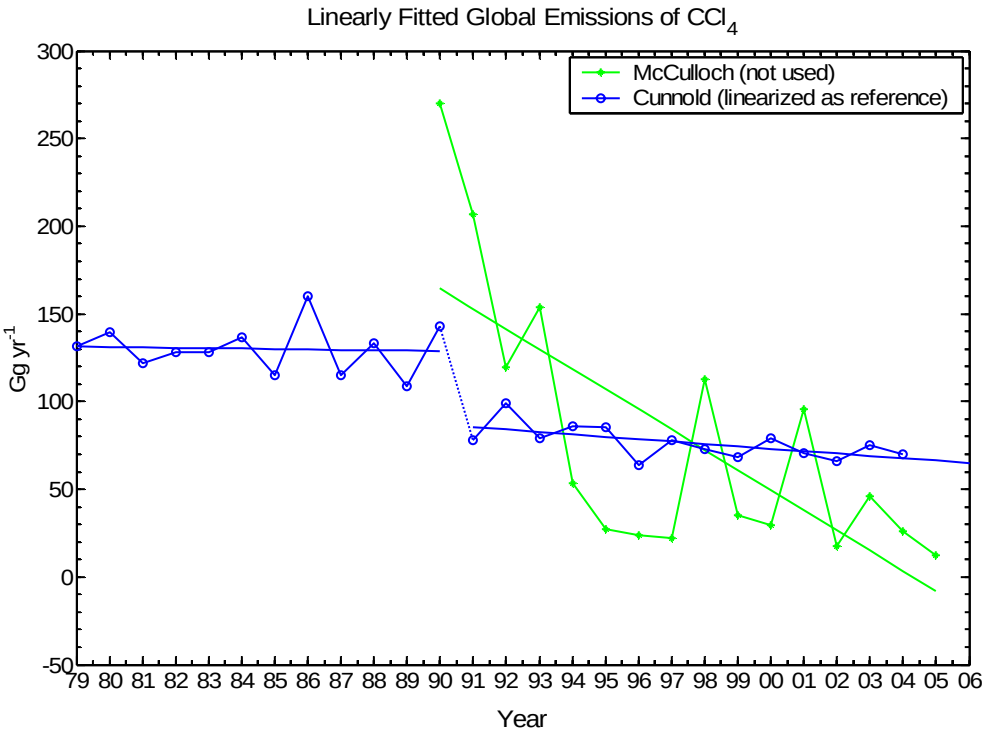

Figure 8.1. Yearly global industrial emission estimates from the industrial sales data [*McCulloch*] (green lines) and from the 2-D model inverse modeling approach [*Cunnold et al*., 1997; *Simmonds et al*., 1998a; updated by *D. Cunnold*] (blue lines). Also shown are the corresponding linearly fitted lines. There are two regimes in the 2-D model emission estimates, and the linearly fitted yearly global emissions for 1996-2004 are used as our references.

Oceanic loss for CCl_4 is significant, as noted earlier, and has a partial lifetime of 94 years. Once dissolved in the water, CCl_4 may be removed by chemical reaction, absorption to particles, and biological consumption. The rate constant for its removal can be expressed as a function of wind speed, temperature, and salinity [*Yvon-Lewis and*

Butler, 2002]. Using knowledge of the spatial and temporal distribution of sea surface temperature, salinity, and wind speed over the oceans, and assuming a global mean mixing ratio of 103 ppt, *Yvon-Lewis and Butler* [2002] have computed monthly oceanic uptake rates of CCl_4 distributed over a 2º × 2º grid of the world's oceans, plus a spatially and temporally constant biological degradation rate. We have converted these maps to the MATCH T42 grids, and scaled them by a constant global factor to reflect an oceanic lifetime of 94 years (The annual average spatial distribution is shown in Figure 8.2, right-hand graph). The distribution indicates that the degradation rate of CCl_4 is the greatest at mid-latitudes in the Northern Hemisphere, resulting from collocated high temperatures and high wind speeds at these latitudes. As noted, these uptake rates are based on a global average mole fraction of 103 ppt. Since the global mole fraction of CCl_4 is decreasing, the global oceanic sink must be decreasing as well. For the optimization we estimate the global oceanic sink at the above seasonal time resolution (DJF, MAM, JJA, and SON) for 1996-2004.

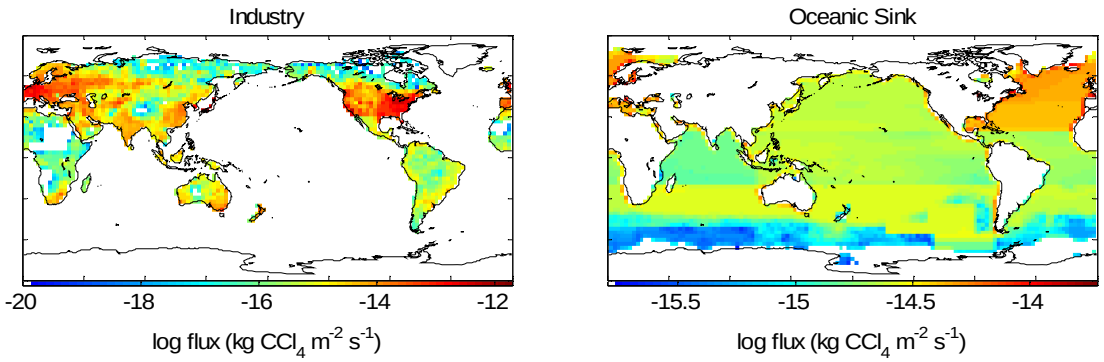

Figure 8.2. Annual average distributions of carbon tetrachloride industrial emissions and oceanic uptake rates. Oceanic sink magnitudes and patterns vary by month. Global industrial emissions have been divided into eight regions, and the magnitude of the oceanic sink is estimated on a global scale as a multiplier on the above sink pattern.

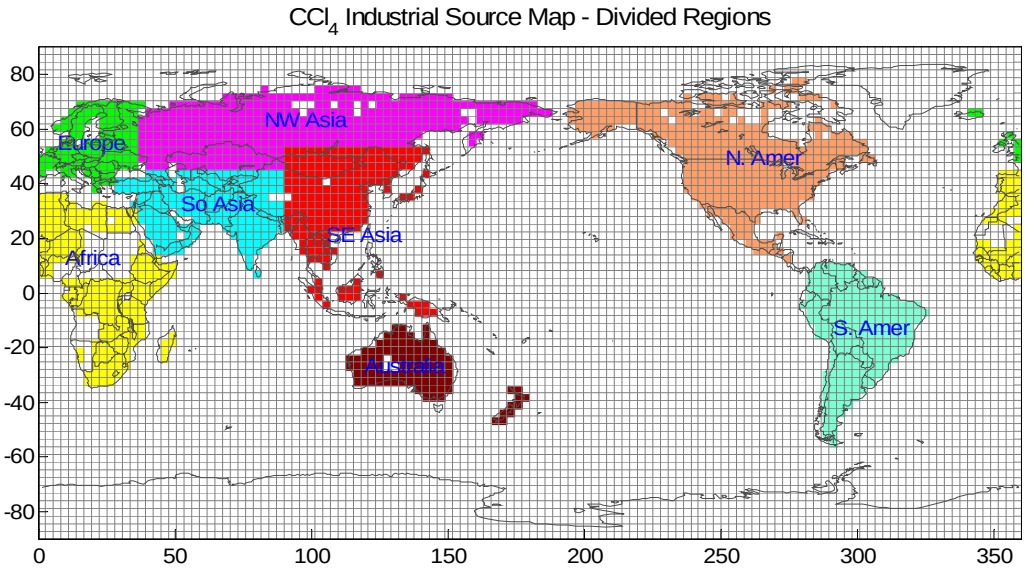

Figure 8.3. Partitioning of the global industrial CCl_4 source into the eight regions is shown along with the T42 MATCH grids. The regional source magnitudes are estimated in the Kalman filter as 3-month average values, and the spatial distribution within each region remains at its a priori distribution.

Stratospheric photodissociation is the most important sink for CCl_4 (reaction between CCl_4 and OH is negligible). The chemical destruction rate constants (J values in s^{-1}) for photodissociation of CCl_4 have been calculated from a more detailed 3-D model for the stratosphere [*Golombek and Prinn*, 1986, 1989, 1993, updated by *A. Golombek*]. We have interpolated their monthly average photodissociation rate fields (that vary with latitude and altitude) to the MATCH grids. These values are then modified by a constant global factor to produce a recommended stratospheric lifetime of ~ 35 years for CCl_4. Due to the very rapid increasing of the J values in the vertical direction in the stratosphere of MATCH, the stratospheric sink is actually overestimated without any adjustment factor. To do the adjustment, we first run the forward model for 4 years from 1992 to 1995, then check the implied stratospheric lifetime, decrease the J values, run the model again, and re-check the inferred lifetime, until we get the appropriate 35-year lifetime. We again check the inferred stratospheric lifetime for the whole reference run from 1996 to 2005 and make any needed adjustment to ensure the time-averaged stratospheric lifetime to be ~ 35 years. We do not explicitly model stratospheric CCl_4 destruction by $O^1(D)$ because it is much weaker than photodissociation. Global soils are also proposed as a sink of CCl_4 that would lower the global lifetime to 20 years. However, because of the spatial correlation with the industrial emissions distribution, and the inconsistency of an overall lifetime of 20 years with the measured interhemispheric gradient, we do not estimate the soil sink directly in this work (if there is a small soil sink it will simply lower the inferred industrial emissions by that small amount).

Consequently, the state vector for the CCl_4 emissions and sink is expressed as:

$$\mathbf{x}_k = \begin{bmatrix} \mathbf{X}^s_k \\ \mathbf{X}^s_{k-1} \\ \mathbf{X}^s_{k-2} \\ \mathbf{X}^s_{k-3} \end{bmatrix} \tag{8.1}$$

where

$$\mathbf{X}^s_k = \begin{bmatrix} x_k^{\text{IND Europe}} \\ x_k^{\text{IND NW Asia}} \\ x_k^{\text{IND So Asia}} \\ x_k^{\text{IND SE Asia}} \\ x_k^{\text{IND Africa}} \\ x_k^{\text{IND Australia}} \\ x_k^{\text{IND N. Amer}} \\ x_k^{\text{IND S. Amer}} \\ x_k^{\text{Ocean}} \end{bmatrix} \tag{8.2}$$

The inversion calculations last from Dec., 1995 to Nov., 2004 (36 seasons total).

Note that the subvector $\mathbf{X}^s_{k-3}$ represents the oldest 3-monthly fluxes at current time step k, and will be removed from the state vector after having used 12 months' observations. However, unlike the other three short-lived chloromethanes, CCl_4 has a very long lifetime (~ 26 years), which means the effect of the old fluxes between season 1 and k-3 will not diminish as quickly as for the three short-lived chloromethanes. Therefore we use an additional term, $\tilde{\mathbf{y}}^{adj}_{k-3}$, to be added to the right-hand side of Equation (4.4), to represent the cumulative effect of the old fluxes which are no longer included in

the state vector [as *Chen and Prinn*, 2006]. Also note that since the global horizontal mixing time in MATCH is ~ 1 year, the effect of the old fluxes should be restricted to the global average concentrations of CCl_4.

The global magnitudes of the reference fluxes and their roles in the state vector are listed in Table 8.1. The a priori errors for the state vector elements are ± 50% (for large magnitudes) to ± 100% of their reference values, which encompass the uncertainty ranges in most of the literature. Table 8.2 summarizes the surface sites whose observations are used in the inversions for CCl_4.

Table 8.1. Reference annual average strengths of the sources and sinks of atmospheric carbon tetrachloride (CCl_4) and their participation in the inversion.

Source/Sink Type [reference]	Seasonality (Y/N ?)	Strength (Gg yr^{-1})	State Vector ?
Industry [*Cunnold et al*., 1997, updated and linearized]	Interannually varying	73 (1996-2004 ave.)	Y (8 regions)
Oceans [*Yvon-Lewis and Butler*, 2002, scaled]	Y	-26	Y (global)
Soils [*Happell and Roche*, 2003]	Y	-27	N
Composite	Y	47	-

Table 8.2. List of the stations whose measurements are used in the inversions for CCl_4, along with their corresponding numbers as in Table 2.1.

(1) MHD	(2) THD	(3) RPB	(4) SMO	(5) CGO	(10) BRW
(11) MLO	(12) NWR	(14) SPO	(15) ALT	(21) KUM	

Note that each element, e.g., $x_k^{\text{IND Europe}}$, is a 3-month average for that region. We use the same emission pulse method as for CH_3Cl, $CHCl_3$, and CH_2Cl_2 to calculate the sensitivities of station mole fractions to the state vector elements. Figure 8.4 (a) and (b) show an example of the calculated sensitivities of individual observing sites to a DJF, 2000 emission pulse from the European region. It is a uniform pulse with an intensity of 10 Gg yr^{-1} lasting for three months. Note that the sensitivities are greatest in the first 3-4 months and then decrease because of atmospheric mixing. The responses at different sites have different patterns depending on their relative proximity to the source region on the global time-varying wind fields. The Mace Head and Alert stations are located near Europe, and therefore they respond rapidly with large response peaks. The other three stations are further away from the source region and therefore their responses are delayed with relatively steady slow increases then decreases in their mole fractions. Also note that the responses at different sites tend to converge to a single value after one year which is consistent with each emission pulse being mixed equally throughout the troposphere by this time.

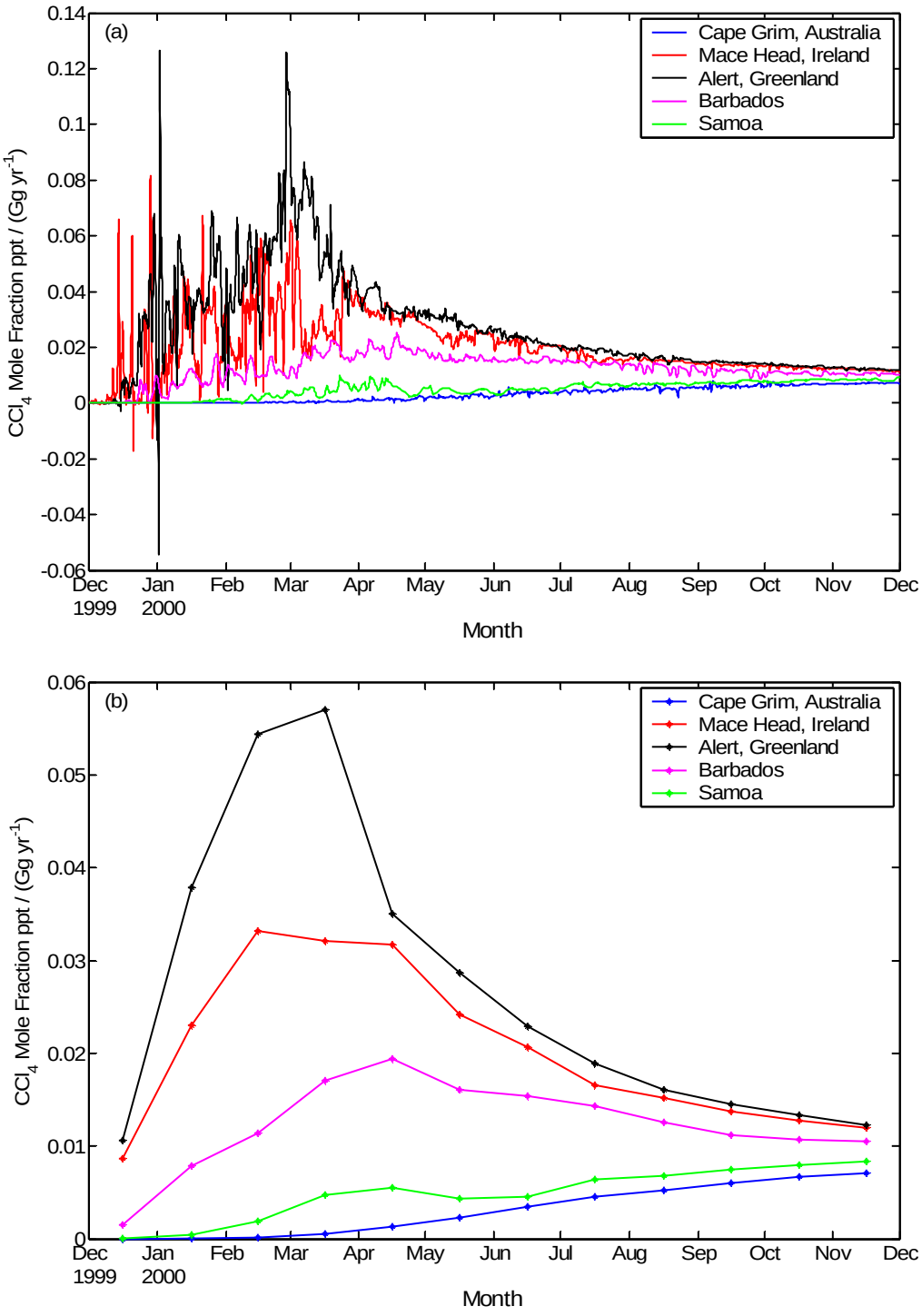

Figure 8.4. MATCH-modeled sensitivities of carbon tetrachloride mole fractions (ppt) to a DJF, 2000 emission pulse from European industry (Gg yr^{-1}), plotted at high frequency (a) and as monthly means (b) at selected atmospheric measuring stations.

8.2. Forward modeling

As we did for the other gases, we first assess the ability of the a priori emission and sink fields to reproduce the carbon tetrachloride observations in the forward runs of MATCH. We initialized the atmospheric 3-D distribution of CCl_4 using the output from a previous multi-year run, scaled to fit the observed mole fractions at remote sites such as Alert, Mauna Loa, and Cape Grim during December, 1995. These stations were chosen because they represent better the global background interhemispheric gradient due to their long distances from strongly emitting sources. The reference run was then made from December, 1995 till August, 2005. Figure 8.5 shows the monthly mean modeled versus observed mole fractions of CCl_4 at the indicated stations over the 9-year period of the simulation. Note the significant differences in the calculated and observed rates of decrease at most stations. We also note that the reference model simulations have larger seasonal cycles than the observations, which are distinct for the NH sites, such as Trinidad Head, CA and Mace Head, Ireland. These seasonal cycles are likely to be attributed to the seasonal variations of the downward flux of CCl_4 from the stratosphere to the troposphere. Stratosphere-troposphere exchange (STE) is a maximum during springtime, and is stronger in the NH than in the SH. Note that stratospheric CCl_4 mole fractions are less than tropospheric mole fractions due to stratospheric photodissociation. Therefore, the net effect is that the mole fractions of CCl_4 at the surface level would decrease because of this downward mixing during springtime. Comparing the model and the observations, we know that this downward mixing is overestimated in the MATCH model, which has also been confirmed by *Jöckel et al*. [2002] in the evaluation of STE in

the MATCH model using observations of ^{14}CO. This overestimated downward mixing of CCl_4 affects our 3-month inversion results leading to their aggregation to 12-month values as discussed below.

8.3. Inversion results

8.3.1. Industrial emissions

Figure 8.6 shows the optimized 3-month average industrial emissions (red lines) from DJF, 1996 to SON, 2004, compared to the linearly decreasing reference values (blue lines). There are significant deviations from the reference case. Overall there are much larger variations in the optimally-estimated emissions than the references (and differ from expectations about the industry). These are likely the responses of the optimized emissions to compensate for the effect of the overestimated downward mixing of CCl_4. For example, if we look at the North American region, there are increasing emissions during springtime to compensate the overestimated decreasing of CCl_4 mole fractions. Because of this, we have aggregated the 3-monthly emissions to annual averages, shown in black lines.

Figure 8.7 shows the reference and optimized yearly regional industrial source strengths between 1996-2004, with their error bars. Substantial decreases in the errors occur for Europe, SE Asia, and N. America, but the decreases elsewhere are small, indicating that the observing network is not sampling air from these other regions very effectively.

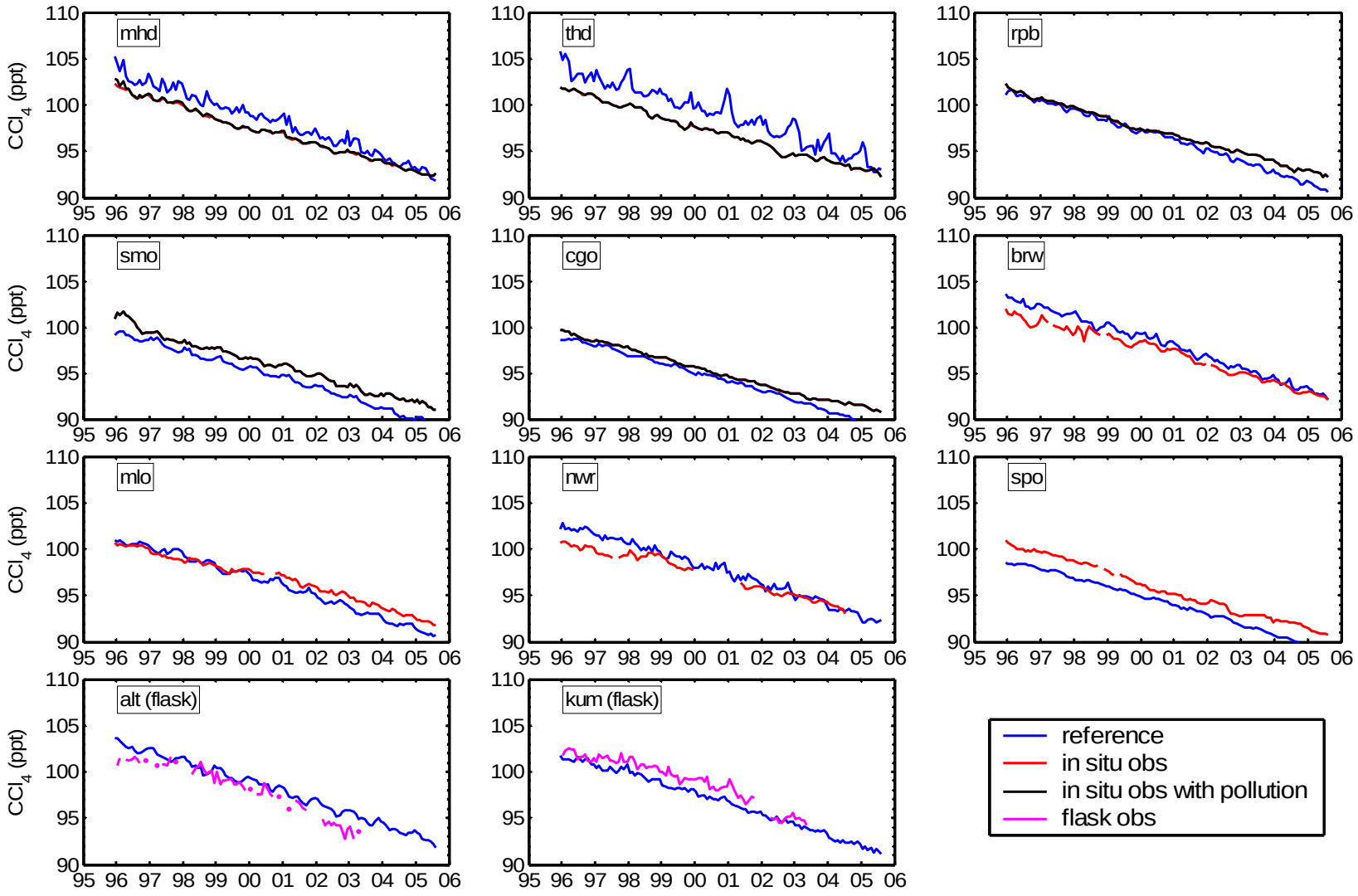

Figure 8.5. The time series of the monthly mean carbon tetrachloride mole fractions computed in the reference model using the a priori (reference) surface fluxes are compared to the observations.

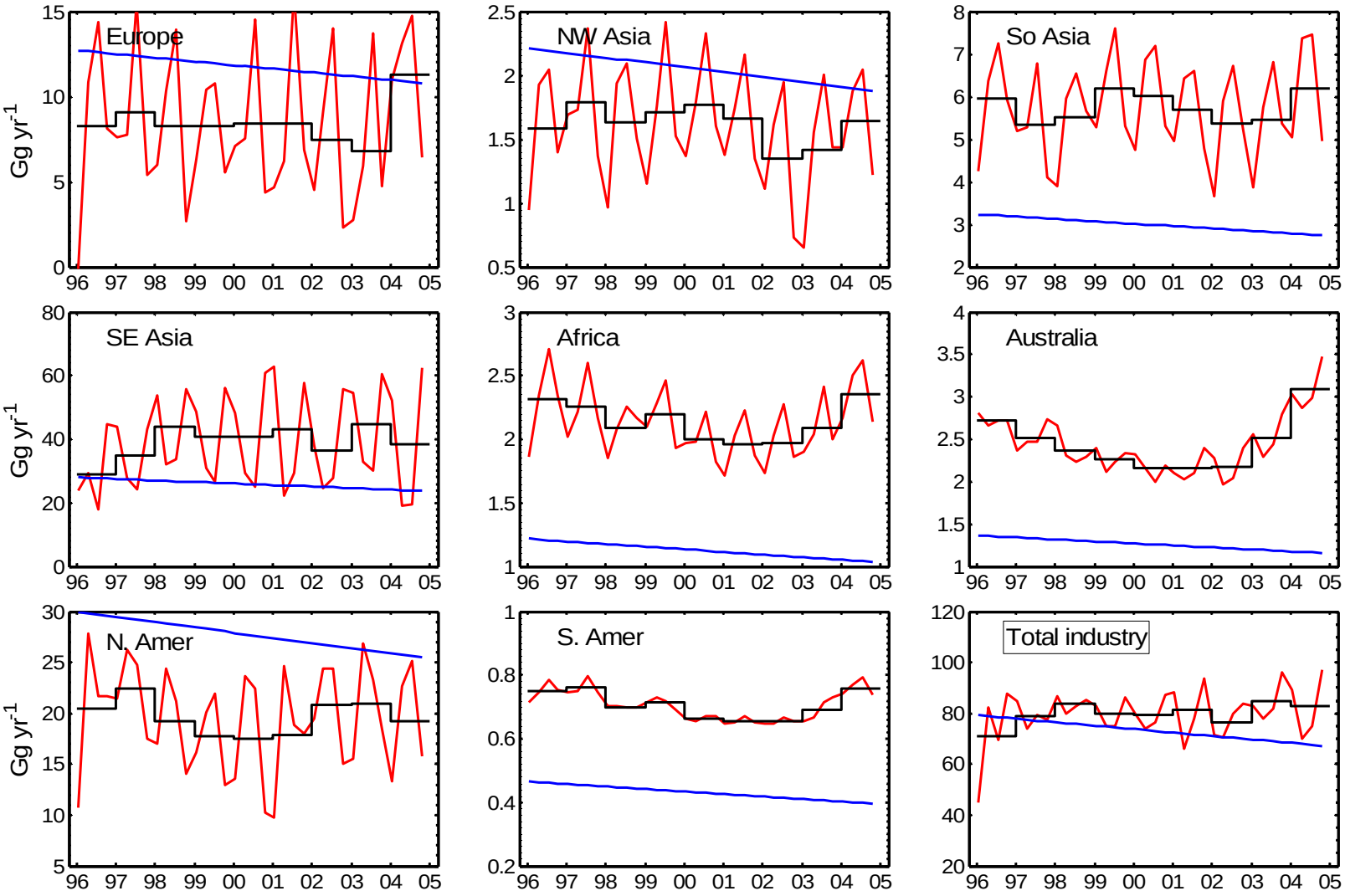

Figure 8.6. Inversion results for the 3-month average regional industrial emissions of carbon tetrachloride. Blue lines show the reference magnitudes, which are linearly decreasing. Red lines show the optimized estimates, along with the aggregated annual averages (black lines). The total industry emissions are the sum of the eight regional emissions.

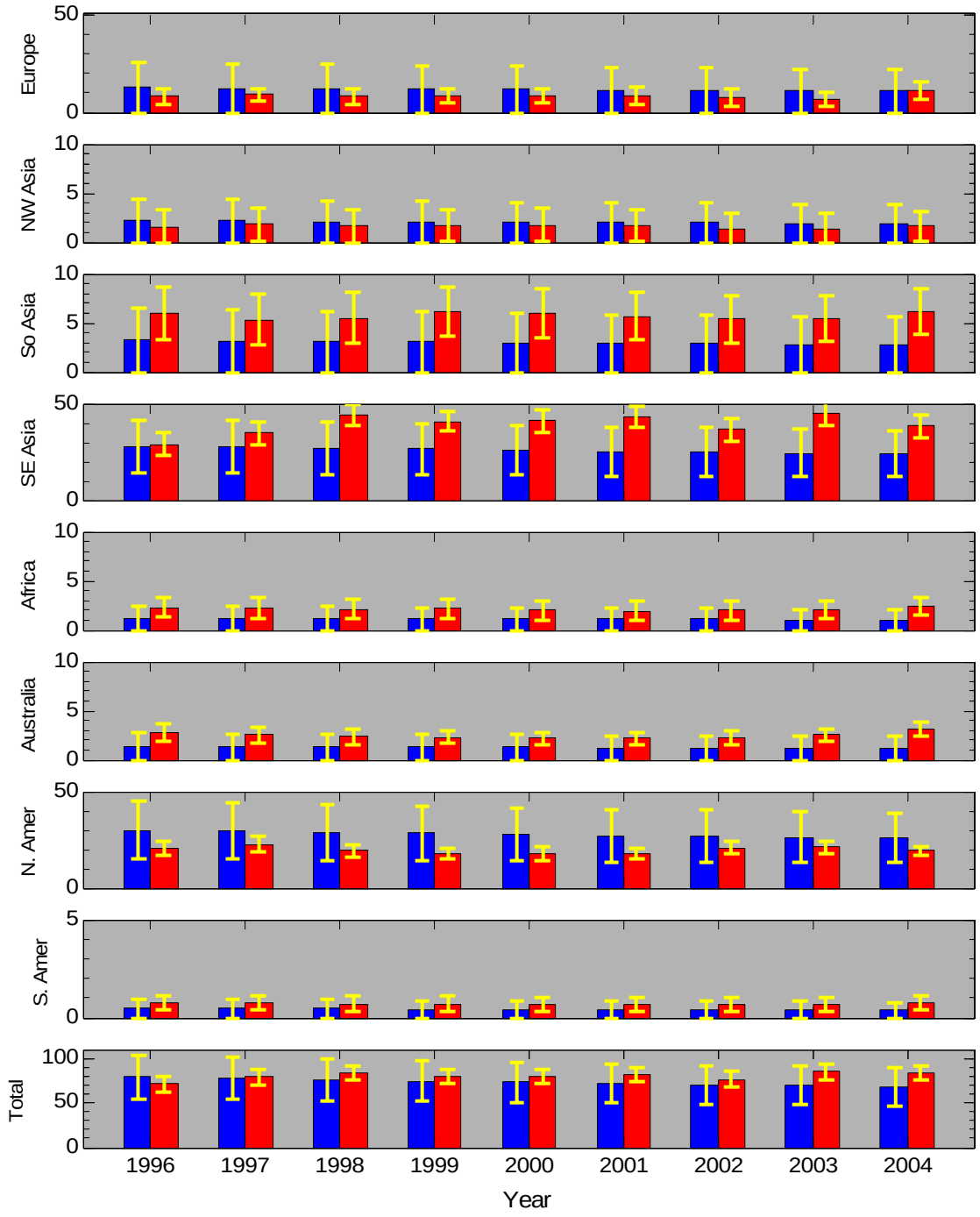

Figure 8.7. Yearly-averaged optimal results of regional industrial emissions of carbon tetrachloride. Blue bars show the reference magnitudes, and red bars show the optimized estimates, each with their respective errors (yellow bars).

Figure 8.8 shows the comparison of the a posteriori optimal estimates and the a priori reference estimates and their relative regional importance to the global total industrial emission. The global optimal estimate of the industrial source is 79.8 ± 8.2 Gg yr^{-1}. Our derived European emissions of 8.5 ± 3.8 Gg yr^{-1} are lower than the estimate of 11.8 Gg yr^{-1} from industry sales data. Our derived Southeast Asian emissions of 39.1 ± 5.7 Gg yr^{-1} are higher than their reference, and the North American emissions of 19.6 ± 3.2 Gg yr^{-1} are slightly less than their reference. Emissions from other regions are relatively small, and the changes from their reference values (and their error reductions) are also small.

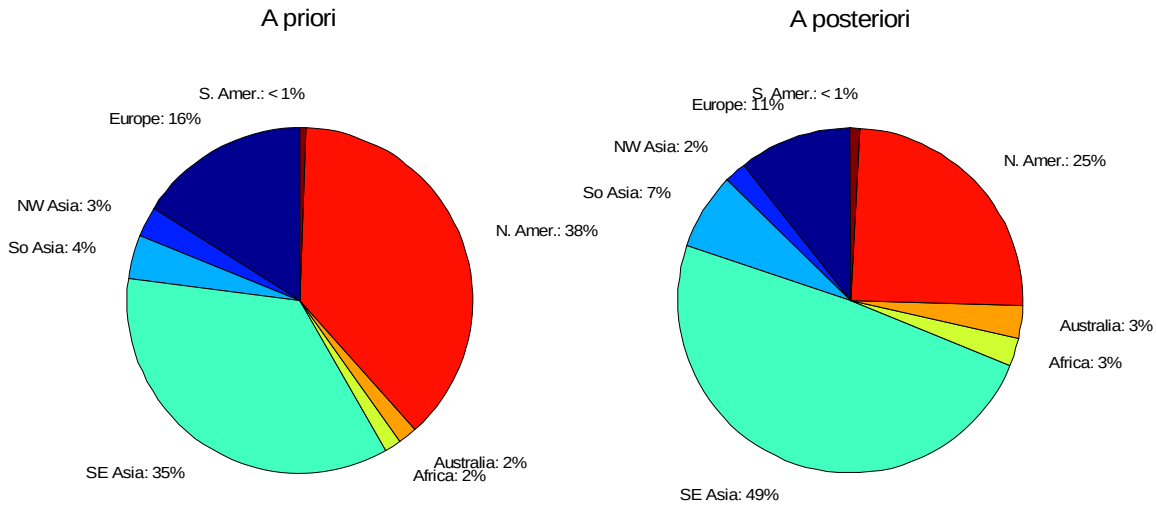

Figure 8.8. A priori (left chart) and a posteriori (right chart) regional contributions to the global industrial emission of carbon tetrachloride.

Figure 8.9 shows the derived yearly global industrial emissions, compared to the estimates from industrial sales data and our reference emissions. Our results actually indicate a slight increasing trend in the global CCl_4 emissions compared to a slight decrease in the reference emissions.

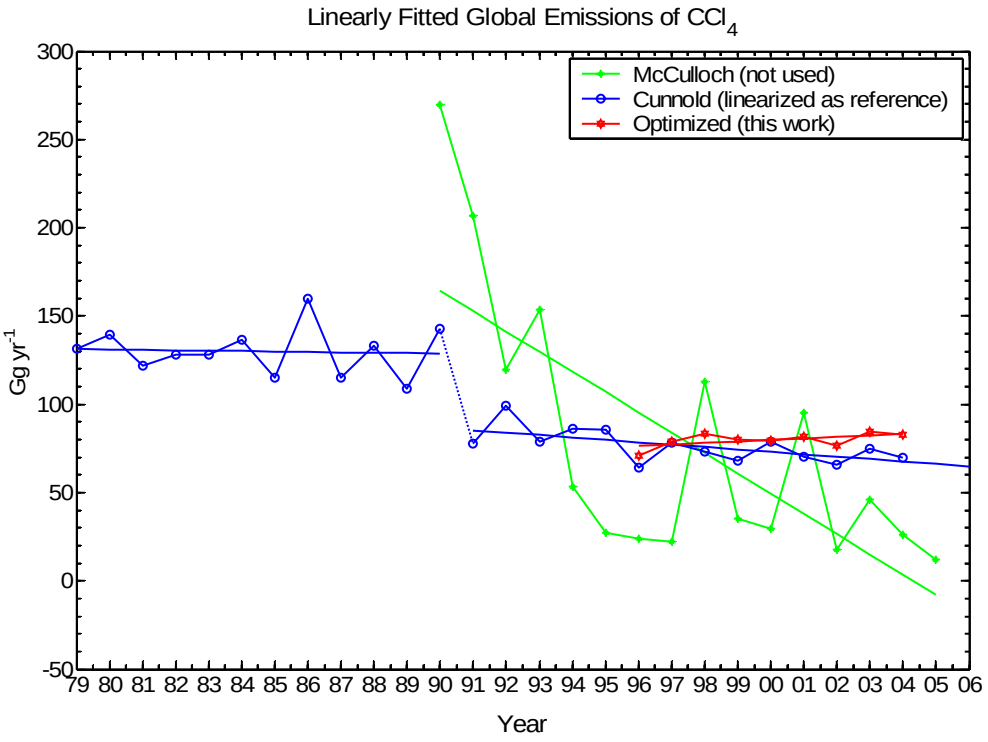

Figure 8.9. Optimal yearly global industrial sources (red lines), compared to yearly global industrial emission estimates from the industrial sales data [*McCulloch*] (green lines) and from the 2-D model inverse modeling approach [*Cunnold et al.*, 1997; *Simmonds et al.*, 1998a; updated by *D. Cunnold*] (blue lines). Also shown are the corresponding linearly fitted lines.

8.3.2. Oceanic uptake

In the Kalman filter the global oceanic CCl_4 uptake rates are solved as seasonal fluxes. Figure 8.10 shows the inversion results compared to the reference ones. To understand the seasonal behavior of the global oceanic sink, we first study the seasonal variations in different semihemispheres (Figure 8.11). In general, the oceanic sink is greatest in summer in the four semihemispheres. The oceanic sink in the HSH has the largest seasonal variability, probably resulting first from the higher winter-summer variations in both of the extratropics (HNH and HSH), and second from the larger oceanic area in the HSH. The dominant seasonal variability in the HSH ocean largely determines the seasonal variability of the global ocean sink. The oceanic sink is stronger in the tropical regions (LNH and LSH) because of the coincidence of higher temperatures and larger oceanic areas there. The optimized global oceanic sink retains the phasing but not the magnitude of the seasonal variations of the a priori sink. The optimized values show significant interannual variability in the global oceanic uptake rate which is also decreasing with time after 2002. Note that the oceanic uptake rate is calculated as the rate constant multiplied by atmospheric mole fraction. Although the uptake rate constant (and the partial lifetime) is independent of the atmospheric burden [*Yvon-Lewis and Butler*, 2002], the globally decreasing CCl_4 mole fractions lead to a decreasing mass of CCl_4 dissolving in the oceans and being destroyed by subsequent chemical reactions and biological consumption over time.

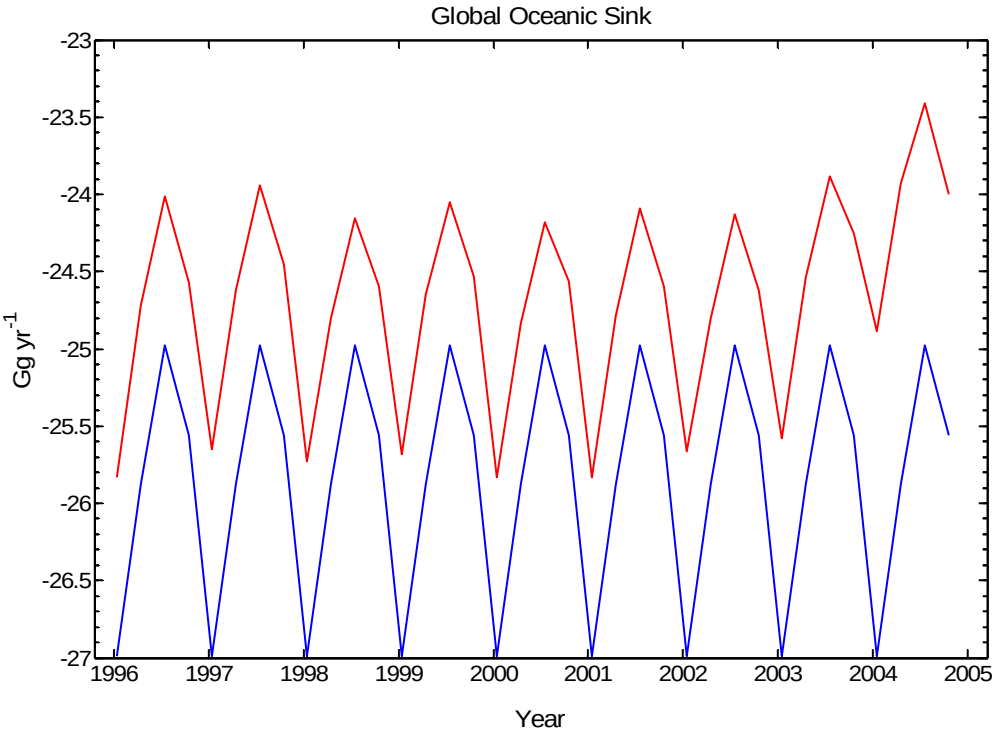

Figure 8.10. Inversion results for the global oceanic sink of carbon tetrachloride. Blue line shows the reference magnitudes, which are annually repeating. Red line shows the optimized estimates, which contain interannual variability.

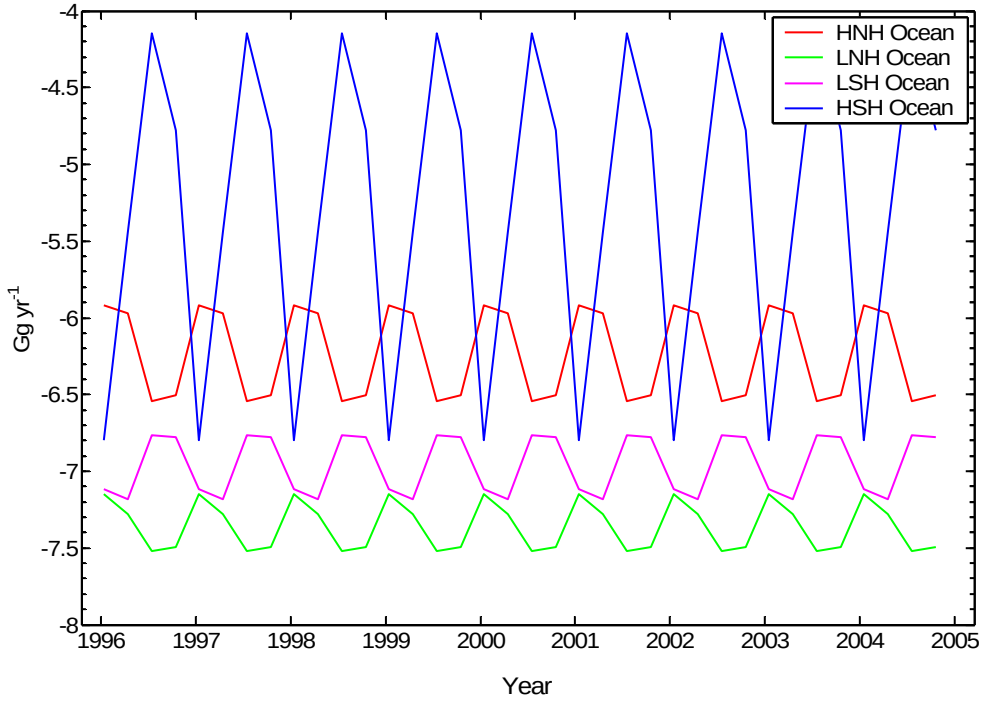

Figure 8.11. Seasonal cycles of the semihemispheric oceanic sinks (negative) of carbon tetrachloride. Note the dominance of the tropical sinks. Oceanic uptake in the HSH has the largest seasonal variation.

8.3.3. Average annual results

The inversion results have been aggregated to compute the global budget of CCl_4. Figure 8.12 and Table 8.3 contain the CCl_4 fluxes averaged over the entire period between 1996-2004. Also shown are the optimized errors, which are always less than the reference errors due to the incorporation of the observations into the Kalman filter. As noted before, the average annual emissions from the European and North American

regions are less then their a priori values which were based on their GDP, presumably because emissions from these regions have been regulated. Emissions from Southeast Asia are much larger than their reference values based on GDP. Global annual uptake by the oceans is less than its a priori magnitude.

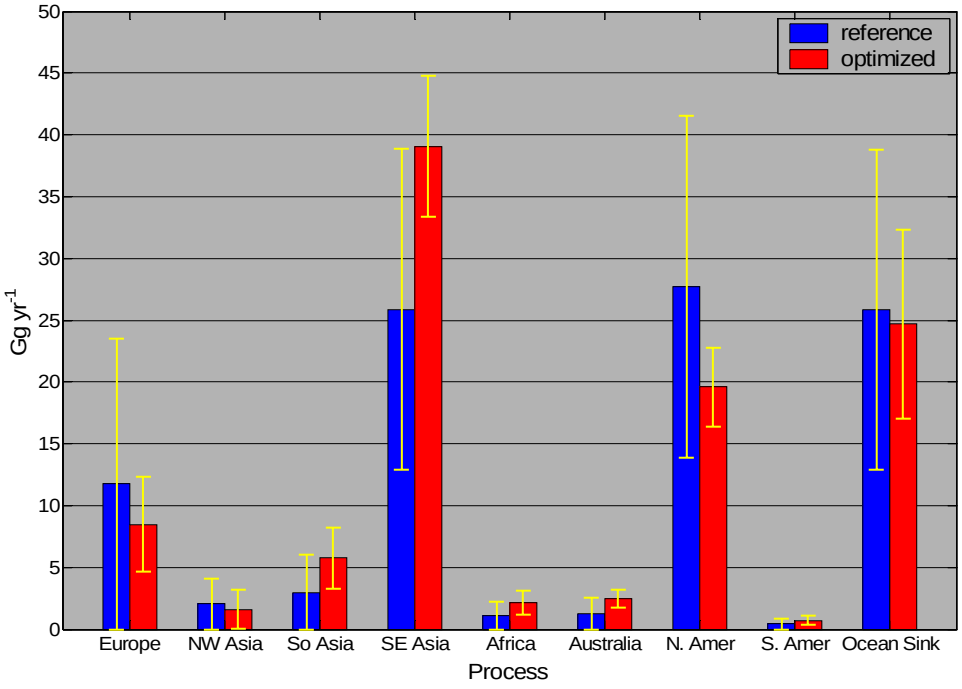

Figure 8.12. Annual average carbon tetrachloride surface flux magnitudes. Shown are the reference (blue bars) and optimized (red bars) values with their 1σ error bars (yellow). The errors on the references are derived from the assumed a priori inversion uncertainties.

Table 8.3. Five-year averaged optimal surface flux values and errors for the industrial sources and oceanic sink (units of Gg yr^{-1}).

Flux type		Reference	Optimization
Industry	Europe	11.8 ± 11.8	8.5 ± 3.8
	NW Asia	2.0 ± 2.0	1.6 ± 1.6
	So Asia	3.0 ± 3.0	5.7 ± 2.5
	SE Asia	25.9 ± 13.0	39.1 ± 5.7
	Africa	1.1 ± 1.1	2.1 ± 1.0
	Australia	1.3 ± 1.3	2.4 ± 0.7
	N. Amer	27.7 ± 13.9	19.6 ± 3.2
	S. Amer	0.4 ± 0.4	0.7 ± 0.4
	Subtotal	73.2 ± 22.7	79.8 ± 8.2
Oceans		-25.9 ± 12.9	-24.7 ± 7.6
Total		47.4 ± 26.1	55.1 ± 11.2

8.4. Inversion check

To test the inversion, we run the forward model with the final optimal emission and sink estimates, and compare the predicted mole fractions with the measurements. Figure 8.13 shows the residuals between the optimized and observed monthly mean mole fractions, compared to the residuals between the reference and observed monthly mean mole fractions at each observing site. The optimal mole fractions tend to be much closer to the observations at most of the sites than the reference as expected from the application of the Kalman filter to the observational time series.

8.5. Summary and conclusions

We have solved for the annual, 3-month-averaged, and interannual surface fluxes of CCl_4 using the Kalman filter as described in Chapter 4. The main conclusions are summarized below.

Overall, for the industrial emissions there are larger temporal variations than in the reference emissions (which are simply linearly decreasing), and we have argued that these seasonal variations are due to the overestimated downward mixing of CCl_4. Because of this we have aggregated the 3-monthly emissions to 12-month averages. The three regions of Europe, Northwest Asia, and North America show smaller optimized emissions relative to their a priori values which were based on their GDP. This is presumably because emissions from these regions are being regulated. Our derived Southeast Asian emissions are much larger than their reference values. Emissions from

other regions are relatively small and do not vary too much from their reference values. Our results actually indicate a slight increasing trend in the global CCl_4 industrial emissions.

The seasonal variability of the global oceanic sink is dominated by the seasonal variability of the HSH oceans, which is greatest in summer and weakest in winter. The optimized values also show significant interannual variability in the global oceanic uptake rate which is decreasing with time. The globally decreasing CCl_4 mole fractions have led to a decreasing mass of CCl_4 being dissolved each year in the oceans and being destroyed there by chemical reactions and biological consumption.

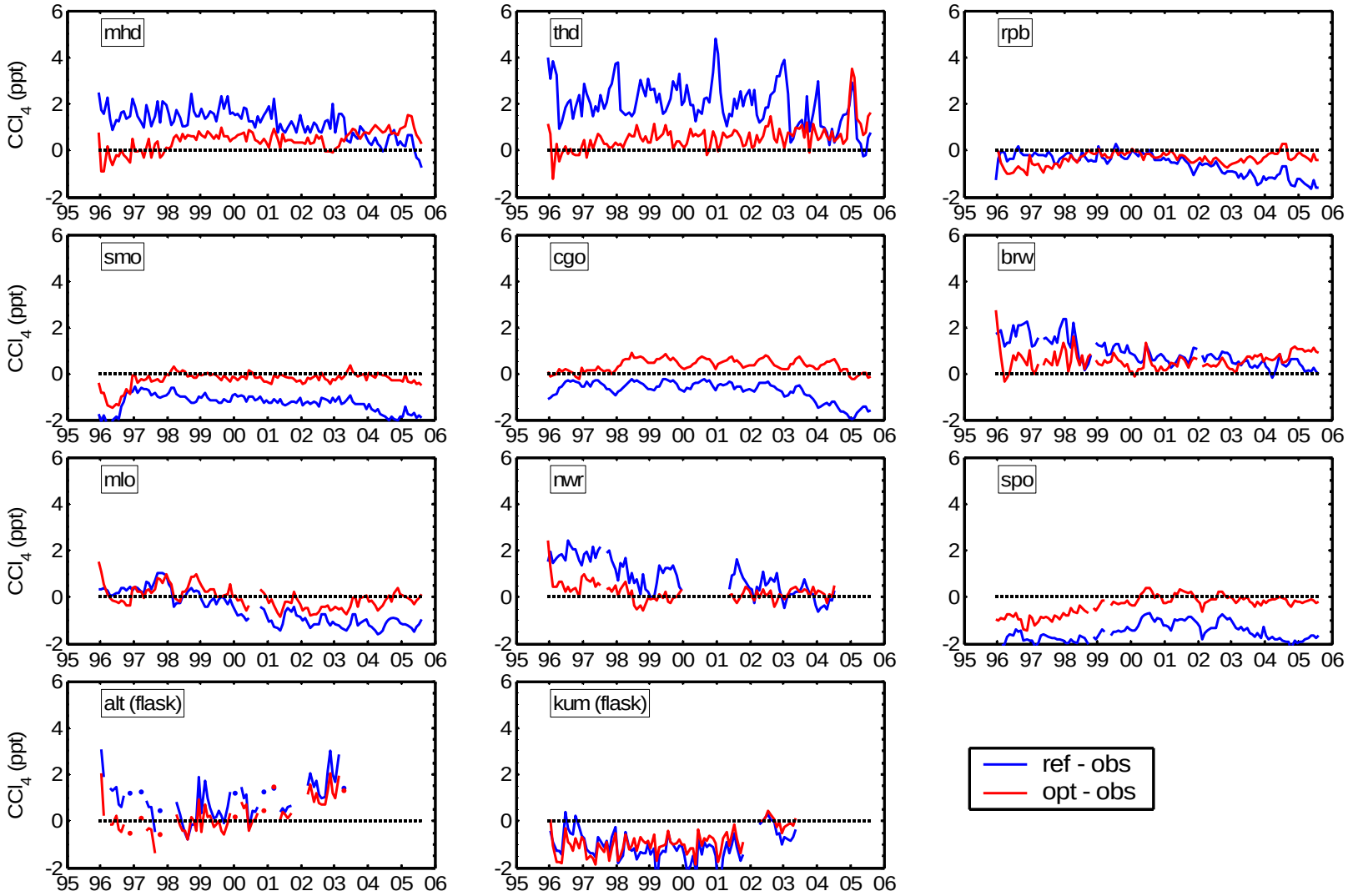

Figure 8.13. Residuals between the optimized and observed monthly mean mole fractions of carbon tetrachloride (red lines), compared to the residuals between the reference and observed monthly mean mole fractions (blue lines) at each observing site.

Chapter 9

Conclusions

The goal of the thesis was to estimate global chloromethane surface flux magnitudes using a 3-D inverse modeling approach. This work is to our knowledge the very first 3-D inverse modeling for the global emissions of chloroform, dichloromethane, and carbon tetrachloride. For methyl chloride and also the other three gases, some new, previously unused elements have been incorporated into the work: (1) interannually varying driving meteorology from reanalysis of observations, (2) optimization of interannual monthly (or 3-monthly) surface fluxes using the adapted Kalman filter, and (3) high frequency observations. In this final chapter, we briefly summarize the main results and findings from the preceding chapters. Some general conclusions are then drawn from these results.

9.1. Summary of the inversion results

We have used the discrete Kalman filter to estimate the seasonal, annual, and interannual surface fluxes associated with the major sources and sinks of the four chloromethanes at monthly resolution (for CH_3Cl, CH_2Cl_2, and $CHCl_3$) or 3-monthly resolution (for CCl_4), on regional or global scales. This inversion technique combines observations of the chloromethane concentrations (as monthly average mole fractions) taken at the surface stations of the AGAGE and other global networks, with a representation of the MATCH atmospheric transport and chemistry model using the Jacobian (sensitivity) matrix computed in MATCH by finite differences. This time dependent Jacobian matrix maps time-invariant, monthly, or 3-monthly flux pulses on regional/global scales onto the resulting changes in the monthly average chloromethane concentration at every observing station. The quality of the solutions to the inversion problems was based on the accuracy of the inversion flux results as computed in the Kalman filter, the consistency of the optimized model with the observations taking account of the measurement statistics, the initial conditions, and the a priori information about the unknown surface fluxes.

9.1.1. Methyl chloride inverse modeling

Atmospheric methyl chloride (CH_3Cl) is the major continuous natural source of chlorine in the stratosphere. The tropospheric lifetime for CH_3Cl is sufficiently long, 1.3 years, so that a significant quantity of emitted CH_3Cl can be transported upwards through the tropopause. In the stratosphere, as in the troposphere, CH_3Cl is removed primarily by

reaction with the OH free radical. There are many kinds of natural sources and sinks of CH_3Cl, and they are affected by seasonal and longer-term climatic changes in complicated ways. We solved for eight seasonal (time-varying) and one aseasonal (constant) CH_3Cl flux processes/regions between 2000-2004, and examined the optimized fluxes in terms of multi-year averages, seasonal, and monthly interannual variability. The main findings are:

- The CH_3Cl inversion results indicate large CH_3Cl emissions of ~ 2240 Gg yr^{-1} from tropical plants. Relative to their a priori (literature) magnitudes, the inversion nearly doubles global fungal emissions, slightly increases emissions from tropical plants, biomass burning and salt marshes, and reduces the global oceanic source and soil sink. The inversion also implies greater seasonal oscillations of the natural sources and soil sink of CH_3Cl compared to their a priori values.

- The inversion also implies strong effects of the 2002/2003 globally wide-spread warming and drought on the emissions from tropical plants, eastern hemisphere biomass burning, and global salt marshes, and also on the global soil sink. The 2002/2003 El Niño event was a moderate one in which the global land precipitation appeared unusually low. There is independent evidence showing that a global land dryness might lead to a strong NPP decrease and therefore a subsequent decrease in emissions by tropical plants and a decrease in global soil microbially-aided consumption. The anomalously dry and hot climate might also

lead to increased insect damage to vegetation and increased susceptibility of vegetation to burning, thus resulting in increased global emissions of CH_3Cl from biomass burning. Future climate change involving an increasingly dry and hot summer climate may lead to increased susceptibility to decreased NPP (and hence decreased tropical plant emissions), increased CH_3Cl emissions from biomass burning, increased salt marsh plant emissions, and decreased soil organic matter content and thus microbially-aided CH_3Cl uptake by soils.

9.1.2. Chloroform inverse modeling

Atmospheric chloroform ($CHCl_3$) is largely of natural origin, with emissions from biomass burning, oceans, and soils, and minor emissions from industrial activity. The atmospheric lifetime of $CHCl_3$ is relatively short (0.41 years), resulting from its efficient destruction by OH radicals. We estimated monthly global emissions from the biomass burning source for 2000-2004, because of the presumed small magnitudes and insignificance in the total budget of $CHCl_3$, and we estimated monthly oceanic and soil emissions on semihemispheric scales between 2000-2004. The industrial emissions are kept as their references. The main findings are:

- Biomass burning is still indicated as a minor source of chloroform and its estimated seasonal variations do not change from its a priori values.

- The relative importance of the oceanic and terrestrial sources tends to be equal. Seasonal cycles have been derived for both the oceanic and terrestrial sources,

with summer maximum and winter minimum emissions, because both processes are microbially driven and the relevant microbial activities increase in warmer environments.

- Like CH_3Cl, the interannual variability of the derived $CHCl_3$ oceanic and soil fluxes reflects the impact of the 2002/2003 globally wide-spread warming and drought. The anomalously high emissions from the HNH oceans in the summers of 2002 and 2003 might have been caused by the high sea surface temperature anomalies there, and the low emission anomalies from the HNH and LNH soils in the summer of 2003 and from the LSH and HSH soils in the winters (SH) of 2002 and 2003 might have been caused by the extreme droughts in these two consecutive years.

9.1.3. Dichloromethane inverse modeling

Atmospheric dichloromethane (CH_2Cl_2) is largely of anthropogenic origin, with smaller emissions from biomass burning and oceans. The atmospheric lifetime of CH_2Cl_2, like $CHCl_3$, is relatively short (0.38 years), resulting from its efficient destruction by OH radicals. We estimated the average industrial emissions of CH_2Cl_2 during the five-year period (2000-2004) from eight continental regions. For the natural sources, we estimated monthly emissions from biomass burning and the oceans on semihemispheric scales between 2000-2004. The main findings are:

- For the industrial emissions, our derived European emissions are much lower than the a priori estimates from the industry sales data, but are only marginally lower than the published estimates from the back-attribution technique and the CO ratio method using CO emission inventories. Our inversion results show very significant emissions from the Southeast Asian region, while the North American emissions slightly decrease from their a priori values. Emissions from other regions are relatively small.

- For the biomass burning source, emissions are concentrated in the tropical regions. Our inversion generally retains the seasonal cycles of the reference emissions, with emissions in Central Africa, India, and Southeast Asia peaking in April and May (Northern Spring), and emissions in South America and South Africa peaking in October and November (Southern spring). For both tropical regions, the biomass burning emissions are strongest during the spring term, associated with the warm and dry season conditions at that time leading to the largest amount of biomass burned. Relatively high emissions from biomass burning in the LNH and LSH in the two-year time frame of 2002/2003 might have been caused by the extreme 2002/2003 global wide-spread warming and drought conditions.

- The derived oceanic emissions show well-established seasonal variations in the HNH, LNH and HSH with summer maxima and winter minima. The inversion, as in the reference, still indicates the greater importance of tropical oceanic emissions relative to high latitude emissions, probably related to the higher sea

surface temperatures and supersaturation in tropical regions. The physical, chemical or biological details of the processes that are involved in dichloromethane production warrant further investigation. Measurements of oceanic saturation levels throughout the year would be needed to establish whether the ocean is indeed a net source or is simply re-emitting in summer the CH_2Cl_2 that was taken up in winter.

9.1.4. Carbon tetrachloride inverse modeling

Atmospheric carbon tetrachloride (CCl_4) is controlled by the Montreal Protocol and its various amendments due to its much longer lifetime (26 years) and much larger ozone depletion potential. CCl_4 is thought to originate almost exclusively from anthropogenic processes, although there may be some small natural sources. The principal sink of CCl_4 is stratospheric photodissociation resulting in a partial atmospheric lifetime of ~ 35 years; the oceans have been identified as the second largest sink with a partial lifetime of ~ 94 years. We estimated eight regional industrial sources and the global oceanic sink at a 3-month time resolution between 1996-2004. The main findings are:

- For the industrial emissions, there are overall larger oscillations in the inversions than in the references (which were simply linearly decreasing), probably because of the overestimated downward mixing of CCl_4 in MATCH. Therefore we have aggregated the 3-monthly emissions to 12-month averages. For Europe, Northwest Asia, and North America we estimate smaller emissions relative to their a priori values (which were based simply on GDP). This is presumably

because emissions from these regions are regulated under the Montreal Protocol. Our derived Southeast Asian emissions are much larger than its reference values. Emissions from other regions are relatively small. Our inversion results indicate a slight increasing trend in the global CCl_4 emissions relative to the reference.

- The seasonal variability of the global oceanic sink is dominated by the seasonal variability of the HSH oceans, where uptake is the greatest in summer and weakest in winter. The optimized values indicate significant interannual variability in the global oceanic uptake rate which shows a decreasing trend with time. This is consistent with the globally decreasing CCl_4 mole fractions leading to a decreasing mass of CCl_4 dissolved in the oceans and thus destroyed by chemical reactions and biological consumption.

9.2. Further comments on the inverse modeling approach

Our inversion approach using the discrete Kalman filter has been based on assumptions made about the observations, the model, the construction of the state vector, and the nature of the inversion technique itself. Thus the accuracy of the inversion results and the extent of the reduction of the a priori uncertainties depend on these assumptions.

9.2.1. Effects of measuring frequency and spatial coverage of the observations in constraining the surface fluxes

The inverse modeling approach is of course strongly dependent on the observed data. Throughout the thesis we used both high frequency real time in situ and low frequency flask observations from different observing laboratories. The differences in their calibration standards have been accounted for based on inter-comparisons of the chloromethane concentrations at common sites. In situ data have been collected within a window of 1-3 hours on either side of the time of collection of the flask data. Observational errors accounting for instrumental precision, model grid and site mismatch, and limited sampling frequency have been included in the inversions.

Since the squares of the observational errors determine inversely in the Kalman filter how useful the observations are in updating the state vector, high and low frequency observations receive different weights in the inverse modeling. The much lower weekly/bi-weekly frequency flask data (~ 4 per month) have errors about 15 to 16 times larger than the high frequency observations (~ 1000 per month), and therefore have much less influence in determining the optimal surface fluxes. However, this disadvantage can be offset at some of the flask sites that are very sensitive to specific regional fluxes given their strategic geographical locations, such as Palmer station (for the HSH region), Mauna Loa for $CHCl_3$ and CH_2Cl_2 (for the tropical oceanic or plant emissions), Niwot Ridge for $CHCl_3$ and CH_2Cl_2, and Harvard Forest station (for emissions from the USA).

These comments refer to the currently available flask measuring locations, which are chosen based on accessibility and budget constraints, as well as scientific desirability.

The limitations in the spatial coverage of the in situ and flask observations play an important role in the limiting the accurate deduction of surface fluxes from specific regions. In Chapter 7, in the estimation of the industrial emissions of CH_2Cl_2, we were forced to aggregate the European region and NW Asia, because no observations are available in the NW Asian area. Most of the sites are located in the Northern Hemisphere, typically in the middle or high latitudes, and very few observations are available for the Southern Hemisphere. Typically there is only one site (American Samoa) for the LSH. How well can American Samoa alone represent the entire Southern Hemisphere tropics? Can it distinguish between the land and oceanic area? The answer to both questions is probably, no. Furthermore, there are no data for the whole of South America and Africa. If we had stations in these regions (NW Asia, South America, and Africa), for example if we had one measuring site in the coastal region of each, not only would the fluxes from these regions be better deduced, but also the fluxes from neighboring regions be better constrained.

The above comments are still based on fairly coarse ($2.8^\circ \times 2.8^\circ$) spatial scale inverse modeling. In the future we would hope to solve for emissions from smaller regions and/or countries. This is especially true for the industrial emissions of CCl_4, for which the production and consumption data within each country are required to be reported to UNEP. This also requires more spatially dense global measuring networks. An inversion

technique such as the Kalman filter can in principle be adapted to determine an optimal network given any limitations on the number of sites.

9.2.2. Effects of the prescribed spatial structures within large regions

Improved bottom-up studies that produce more realistic high resolution spatial distributions of the chloromethane surface fluxes are also essential to improving their simulations. In Chapter 7, in the simulation of dichloromethane mole fractions, we showed that non-uniform oceanic emissions reproduced the actual observations much more successfully. Because our inversions assumed fixed (but non-uniform) spatial distributions within each region that were obtained from these bottom-up estimates, the inclusion of more realistic spatial distributions into the top-down approach should result in more accurate flux estimates. Moreover, although the inverse modeling approach can quantitatively estimate the flux magnitudes, field and laboratory experiments are still necessary to study the mechanisms of the fluxes, especially for the biogeochemical processes that control the natural sources and sinks of the chloromethanes.

References

Asplund, G., J. V. Christiansen, and A. Grimvall (1993), A chloroperoxidase-like catalyst in soil: detection and characterization of some properties, *Soil Biology and Biochemistry, 25*, 41-46.

Aucott, M. L., A. McCulloch, T. E. Graedel, G. Kleiman, P. Midgley, and Y. Li (1999), Anthropogenic emissions of trichloromethane (chloroform, $CHCl_3$) and chlorodifluoromethane (HCFC-22): Reactive Chlorine Emissions Inventory, *J. Geophys. Res.*, *104*(D7), 8405-8415.

Ayres, M. P., and M. J. Lombardero (2000), Assessing the consequences of global change for forest disturbance from herbivores and pathogens, *Sci. Total Environ., 262*, 263-286.

Balzter, H., F. F. Gerard, C. T. George, C. S. Rowland, T. E. Jupp, I. McCallum, A. Shvidenko, S. Nilsson, A. Sukhinin, A. Onuchin, and C. Schmullius (2005), Impact of the Arctic oscillation pattern on interannual forest fire variability in Central Siberia, *Geophys. Res. Lett.*, *32*, L14709, doi:10.1029/2005GL022526.

Butler, J. H., M. Battle, M. Bender, S. A. Montzka, A. D. Clarke, E. S. Saltzman, C. Sucher, J. Severinghaus, and J. W. Elkins (1999), A twentieth century record of atmospheric halocarbons in polar firn air, *Nature*, *399*, 749-755.

Chen, Y.-H. (2004), Estimation of methane and carbon dioxide surface fluxes using a 3-D global atmospheric chemical transport model, PhD thesis, MIT, Cambridge.

Chen, Y.-H., and R. G. Prinn (2005), Atmospheric modeling of high- and low-frequency methane observations: Importance of interannually varying transport, *J. Geophys. Res.*, *110*, D10303, doi:10.1029/2004JD005542.

Chen, Y.-H., and R. G. Prinn (2006), Estimation of atmospheric methane emissions between 1996 and 2001 using a three-dimensional global chemical transport model, *J. Geophys. Res.*, *111*, D10307, doi:10.1029/2005JD006058.

Ciais, P., et al. (2005), Europe-wide reduction in primary productivity caused by the heat and drought in 2003, *Nature*, *437*, 529-533.

Cleveland, C. C., E. A. Holland, and J. C. Neff (1993), Temperature regulation of soil respiration in an alpine tundra ecosystem, paper presented at the Front Range Branch Annual Meeting, Am. Geophys. Union, Golden, Colo., Feb. 8-10.

Collins, W. D., P. J. Rasch, B. E. Eaton, B. V. Khattatov, J. F. Lamarque, and C. S. Zender (2001), Simulating aerosols using a chemical transport model with assimilation of satellite aerosol retrievals : methodology for INDOEX, *J. Geophys. Res.*, *106*(D7), 7313-7336.

Collins, W. D., P. J. Rasch, B. E. Eaton, D. W. Fillmore, J. T. Kiehl, C. T. Beck, and C. S. Zender (2002), Simulation of aerosol distributions and radiative forcing for INDOEX: regional climate impacts, *J. Geophys. Res.*, *107*(D19), 8028, doi: 10.1029/2000JD000032.

Cox, M. L., G. A. Sturrock, P. J. Fraser, S. T. Siems, P. B. Krummel, and S. O'Doherty (2003), Regional sources of methyl chloride, chloroform and dichloromethane identified from AGAGE observations at Cape Grim, Tasmania, 1998-2000, *J. Atmos. Chem.*, *45*, 79-99.

Cunnold, D. M., R. G. Prinn, R. A. Rasmussen, P. G. Simmonds, F. N. Alyea, C. A. Cardelino, A. J. Crawford, P. J. Fraser, and R. D. Rosen (1983), The Atmospheric Lifetime Experiment 3. Lifetime methodology and application to three years of $CFCl_3$ Data, *J. Geophys. Res.*, *88*(C13), 8379-8400.

Cunnold, D. M., P. J. Fraser, R. F. Weiss, R. G. Prinn, P. G. Simmonds, B. R. Miller, F. N. Alyea, and A. J. Crawford (1994), Global trends and annual releases of CCl_3F and CCl_2F_2 estimated from ALE/GAGE and other measurements from July 1978 to June 1991, *J. Geophys. Res.*, *99*(D1), 1107-1126.

Cunnold, D. M., R. F. Weiss, R. G. Prinn, D. E. Hartley, P. G. Simmonds, P. J. Fraser, B. R. Miller, F. N. Alyea, and L. Porter (1997), GAGE/AGAGE measurements indicating reductions in global emissions of CCl_3F and CCl_2F_2 in 1992-1994, *J. Geophys. Res.*, *102*(D1), 1259-1269.

Elkins, J. W., S. A. Montzka, T. M. Thompson, T. H. Swanson, A. D. Clarke, F. L. Moore, D. F. Hurst, P. A. Romashkin, S. A. Yvon-Lewis, J. M. Lobert, M. Dicoreleto, G. S. Dutton, L. T. Lock, D. B. King, R. E. Dunn, E. A. Ray, M. Pender, P. R. Wamsley, and C. M. Volk (1998), Nitrous oxide and halocompounds, in J. H. Butler, D. J. Hofmann, J. T. Peterson, and R. M. Rosson (eds.), *Climate Monitoring and Diagnostics Laboratory Summary Report No. 24, 1997*, Department of Commerce, Boulder, Colorado, U. S., Chap. 5, pp. 91-121.

Gelb, A., J. F. Kasper, Jr., R. A. Nash, Jr., C. F. Price, and A. A. Sutherland, Jr. (1974), *Applied Optimal Estimation*, 374 pp., M.I.T. Press, Massachusetts Institute of Technology, Cambridge, Massachusetts, 13th printing.

Golombek, A., and R. G. Prinn (1986), A global three-dimensional model of the circulation and chemistry of CCl_3F, CCl_2F_2, CH_3CCl_3, CCl_4, and N_2O, *J. Geophys. Res.*, *91*, 3985-4001.

Golombek, A., and R. G. Prinn (1989), Global three-dimensional model calculations of the budgets and present-day atmospheric lifetimes of $CF_2ClCFCl_2$ (CFC-113) and $CHClF_2$ (CFC-22), *Geophys. Res. Lett.*, *16*, 1153-1156.

Golombek, A., and R. G. Prinn (1993), A global three-dimensional model of the stratospheric sulfuric acid layer, *J. Atmos. Chem.*, *16*, 179-199.

Graedel, T. E., and W. C. Keene (1995), The tropospheric budget of reactive chlorine, *Global Biogeochem. Cycles*, *9*, 47-77.

Graedel, T. E., and W. C. Keene (1996), The budget and cycle of Earth's natural chlorine, *Pure and Appl. Chem.*, *68*, 1687-1689.

Graedel, T. E., and W. C. Keene (1999), Preface, *J. Geophys. Res.*, *104*(D7), 8331-8332.

Guenther, A., C. N. Hewitt, D. Erickson, R. Fall, C. Geron, T. Graedel, P. Harley, L. Klinger, M. Lerdau, W. A. McKay, T. Pierce, B. Scholes, R. Steinbrecher, R. Tallamraju, J. Taylor, and P. Zimmerman (1995), A global model of natural volatile organic compound emissions, *J. Geophys. Res., 100*(D5), 8873-8892.

Hack, J. J. (1994), Parameterization of moist convection in the National Center for Atmospheric Research community climate model (CCM2), *J. Geophys. Res.*, *99*, 5551-5568.

Hao, W. M., and M.-H. Liu (1994), Spatial and temporal distribution of tropical biomass burning, *Global Biogeochem. Cycles*, *8*(4), 495-503.

Happell, J. D., and M. P. Roche (2003), Soil: a global sink of atmospheric carbon tetrachloride, *Geophys. Res. Lett.*, *30*(2), 1088, doi:10.1029/2002GL015957.

Hartley, D. E., and R. G. Prinn (1993), On the feasibility of determining surface emissions of trace gases using an inverse method in a three-dimensional chemical transport model, *J. Geophys. Res.*, *98*, 5183-5198.

Haselmann, K. F., R. A. Ketola, F. Laturnus, F. R. Lauritsen, and C. Grøn (2000a), Occurrence and formation of chloroform at Danish forest sites. *Atmos. Environ., 34*, 187-193.

Haselmann, K. F., F. Laturnus, F., and C. Grøn (2002), Formation of chloroform in soil – a year-round study at a Danish spruce forest site. *Water, Air Soil Pollut., 139*, 35-41.

Hjelm, O. (1996), Organohalogens in Coniferous Forest Soil, Ph.D. Thesis, Linköping studies in arts and science No 139, University of Linköping, Sweden.

Hoekstra, E. J., F. J. M. Verhagen, J. A. Field, E. W. B. De Leer, and U. A. Th. Brinkman (1998a), Natural production of chloroform by fungi, *Phytochem.*, *49*, 97-99.

Hoekstra, E. J., E. W. B. De Leer, and U. A. Th. Brinkman (1998b), Natural formation of chloroform and brominated trihalomethanes in soil, *Environ. Sci. Technol.*, *32*, 3724-3729.

Holland, E. A., A. R. Townsend, and P. M. Vitousek (1995), Variability in temperature regulation of CO_2 fluxes and N mineralization from five Hawaiian soils: Implications for a changing climate, *Global Change Biol.*, *1*, 115-123.

Holtslag, A. A. M., and B. A. Boville (1993), Local versus nonlocal boundary-layer diffusion in a global climate model. *J. Clim.*, *6*, 1825-1842.

Jöckel, P. (2000), Cosmogenic ^{14}CO as tracer for atmospheric chemistry and transport, Rpertus Carola University of Heidelberg, Heidelberg.

Jöckel, P., C. A. M. Brenninkmeijer, M. G. Lawrence, A. B. M. Jeuken, and P. F. J. van Velthoven (2002), Evaluation of stratosphere-troposphere exchange and the hydroxyl radical distribution in three-dimensional global atmospheric models using observations of cosmogenic ^{14}CO, *J. Geophys. Res.*, *107*(D20), 4446, doi:10.1029/2001JD001324.

Kalman, R. E. (1960), A new approach to linear filtering and prediction problems, *J. Basic Eng.*, *82D*, 35-45.

Kalman, R. E., and R. Bucy (1961), New results in linear filtering and prediction, *J. Basic Eng.*, *83D*, 95-108.

Keene, W. C., M. A. K. Khalil, D. J. Erickson III, A. McCulloch, T. E. Graedel, J. M. Lobert, M. L. Aucott, S. L. Gong, D. B. Harper, G. Kleiman, P. Midgley, R. M. Moore, C. Seuzaret, W. T. Sturges, C. M. Benkovitz, V. Koropalov, L. A. Barrie, and Y. F. Li (1999), Composite global emissions of reactive chlorine from anthropogenic and natural sources: Reactive Chlorine Emissions Inventory, *J. Geophys. Res.*, *104*(D7), 8429-8440.

Khalil, M. A. K., R. A. Rasmussen, J. R. J. French, and J. A. Holt (1990), The influence of termites on atmospheric trace gases: CH_4, CO_2, $CHCl_3$, N_2O, CO, H_2, and light hydrocarbons, *J. Geophys. Res., 95*, 3619-3634.

Khalil, M. A. K., and R. A. Rasmussen (1998), Ocean-air exchange of atmospheric trace gases, *Rep. 01-1097*, Dep. Of Phys., Portland State Univ., Portland, Oreg.

Khalil, M. A. K., R. A. Rasmussen, M. J. Shearer, Z.-L. Chen, H. Yao, and J. Yang (1998), Emissions of methane, nitrous oxide and other trace gases from rice fields in China, *J. Geophys. Res., 103*, 25,241-25,250.

Khalil, M. A. K. (1999), Reactive chlorine compounds in the atmosphere, in P. Fabian and O. N. Singh (eds.), *Reactive Halogen Compounds in the Atmosphere*, Springer-Verlag, Berlin, Heidelburg New York, pp. 45-79.

Khalil, M. A. K., and R. A. Rasmussen (1999a), Atmospheric chloroform, *Atmos. Environ.*, *33*, 1151-1158.

Khalil, M. A. K., and R. A. Rasmussen (1999b), Atmospheric methyl chloride, *Atmos. Environ.*, *33*, 1305-1321.

Khalil, M. A. K., R. M. Moore, D. B. Harper, J. M. Lobert, D. J. Erickson, V. Koropalov, W. T. Sturges, and W. C. Keene (1999), Natural emissions of chlorine-containing gases: Reactive Chlorine Emission Inventory, *J. Geophys. Res.*, *104*(D7), 8333-8346.

Kindler, T. P., W. L. Chameides, P. H. Wine, D. M. Cunnold, F. N. Alyea, and J. A. Franklin (1995), The fate of atmospheric phosgene and the stratospheric chlorine loadings of its parent compounds: CCl_4, C_2Cl_4, C_2HCl_3, CH_3CCl_3, and $CHCl_3$, *J. Geophys. Res.*, *100*(D1), 1235-1252.

Kleiman, G., and R. G. Prinn (2000), Measurement and deduction of emissions of trichloroethene, tetrachloroethene, and trichloromethane (chloroform) in the northeastern United States and southeastern Canada, *J. Geophys. Res.*, *105*(D23), 28,875-28,893.

Knorr, W., N. Gobron, M. Scholze, T. Kaminski, R. Schnur, and B. Pinty (2007), Impact of terrestrial biosphere carbon exchanges on the anomalous CO_2 increase in 2002-2003, *Geophys. Res. Lett.*, *34*, L09703, doi:10.1029/2006GL029019.

Kobak, K. I., I. Y. Turchinovich, N. Y. Kondrasheva, E. D. Schulze, W. Schulze, H. Koch, and N. N. Vygodskaya (1996), Vulnerability and adaptation of the larch forest in eastern Siberia to climate change, *Water Air Soil Pollut., 92*, 119-127.

Krummel, P. B., the AGAGE team and respective participating laboratory investigators (2008), Inter-comparison of AGAGE trace gases with other laboratories, 19 pp., unpublished report presented at the 37th meeting of AGAGE scientists, Grindelwald, Switzerland, June 2008.

Kurylo, M. J., J. M. Rodriguez, M. O. Andreae, E. L. Atlas, D. R. Blake, J. H. Butler, S. Lal, D. J. Lary, P. M. Midgeley, S. A. Montzka, P. C. Novelli, C. E. Reeves, P. G.

Simmonds, P. L. Steele, W. T. Sturges, R. F. Weiss, and Y. Yokouchi (1999), Short-lived ozone-related compounds, Chap. 2 in *Scientific Assessment of Ozone Depletion: 1998*, WMO Global Ozone Research and Monitoring Project – Report No. 44, 2.1-2.56.

Laturnus, F., G. Mehrtens, and C. Grøn (1995), Haloperoxidase-like activity in spruce forest soil – a source of volatile halogenated organic compounds? *Chemosphere, 31*, 3709-3719.

Laturnus, F., K. F. Haselmann, T. Borch, and C. Grøn (2002), Terrestrial natural sources of trichloromethane (chloroform, $CHCl_3$) – An overview, *Biogeochemistry, 60*, 121-139.

Lawrence, M. G. (1996), Photochemistry in the tropical pacific troposphere: Studies with a global 3D chemistry-meteorology model, Doctoral thesis, Ga. Inst. of Technol., Atlanta.

Lawrence, M. G., P. J. Crutzen, P. J. Rasch, B. E. Eaton, and N. M. Mahowald (1999b), A model for studies of tropospheric photochemistry: Description, global distributions, and evaluation. *J. Geophys. Res.*, *104*(D21), 26,245-26,277.

Lawrence, M. G., P. J. Rasch, R. von Kuhlmann, J. Williams, H. Fischer, M. de Reus, J. Lelieveld, P. J. Crutzen, M. Schultz, P. Stier, H. Huntrieser, J. Heland, A. Stohl, C. Forster, H. Elbern, H. Jakobs, and R. R. Dickerson (2003), Global chemical weather forecasts for field campaign planning: predictions and observations of large-scale features during MINOS, CONTRACE, and INDOEX, *Atmos. Chem. Phys.*, *3*, 267-289.

Lee-Taylor, J. M., S. C. Doney, G. P. Brasseur, and J.-F. Müller (1998), A global three-dimensional atmosphere-ocean model of methyl bromide distributions, *J. Geophys. Res.*, *103*(D13), 16,039-16,057.

Lee-Taylor, J. M., G. P. Brasseur, and Y. Yokouchi (2001), A preliminary three-dimensional global model study of atmospheric methyl chloride distributions, *J. Geophys. Res.*, *106*(D24), 34,221-34,233.

Lobert, J. M., W. C. Keene, J. A. Logan, and R. Yevich (1999), Global chlorine emissions from biomass burning: Reactive Chlorine Emissions Inventory, *J. Geophys. Res.*, *104*(D7), 8373-8389.

Lucas, D. D., and R. G. Prinn (2005), Sensitivities of gas-phase dimethylsulfide oxidation products to the assumed mechanisms in a chemical transport model, *J. Geophys. Res., 110*, D21312, doi:10.1029/2004JD005386.

Lyon, B. (2004), The strength of El Niño and the spatial extent of tropical drought, *Geophys. Res. Lett.*, *31*, L21204, doi:10.1029/2004GL020901.

Madronich, S., G. J. M. Velders, J. S. Daniel, M. Lal, A. McCulloch, and H. Slaper (1999), Halocarbon scenarios for the future ozone layer and related consequences, Chap.

11 in *Scientific Assessment of ozone depletion: 1998*, WMO Global Ozone Research and Monitoring Project – Report No. 44, 11.1-11.38.

Mahowald, N. M. (1996), Development of a 3-dimensional chemical transport model based on observed winds and use in inverse modeling of the source of CCl_3F, PhD thesis, MIT, Cambridge.

Mahowald, N. M., P. J. Rasch, B. E. Eaton, S. Whittlestone, and R. G. Prinn (1997a), Transport of ^{222}radon to the remote troposphere using the Model of Atmospheric Transport and Chemistry and assimilated winds from ECMWF and the National Center for Environmental Prediction/NCAR, *J. Geophys. Res.*, *102*(D23), 28,139-28,151.

Mahowald, N. M., R. G. Prinn, and P. J. Rasch (1997b), Deducing CCl_3F emissions using an inverse method and chemical transport models with assimilated winds, *J. Geophys. Res.*, *102*(D23), 28,153-28,168.

Maybeck, P. S. (1979), *Stochastic models, Estimation and Control*, Academic, San Diego, Calif.

McCulloch, A., M. L. Aucott, C. M. Benkovitz, T. E. Graedel, G. Kleiman, P. M. Midgley, and Y. F. Li (1999), Global emissions of hydrogen chloride and chloromethane from coal combustion, incineration and industrial activities: Reactive Chlorine Emissions Inventory, *J. Geophys. Res.*, *104*(D7), 8391-8403.

McGuire, A. D., S. Sitch, J. S. Clein, R. Dargaville, G. Esser, J. Foley, M. Heimann, F. Joos, J. Kaplan, D. W. Kicklighter, R. A. Meier, J. M. Melillo, B. Moore III, I. C. Prentice, N. Ramankutty, T. Reichenau, A. Schloss, H. Tian, L. J. Williams, and U. Wittenberg (2001), Carbon balance of the terrestrial biosphere in the twentieth century: analyses of CO_2, climate and land use effects with four process-based ecosystem models, *Global Biogeochem. Cycles*, *15*(1), 183-206.

Montzka, S. A., J. H. Butler, R. C. Myers, T. M. Thompson, T. H. Swanson, A. D. Clarke, L. T. Lock, and J. W. Elkins (1996), Decline in tropospheric abundance of halogen from halocarbons: Implication for stratospheric ozone depletion, *Science*, *272*, 1318-1322.

Montzka, S. A., J. H. Butler, J. W. Elkins, T. M. Thompson, A. D. Clarke, and L. T. Lock (1999), Present and future trends in the atmospheric burden of ozone-depleting halogens, *Nature*, *398*, 690-694.

Montzka, S. A., C. M. Spivakovsky, J. H. Butler, J. W. Elkins, L. T. Lock, and D. J. Mondeel (2000), New observational constraints for atmospheric hydroxyl on global and hemispheric scales, *Science*, *288*, 500-503.

Moore, R. M. (2004), Dichloromethane in North Atlantic waters, *J. Geophys. Res., 109*, C09004, doi:10.1029/2004JC002397.

Mulquiney, J. E., J. A. Taylor, and J. P. Norton (1993), Identifying global sources and sinks of greenhouse gases, in *Modelling Change in Environmental Systems*, edited by A. J. Jakeman *et al*., pp. 431-451, John Wiley, New York.

Mulquiney, J. E., and J. P. Norton (1998), A new inverse method for trace gas flux estimation 1. State-space model identification and constraints, *J. Geophys. Res.*, *103*(D1), 1417-1427.

O'Doherty, S., P. G. Simmonds, D. M. Cunnold, H. J. Wang, G. A. Sturrock, P. J. Fraser, D. Ryall, R. G. Derwent, R. F. Weiss, P. Salameh, B. R. Miller, and R. G. Prinn (2001), In situ chloroform measurements at Advanced Global Atmospheric Gases Experiment atmospheric research stations from 1994 to 1998, *J. Geophys. Res.*, *106*(D17), 20,429-20,444.

O'Doherty, S., D. M. Cunnold, A. Manning, B. R. Miller, R. H. J. Wang, P. B. Krummel, P. J. Fraser, P. G. Simmonds, A. McCulloch, R. F. Weiss, P. Salameh, L. W. Porter, R. G. Prinn, J. Huang, G. Sturrock, D. Ryall, R. G. Derwent, and S. A. Montzka (2004), Rapid growth of hydrofluorocarbon 134a and hydrochlorofluorocarbons 141b, 142b, and 22 from Advanced Global Atmospheric Gases Experiment (AGAGE) observations at Cape Grim, Tasmania, and Mace Head, Ireland, *J. Geophys. Res.*, *109*, D06310, doi:10.1029/2003JD004277.

Prinn, R. G., D. M. Cunnold, R. A. Rasmussen, P. G. Simmonds, F. N. Alyea, A. J. Crawford, P. J. Fraser, and R. D. Rosen (1990), Atmospheric emissions and trends of nitrous oxide deduced from 10 years of ALE/GAGE data, *J. Geophys. Res.*, *95*, 18,369-18,385.

Prinn, R. G., D. M. Cunnold, P. G. Simmonds, F. N. Alyea, B. Boldi, A. J. Crawford, P. J. Fraser, D. Gulzler, D. E. Hartley, R. D. Rosen, and R. A. Rasmussen (1992), Global average concentration and trend for hydroxyl radicals deduced from ALE-GAGE trichloroethane (methyl chloroform) data for 1978-1990, *J. Geophys. Res.*, *97*, 2445-2462.

Prinn, R. G. (2000), Measurement equation for trace chemicals in fluids and solution of its inverse, in *Inverse Methods in Global Biogeochemical Cycles*, *Geophys. Monogr. Ser.*, *114*, edited by P. Kasibhatla *et al*., pp. 3-18, AGU, Washington, D. C.

Prinn, R. G., R. F. Weiss, P. J. Fraser, P. G. Simmonds, D. M. Cunnold, F. N. Alyea, S. O'Doherty, P. Salameh, B. R. Miller, J. Huang, R. H. J. Wang, D. E. Hartley, C. Harth, L. P. Steele, G. Sturrock, P. M. Midgley, and A. McCulloch (2000), A histoty of chemically and radiatively important gases in air deduced from ALE/GAGE/AGAGE, *J. Geophys. Res.*, *105*(D14), 17,751-17,792.

Prinn, R. G., J. Huang, R. F. Weiss, D. M. Cunnold, P. J. Fraser, P. G. Simmonds, A. McCulloch, C. Harth, P. Salameh, S. O'Doherty, R. H. J. Wang, L. Porter, and B. R.

Miller (2005), Evidence for variability of atmospheric hydroxyl radicals over the past quarter century, *Geophys. Res. Lett.*, *32*, L07809, doi:10.1029/2004GL022228.

Rasch, P. J., N. M. Mahowald, and B. E. Eaton (1997), Representations of transport, convection, and the hydrologic cycle in chemical transport models: Implications for the modeling of short-lived and soluble species, *J. Geophys. Res.*, *102*(D23), 28,127-28,138.

Rasch, P. J., and M. G. Lawrence (1998), Recent developments in transport methods at NCAR, in *Rep. 265*, edited by B. Machenhauer, pp. 65-75, Max-Planck-Institute for Meteorology, Hamburg, Germany.

Rasch, P. J., W. D. Collins, and B. E. Eaton (2001), Understanding the Indian Ocean Experiment (INDOEX) aerosol distributions with an aerosol assimilation, *J. Geophys. Res.*, *106*(D7), 7337-7355.

Reimann, S., A. J. Manning, P. G. Simmonds, D. M. Cunnold, R. H. J. Wang, J. Li, A. McCulloch, R. G. Prinn, J. Huang, R. F. Weiss, P. J. Fraser, S. O'Doherty, B. R. Greally, K. Stemmler, M. Hill, and D. Folini (2005), Low European methyl chloroform emissions inferred from long-term atmospheric measurements, *Nature, 433*, 506-508.

Rhew, R. C., B. R. Miller, and R. F. Weiss (2000), Natural methyl bromide and methyl chloride emissions from coastal salt marshes, *Nature*, *403*, 292-295.

Sander, S. P., R. R. Friedl, D. M. Golden, M. J. Kurylo, R. E. Huie, V. L. Orkin, G. K. Moortgat, A. R. Ravishankara, C. E. Kolb, M. J. Molina, and B. J. Finlayson-Pitts (2003), Chemical Kinetics and Photochemical Data for Use in Atmospheric Studies, *Evaluation No. 14, JPL Publication 02-25*, Jet Propulsion Laboratory, Pasadena, Calif.

Schauffler, S. M., L. E. Heidt, W. H. Pollock, T. M. Gilpin, J. F. Vedder, S. Solomon, R. A. Lueb, and E. L. Atlas (1993), Measurements of halogenated organic compounds near the tropical tropopause, *Geophys. Res. Lett.*, *20*(22), 2567-2570.

Seinfeld, J. H., and S. N. Pandis (1998), *Atmospheric chemistry and physics: from air pollution to climate change*, A Wiley-Interscience publication, USA, 1326pp.

Shorter, J. H., C. E. Kolb, P. M. Crill, R. A. Kerwin, R. W. Talbot, M. E. Hines, and R. C. Harriss (1995), Rapid degradation of atmospheric methyl bromide in soils, *Nature*, *377*, 717-719.

Simmonds, P. G., D. M. Cunnold, R. F. Weiss, B. R. Miller, R. G. Prinn, P. J. Fraser, A. McCulloch, F. N. Alyea, and S. O'Doherty (1998a), Global trends and emission estimates of CCl_4 from in situ background observations from July 1978 to June 1996, *J. Geophys. Res.*, *103*(D13), 16,017-16,027.

Simmonds, P. G., R. G. Derwent, A. J. Manning, P. J. Fraser, P. B. Krummel, S. O'Doherty, R.G. Prinn, D.M. Cunnold, B. R. Miller, H. J. Wang, D. B. Ryall, L. W. Porter, R. F. Weiss, and P. K. Salameh (2004), AGAGE observations of methyl bromide and methyl chloride at Mace Head, Ireland, and Cape Grim, Tasmania, 1998-2001, *J. Atmos. Chem.*, *47*(3), 243-269.

Simmonds, P. G., A. J. Manning, D. M. Cunnold, A. McCulloch, S. O'Doherty, R. G. Derwent, P. B. Krummel, P. J. Fraser, B. Dunse, L. W. Porter, R. H. J. Wang, B. R. Greally, B. R. Miller, P. Salameh, R. F. Weiss, and R. G. Prinn (2006), Global trends, seasonal cycles, and European emissions of dichloromethane, trichloroethene, and tetrachloroethene from the AGAGE observations at Mace Head, Ireland, and Cape Grim, Tasmania, *J. Geophys. Res.*, *111*, D18304, doi:10.1029/2006JD007082.

Singh, H. B., L. J. Salas, and R. E. Stiles (1983), Selected man-made halogenated chemicals in the air and ocean environment, *J. Geophys. Res., 88*, 3675-3683.

Singh, H. B. (1995), Halogens in the atmospheric environment, in *Composition, Chemistry and Climate of the Atmosphere*, edited by H. B. Singh, pp. 216-250, Van Nostrand Reinhold, New York.

Solomon, S., *et al*. (1995), Ozone depletion potentials, global warming potentials, and future chlorine/bromine loading, in *Scientific Assessment of Ozone Depletion: 1994, Rep. 37*, pp. 13.1-13.36, Global Ozone Res. and Monit. Proj., World Meteorol. Org., Geneva.

Spivakovsky, C. M., J. A. Logan, S. A. Montzka, Y. J. Balkanski, M. Foreman-Fowler, D. B. A. Jones, L. W. Horowitz, A. C. Fusco, C. A. M. Brenninkmeijer, M. J. Prather, S. C. Wofsy, and M. B. McElroy (2000), Three-dimensional climatological distribution of tropospheric OH: Update and evaluation, *J. Geophys. Res.*, *105*(D7), 8931-8980.

Sturrock, G. A., L. W. Porter, and P. J. Fraser (2001), In situ measurements of CFC replacement chemicals and other halocarbons at Cape Grim: The AGAGE GC-MS program, in *Baseline Atmospheric Program (Australia) 1997-98*, edited by N. W. Tindale, R. J. Francey, and N. Derek, pp. 43-49, Bureau of Meteorology and CSIRO Division of Atmospheric Research, Melbourne, Australia.

Todling, R. (2000), Estimation theory and atmospheric data assimilation, in *Inverse Methods in Global Biogeochemical Cycles*. *Geophys. Monogr. Ser.*, *114*, edited by P. Kasibhatla *et al*., pp. 49-65, AGU, Washington, D. C.

Varner, R. K., P. M. Crill, and R. W. Talboat (1999), Wetlands: a potentially significant source of atmospheric methyl bromide and methyl chloride, *Geophys. Res. Lett.*, *26*(16), 2433-2436.

Volk, C. M., J. W. Elkins, D. W. Fahey, G. S. Dutton, J. M. Gilligan, M. Loewenstein, J. R. Podolske, K. R. Chan, and M. R. Gunson (1997), Evaluation of source gas lifetimes from stratospheric observations, *J. Geophys. Res.*, *102*(D21), 25,543-25,564.

von Kuhlmann, R., M. G. Lawrence, P. J. Crutzen, and P. J. Rasch (2003), A model for studies of tropospheric ozone and nonmethane hydrocarbons: Model description and ozone results, *J. Geophys. Res.*, *108*(D9), 4294, doi: 10.1029/2002JD002893.

Walter, B., and K. Ballschmiter (1992), Formation of C_1/C_2-bromo-/chloro-hydrocarbons by haloperoxidase reactions, *Fresenius J. Anal. Chem., 342*, 827-833.

Watling, R., and D. B. Harper (1998), Chloromethane production by wood-rotting fungi and an estimate of the global flux to the atmosphere, *Mycol. Res., 102*, 769-787.

WMO (World Meteorological Organization) (1999), *Scientific Assessment of Ozone Depletion: 1998*, *Global Ozone Research and Monitoring Project – Report No. 44.,* Geneva, Switzerland.

WMO (World Meteorological Organization) (2003), *Scientific Assessment of Ozone Depletion: 2002*, *Global Ozone Research and Monitoring Project – Report No. 47.,* Geneva, Switzerland.

WMO (World Meteorological Organization) (2007), *Scientific Assessment of Ozone Depletion: 2006*, *Global Ozone Research and Monitoring Project – Report No. 50.,* Geneva, Switzerland.

Wunsch, C. (1996), *The Ocean Circulation Inverse Problem*, Cambridge Univ. Press, Cambridge.

Xiao, X., R. G. Prinn, P. G. Simmonds, L. P. Steele, P. C. Novelli, J. Huang, R. L. Langenfelds, S. O'Doherty, P. B. Krummel, P. J. Fraser, L. W. Porter, R. F. Weiss, P. Salameh, and R. H. J. Wang (2007), Optimal estimation of the soil uptake rate of molecular hydrogen from the Advanced Global Atmospheric Gases Experiment and other measurements, *J. Geophys. Res.*, *112*, D07303, doi:10.1029/2006JD007241.

Yokouchi, Y., Y. Noijiri, L. A. Barrie, D. Toom-Sauntry, T. Machida, Y. Inuzuka, H. Akimoto, H. J. Li, Y. Fujinuma, and S. Aoki (2000b), A strong source of methyl chloride to the atmosphere from tropical coastal land, *Nature*, *403*, 295-298.

Yokouchi, Y., M. Ikeda, Y. Inuzuka, and T. Yukawa (2002), Strong emission of methyl chloride from tropical plants, *Nature*, *416*, 163-165.

Yvon-Lewis, S., and J. H. Butler (2002), The effect of oceanic uptake on atmospheric lifetimes of selected trace gases, *J. Geophys. Res.*, *107*(D20), 4414, doi:10.1029/2001JD001267.

Zhang, G. J., and N. A. McFarlane (1995), Sensitivity of climate simulations to the parameterization of cumulus convection in the Canadian Climate Centre general circulation model, *Atmos. Ocean*, *33*, 407-446.

Zeng, N., H. Qian, C. Roedenbeck, and M. Heimann (2005b), Impact of 1998-2002 midlatitude drought and warming on terrestrial ecosystem and the global carbon cycle, *Geophys. Res. Lett.*, *32*, L22709, doi:10.1029/2005GL024607.